



CHARACTERIZATION OF ELECTRON BUNCHES
FROM FIELD EMITTER ARRAY CATHODES FOR
USE IN NEXT-GENERATION X-RAY FREE
ELECTRON LASERS

Thesis submitted to the
SWISS FEDERAL INSTITUTE OF TECHNOLOGY LAUSANNE
for the degree of Doctor of Sciences

presented by
SIMON CHRISTIAN LEEMANN
Dipl. Phys. ETH
citizen of the United States of America and Switzerland

January 2007

EPFL Thesis No. 3724 (2007)

Presented on

25 January 2007

to the

Faculty of Basic Sciences

Accepted on the recommendation of

Prof. Dr. R. Schaller (EPFL), President of the Jury

Prof. Dr. A. F. Wrulich (EPFL/PSI), Thesis Director

Dr. H. Braun (CERN), Referee

Prof. Dr. R. Chawla (EPFL), Referee

Dr. A. Streun (PSI), Referee

To Dina

Abstract

PSI is interested in developing an X-FEL as a companion radiation source to the existing Swiss Light Source. In order to achieve radiation wavelengths as low as 1 Å, the X-FEL requires excellent electron beam quality and high beam energy. The energy requirements and thus the size and cost of the project can be reduced considerably if an ultra-low emittance electron source is developed. Therefore PSI has started the Low Emittance Gun Project with the aim to design a novel type of electron source that will deliver an electron beam with unprecedented emittance at high peak currents to the linear accelerator of the proposed X-FEL. A source candidate for such a gun is field emission from cold cathodes. In order to gain first experience with field emission guns, investigate the dynamics of space charge dominated electron beams and to develop diagnostics capable of resolving ultra-low emittances, it was decided to build a 100 keV DC gun test stand. In the scope of this thesis, the test stand has been designed, assembled and commissioned. For the first time, transverse phase space measurements of bunches emitted by field emitter arrays in pulsed DC accelerating fields have been performed.

Keywords: synchrotron radiation source, X-ray free electron laser, linac, electron gun, field emitter array, transverse emittance measurement, pinhole array, slit array, pepperpot, emittance compensation, solenoid magnet

Zusammenfassung

Das PSI ist an der Entwicklung eines X-FEL als komplementäre Lichtquelle zur bestehenden Synchrotron Lichtquelle Schweiz interessiert. Um Strahlung mit Wellenlängen bis zu 1 \AA zu erzeugen, verlangt ein X-FEL ausgezeichnete Elektronenstrahleigenschaften und hohe Strahlenergie. Die Anforderungen an die Energie, und somit an Grösse und Kosten des Projekts, können bedeutend reduziert werden, sollte eine Elektronenquelle mit sehr kleiner Emittanz gefunden werden. Deshalb hat das PSI das Low Emittance Gun Projekt gegründet mit dem Ziel, eine neuartige Elektronenquelle zu entwickeln, die bisher unerreichte Emittanz bei gleichzeitig hohem Spitzenstrom an den Linearbeschleuniger des X-FEL liefern soll. Eine mögliche Quelle für eine solche Elektronenkanone ist Feldemission von kalten Kathoden. Um erste Erfahrungen mit auf Feldemission basierten Kanonen zu sammeln, die Dynamik durch Raumladung dominierter Elektronenstrahlen zu untersuchen und Diagnostik zu entwickeln, welche niedrigste Emittanzen messen kann, wurde beschlossen, einen 100 keV Teststand zu bauen. Im Rahmen dieser Dissertation wurde dieser Teststand entwickelt, aufgebaut und in Betrieb genommen. Zum ersten Mal wurde der transversale Phasenraum von Elektronenpaketen, die von einer Feldemissions-Matrix ausgesendet und in gepulsten Gleichstromfeldern beschleunigt wurden, ausgemessen.

Contents

1	Introduction	19
1.1	A Brief History of Synchrotron Radiation Sources	19
1.2	Future Synchrotron Radiation Sources and the X-FEL	21
1.3	PSI's X-FEL and LEG Project	26
1.4	The LEG Project's 100 keV DC Gun Test Stand	31
1.5	Thesis Outline	32
2	Theory & Framework	35
2.1	Phase Space Distributions	35
2.2	The Concept of Emittance	38
2.2.1	Statistical Definition	38
2.2.2	Optical Definition	40
2.2.3	The Envelope Equation	42
2.2.4	Slice and Projected Emittance	44
2.3	Brightness	46
2.3.1	Definition	47
2.3.2	Brightness Limitations	48
2.4	Space Charge Forces	49
2.5	Phase Space Manipulation Techniques	52
2.5.1	Bunch Compression	52
2.5.2	Emittance Compensation	54
2.5.3	Radiation Damping	58
2.6	Electron Emission	59

2.6.1	Thermal Emittance	59
2.6.2	Survey of Electron Emission Sources	61
2.6.3	Field Emission and Field Emitter Arrays	64
3	Simulation	71
3.1	Gun Design	71
3.1.1	Input Parameters	72
3.1.2	Optimization	73
3.2	Solenoid Design	78
3.3	Specifications for Diagnostics	83
3.4	Slice Emittance from MAFIA Data	88
3.5	Tolerances	90
4	Test Stand Setup & Implementation	95
4.1	Overview	95
4.2	General Infrastructure	97
4.3	Beam Path	97
4.3.1	Gun Assembly	97
4.3.2	FEA and Mounting	98
4.3.3	Diode Structure: Cathode and Anode	99
4.3.4	Solenoid Magnet	102
4.3.5	Drift Section	103
4.4	High Voltage & FEA Pulsing	104
4.4.1	High Voltage Power Supply	104
4.4.2	Hotdeck	105
4.4.3	Pulser	106
4.5	Vacuum System	106
4.5.1	Vacuum Pumps	107
4.5.2	Vacuum Diagnostics	108
4.6	Control System	111
4.6.1	Control System Hardware and Software	111
4.6.2	Fiber Optic Communication	113

4.6.3	Timing System	114
4.7	Diagnostics	115
4.7.1	Faraday Cup	115
4.7.2	Screen Monitors and Camera Systems	116
4.7.3	Slit and Pinhole Inserts	119
4.7.4	Single Slit Measurement Technique	120
4.7.5	Slit Array & Pinhole Measurement Technique	122
5	Commissioning of the Test Stand	127
5.1	Solenoid Magnet Calibration	127
5.1.1	Measurement Setup	128
5.1.2	Background Measurement	130
5.1.3	Field Calibration	131
5.1.4	Longitudinal Field Scans	132
5.1.5	Fringe Field Measurements	134
5.2	Calibration of the Optical System & Point-Spread Function	136
5.2.1	Measurement Setup	136
5.2.2	Horizontal and Vertical Profile Measurements	137
5.2.3	Point-Spread Function	144
5.3	Startup & First Operation	146
5.3.1	Assembly and Initial Pumpdown	146
5.3.2	Single Tip Conditioning	147
5.3.3	HV Commissioning	150
5.3.4	Conditioning the FEA	152
5.3.5	Breakdown and FEA Destruction	156
6	Experimental Results	163
6.1	FEA Performance Calibration	164
6.1.1	Gate Voltage Influence	165
6.1.2	HV Influence	167
6.1.3	Pulse Length Influence	170
6.2	Investigation of Transverse Beam Profile	173

6.2.1	Transverse Beam Size as a Function of Bunch Charge .	176
6.2.2	Transverse Beam Size as a Function of Solenoid Field .	178
6.2.3	Beam Size Measurement Comparison	180
6.3	Emittance Measurements	184
6.3.1	Solenoid Scan	184
6.3.2	Measurements with the Single Slit	195
6.3.3	Measurements with the Slit Array	198
6.3.4	Measurements with the Pinhole Array	200
6.3.5	Emittance as a function of Bunch Charge	206
6.3.6	Emittance as a function of HV	206
6.3.7	Emission Considerations	208
6.4	Comparison of Measurements with Simulation	209
7	Conclusions & Outlook	217
A	Design Drawings of the Gun Test Stand	227

List of Figures

1.1	Schematic of a typical FEL layout	22
1.2	Required undulator length for an X-FEL	25
1.3	Peak brightness of SLS and the PSI X-FEL	27
1.4	Schematic of the proposed PSI X-FEL	28
2.1	Schematic of a particle bunch in trace space.	42
2.2	Comparison of slice and projected emittance	45
2.3	Schematic of emittance compensation	55
2.4	Simple FEA consisting of pyramidal tips	66
2.5	Gated FEA consisting of pyramidal tips	67
2.6	Gated FEA with focusing layer	68
2.7	Spindt-type FEA	69
3.1	Final gun design	76
3.2	Emittance as a function of gun electrode angle	76
3.3	Emittance as a function of anode iris radius	77
3.4	Electric field strength as a function of accelerating gap	78
3.5	Final solenoid design	79
3.6	Longitudinal magnetic field strength in the solenoid	80
3.7	RMS beam radius for different solenoid settings	81
3.8	Emittance evolution for different solenoid settings	82
3.9	Emittance as a function of solenoid setting	82
3.10	Emittance minima and corresponding longitudinal positions	83
3.11	Angular acceptance of hole/slit measurements	85

3.12	Pepper-pot beamlets in trace space	85
3.13	Pepper-pot beamlets on the screen monitor	86
3.14	Slit array beamlets in trace space	87
3.15	Slit array beamlets on the screen monitor	87
3.16	Example of simulated trace space reconstruction	88
3.17	Slice emittance simulation example	89
3.18	Cathode tilt angle tolerance	91
3.19	Cathode displacement tolerance	91
4.1	Schematic of the test stand.	96
4.2	3D rendering of the test stand.	96
4.3	3D rendering of the test stand diode and solenoid	98
4.4	Schematic of a Spindt-type FEA	99
4.5	Photo of the cathode electrode	100
4.6	Photos of the anode electrode	101
4.7	Photo of the solenoid magnet assembly	102
4.8	Photo of the hotdeck	105
4.9	Examples of rest gas analyzer spectra	110
4.10	Photo of test stand control system hardware	111
4.11	3D rendering of the Faraday cup	115
4.12	Photo of the YAG screen monitor optics	117
4.13	Photo of the phosphor screen monitor system	118
4.14	Measurement modes with pinhole array and pepper-pot	121
5.1	Measurement setup for solenoid magnet calibration	128
5.2	Coordinate system used for solenoid calibration	129
5.3	Magnetic field background measurements	130
5.4	Solenoid calibration data	131
5.5	Longitudinal magnetic field scans on and off axis	132
5.6	Differences between on and off axis longitudinal scans	133
5.7	Longitudinal magnetic field measurement in the fringe field	134
5.8	Experimental setup to determine the PSF	136

5.9	Schematic of the PSF measurement setup	137
5.10	Profiles for a 15 μm pinhole, high intensity, iris half open . . .	139
5.11	Profiles for a 15 μm pinhole, reduced intensity, iris half open .	140
5.12	Profiles for a 15 μm pinhole, reduced intensity, iris fully open .	140
5.13	Profiles for a 15 μm pinhole, high intensity, iris almost closed .	141
5.14	Profiles for a 10 μm pinhole, reduced intensity, iris half open .	142
5.15	Profiles for a 10 μm pinhole, reduced intensity, iris fully open .	142
5.16	Profiles for a 5 μm pinhole, high intensity, iris half open	143
5.17	Profiles for a 5 μm pinhole, high intensity, iris fully open	143
5.18	Profiles for a 5 μm pinhole, high intensity, iris half open	144
5.19	Measured image size vs. pinhole diameter	145
5.20	Photo of the ZrC single-tip emitter	148
5.21	Thermionic emission current as a function of heating current .	149
5.22	Increased thermionic emission current due to conditioning . .	150
5.23	FEA conditioning with long pulses	154
5.24	FEA conditioning with short pulses	156
5.25	Photos of FEA and anode iris damage	157
5.26	SEM picture of FEA destroyed by HV breakdown	158
5.27	Vacuum chamber pressure during FEA destruction	160
6.1	Faraday cup measurement with a fast oscilloscope	164
6.2	Calibration of SRI-1257B	166
6.3	Calibration of different FEAs	166
6.4	FEA calibration for different accelerating HV	167
6.5	Anode vs. Faraday cup collected current for different HV . . .	168
6.6	Reduction of beam scraping for increased accelerating HV . .	169
6.7	Faraday cup collected current as a function of pulse length . .	170
6.8	Peak current for different gate voltages and pulse lengths . . .	171
6.9	Minimum required pulse length for maximum peak current . .	172
6.10	Transverse beam profile of a focused bunch	174
6.11	Non-uniformities in the beam profile of an unfocused beam . .	175
6.12	Beam size evolution in the diagnostics section	176

6.13	Beam size as a function of bunch charge	177
6.14	Influence of solenoid focusing on beam profile	178
6.15	Beam size evolution for different solenoid focusing strengths	179
6.16	Waist position as a function of solenoid field	181
6.17	Beam size evolution in the diagnostics section	182
6.18	Example of solenoid scan and thin lens fit	186
6.19	Solenoid scan and analysis for a hard edge solenoid model	190
6.20	Solenoid scan and analysis for a smooth edge solenoid model	191
6.21	1-sigma phase space ellipses for the data analyzed with EML	194
6.22	Example of a single slit emittance measurement	196
6.23	Example of a slit array measurement	199
6.24	Pinhole array emittance measurement example	200
6.25	Analysis of the horizontal pinhole data	202
6.26	Analysis of the vertical pinhole data	203
6.27	Reconstructed phase space densities from PHSPDENS	205
6.28	Emittance measured as a function of bunch charge	207
6.29	Emittance measured before and after HV breakdown	207
6.30	Comparison between measured data and simulation	212
6.31	Comparison between measured data and simulation	213
A.1	Overview plan of the test stand	228
A.2	Design drawing of the cathode assembly and ceramic break	229
A.3	Design drawing of the cathode assembly with FEA mounting	230
A.4	Design drawing of the anode and solenoid assembly	231
A.5	Overview plan of the test stand diagnostics	232

List of Tables

1.1	X-FEL goal parameters	28
1.2	Pre-injector goal parameters	29
1.3	Accelerator goal parameters	30
3.1	Simulation input parameters	74
6.1	Comparison of beam size measurements	183
6.2	Summary of solenoid scan fit and derived results	188
6.3	Summary of fit results for thin and thick lens models	192
6.4	Error contributions in the thick lens model	193
6.5	Solenoid scan results with errors	195
6.6	Single slit emittance measurement results and analysis	197
6.7	Single slit measurements with variable drift distance	197
6.8	Pinhole emittance measurement results	201
6.9	Error contributions for pinhole measurement analysis	204
6.10	Comparison of beam size measurements	206

List of Symbols

$e = 1.602 \cdot 10^{-19}$ C	elementary charge
$c = 2.998 \cdot 10^8$ m/s	speed of light in vacuum
$m_e = 511$ keV/c ²	mass of the electron
$k_B = 8.617 \cdot 10^{-5}$ eV/K	Boltzmann's constant
$\beta = \vec{\beta} = \vec{v} /c$	normalized relativistic velocity
$\gamma = (1 - \beta^2)^{-1/2}$	relativistic energy in units of the particle rest mass
(\vec{q}, \vec{p})	canonical variables
$\vec{q} = (x, y, z)$	canonical configuration space
$\vec{p} = (p_x, p_y, p_z)$	canonical momentum space
Γ	6D phase space
$\Psi(\vec{q}, \vec{p})$	phase space distribution density
Q	bunch charge
(q_i, p_i)	phase space plane
(x_i, x'_i)	trace space plane
$u = x, y$	transverse coordinates
$E = \gamma mc^2$	total Lorentz-invariant energy of a particle
$p = mc\gamma\beta$	total Lorentz-invariant momentum of a particle
$[\beta, \alpha, \gamma]_u$	Courant-Snyder parameters
ε	RMS emittance
$\varepsilon^{(n)} \approx \beta\gamma\varepsilon$	normalized RMS emittance
$\mathcal{B}, \mathcal{B}^{(n)}$	brightness and normalized brightness
ϕ_w	work function
$W = \frac{3}{2}k_B T$	thermal energy

Chapter 1

Introduction

This chapter begins by giving a very brief overview of the development of synchrotron radiation sources and a prospect on future sources. It continues by motivating PSI's plans to build a 4th generation light source in addition to the existing 3rd generation facility SLS (Swiss Light Source) [1]. Due to the stringent requirements of such a light source, a novel type of electron gun is required, which is the motivation behind the Low Emittance Gun (LEG) Project [2]. An introduction to the project and the project's 100 keV DC Gun Test Stand is given in the next sections. The chapter concludes by giving the outline of this thesis.

1.1 A Brief History of Synchrotron Radiation Sources

The first observation of synchrotron radiation was performed at the 70 MeV synchrotron of the GE Research Lab in Schenectady, New York in 1947.¹

¹The name *synchrotron radiation* was given to this type of electromagnetic radiation because it was generated by a synchrotron. At the time, the synchrotron was the only machine capable of accelerating electrons to energies where detectable amounts of this radiation are produced.

Initially synchrotron radiation was considered a nuisance by the high energy physics community because it was a source of potentially hazardous radiation and an efficient energy loss mechanism. However, it didn't take long until another research community discovered how to use synchrotron radiation in a beneficial manner.

In the meantime synchrotron radiation has become an indispensable research tool in science, medicine and engineering. There are several reasons why synchrotron radiation has become such a popular tool: Similar to the radiation from X-ray cathode tubes (first demonstrated by Wilhelm Conrad Röntgen in 1895) synchrotron radiation has penetrating capabilities enabling researchers to see below surfaces and inside matter. Additionally, synchrotron radiation covers the very wide energy spectrum from radio waves all the way to hard X-rays. It includes wavelengths comparable to molecular and atomic dimensions making it a prime tool to investigate molecular structures (since the radiation wavelength determines the smallest structure size that can be resolved). Due to its rather short pulsed emission, it can also be used for time-resolved imaging.

Ever since its first use as a research tool a quest has started to increase the figure of merit of synchrotron radiation sources: the *brightness* (sometimes also called brilliance, see Section 2.3.1). A synchrotron radiation source's brightness is given by its photon flux per unit area, per unit solid angle, per unit spectral bandwidth; it is a measure for the 6-D phase space density of the emitted photon beam. In this quest for higher brightness three generations of synchrotron radiation sources have been built and each generation increased the brightness by several orders of magnitude compared to the previous generation.

The 1st generation is composed of sources that weren't originally designed as radiation sources, but rather as accelerators or colliders for high energy physics and were parasitically or alternatively used as radiation sources (examples are CESR in Ithaca NY, USA or DORIS in Hamburg, Germany). The 2nd generation consists of the first machines optimized and built as ded-

icated synchrotron radiation sources (NSLS in Brookhaven NY, USA or SRS in Daresbury, England). 3rd generation machines (ALS in Berkeley CA, USA or SPring-8 in Hyogo, Japan) were built for the insertion of undulators and wigglers (so-called “insertion devices”), which are special devices inserted into the electron beam to enhance the photon yield of a synchrotron storage ring.

1.2 Future Synchrotron Radiation Sources and the X-FEL

Presently many 3rd generation synchrotron radiation sources are operational around the world and several new sources are currently under construction. The average brightness has been increased over thirteen orders of magnitude since the first X-ray tubes! However, there are still requests for further increased brightness and especially for ultra-short pulse lengths. In addition, certain applications require full transverse *and* longitudinal coherence of the photon beam.² Synchrotron radiation sources that deliver these qualities are referred to as 4th generation sources.

A concept for such a source is the *X-FEL* (X-Ray Free Electron Laser); it is a special type of FEL that produces photons as high in energy as hard X-rays. A good introduction to the principles of FELs is given in [3]. A simple schematic of a typical FEL layout is shown in Fig. 1.1.

In an FEL electron bunches are accelerated to relativistic energies and pass an undulator where they interact with the emitted electromagnetic wave and

²It is important to distinguish spatial and temporal coherence. Temporal (or longitudinal) coherence is given when the bunch or part of a bunch (microbunch) that radiates is shorter than the emitted wavelength; as a consequence the photons of such radiation are emitted with roughly the same phase. Spatial (or transverse) coherence indicates that the transverse emittance of the electron bunch or microbunch (slice emittance) is less than the emittance of the radiated photon beam; this means that an observer sees the emitted radiation as coming from a point source.

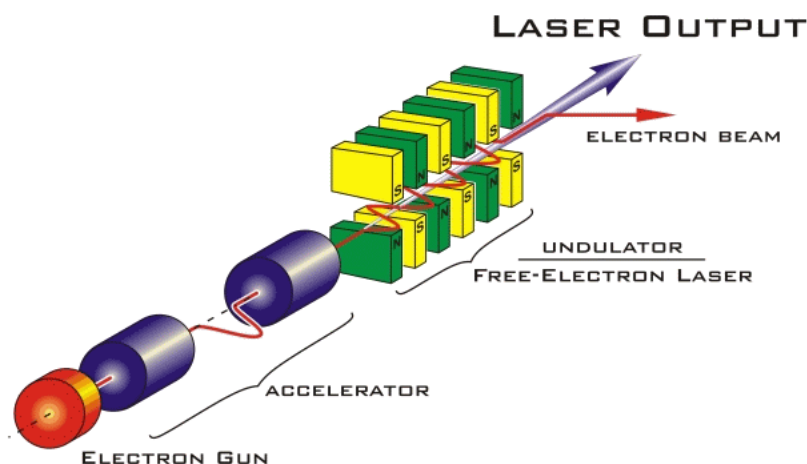


Figure 1.1: Schematic of a typical FEL layout: An electron beam is accelerated to high energy and passes an undulator where the electrons interact with the alternating magnetic field and radiate coherently. Image courtesy of [2].

radiate coherently. The energy exchange between the electron bunch (in the picture of a classical laser this is the gain medium) and the radiated photon beam is not linked to a certain quantum state transition of bound electrons (hence the expression *free electron laser*). The wavelength of the extracted radiation, which is both spatially and temporally coherent, can be selected by changing the undulator parameters (gap) and/or the energy of the electrons. An X-FEL delivers fully coherent, short-pulsed (down to femtoseconds!) radiation with orders of magnitude increased power and brightness compared to a 3rd generation synchrotron source.³ As with previous synchrotron sources, the X-FEL allows selection of wavelength or photon energy. Therefore, it makes use of the properties associated with classical laser systems in a spectral range previously only accessible with synchrotron radiation.

One major challenge in the design of an X-FEL is that one cannot build

³Since in an X-FEL radiation is emitted coherently, its power scales with the number of electrons in the bunch *squared* rather than scaling linearly (as is the case for the incoherent emission coming from the bending magnet of a storage ring based light source). This quadratic dependence is the reason for the great increase in brightness.

optical resonator cavities for X-rays. There are currently no mirrors capable of deflecting X-rays at 180° with high reflectivity. Therefore a single-pass X-FEL is being considered. In such a system there is no optical resonator cavity; the interaction between the electron beam and the photon beam happens within the undulator in one single pass of the electron bunch after which the electrons are extracted (and subsequently either dumped or recirculated) and the photon beam is transported to the experiment. Therefore a mechanism has to be found in which the electron bunch transfers a maximum fraction of its energy to a coherent photon beam within a single undulator section.

SASE (Self-Amplification Through Spontaneous Emission) is such a mechanism: In the undulator of a SASE-based X-FEL the electron bunch first emits incoherent radiation as in a usual undulator. This radiation then acts back on the the electron bunch by modulating its energy distribution (the so-called *microbunching*) and due to this modulation the bunch emits coherent radiation throughout the rest of the undulator. At TTF (TESLA Test Facility) in Hamburg, Germany [4] it has been verified that the SASE principle indeed produces coherent photon beams and only a few years ago radiation down to a wavelength of 80 nm was successfully demonstrated [5]. PSI is planning on applying the SASE concept for its X-FEL Project.

In order to reach lowest photon wavelengths, additional requirements for the electron bunch have to be made: high peak current, low energy spread and low emittance. In other words the electron beam brightness should be maximized (see Section 2.3.1). These requirements are not met by light source storage rings which cannot deliver sub-ps high-brightness beams. On the other hand, in a well-designed linac the electron beam brightness is mainly determined by the source. If an electron source delivers high peak current in low emittance bunches and the emittance can be preserved by quick acceleration to highly-relativistic energies (see Section 2.4), the linac can deliver such an electron beam to the undulator section and meet all requirements for SASE lasing. Therefore linacs are the accelerators of choice to drive the undulators of an X-FEL.

Throughout the undulator section (which can be on the order of ≈ 100 m) a spatial overlap of the electron beam with the diffraction limited photon beam has to be achieved. Spatial coherence in an FEL requires that the transverse electron beam emittance ε (see Section 2.2) is smaller than the photon beam emittance $\varepsilon^{(\gamma)}$ [6]

$$\varepsilon < \varepsilon^{(\gamma)} = \sigma_{x,y}^{(\gamma)} \sigma_{x',y'}^{(\gamma)} = \frac{1}{2} \sigma_r \sigma_{r'}, \quad (1.1)$$

where $\sigma_{x,y}^{(\gamma)} = \sigma_r / \sqrt{2}$ has been used. From the diffraction pattern of a Gaussian source the condition

$$\frac{2\pi}{\lambda} \sigma_r \sigma_{r'} = 1 \quad (1.2)$$

is known. This then leads to the spatial coherence criterion for an FEL

$$\varepsilon = \frac{\varepsilon^{(n)}}{\beta\gamma} < \frac{\lambda}{4\pi}, \quad (1.3)$$

where λ is the radiated photon wavelength and $\varepsilon^{(n)}$ the normalized emittance.

To ensure proper SASE lasing, sufficient undulator length, the so-called *saturation length*, is required. In practice $L_{\text{sat}} \approx 20 L_g$ is sufficient [7], where L_g is the undulator *gain length*.⁴ The gain length can be expressed by [7]

$$L_g \approx \frac{\lambda_u}{4\sqrt{3}\pi\rho} \quad (1.4)$$

with the Pierce parameter ρ which is typically between $10^{-2} - 10^{-3}$.

Finally, the radiated wavelength in a flat undulator is given by

$$\lambda = \frac{\lambda_u}{2\gamma^2} \left(1 + \frac{K^2}{2} \right), \quad (1.5)$$

where λ_u is the undulator period and the undulator parameter K is proportional to the applied magnetic field and the undulator period [8].

⁴Since the SASE X-FEL makes use of self-amplifying microbunching in order to generate coherent radiation, the radiation power grows exponentially; this gives rise to the definition of gain length L_g : $P(z) \propto e^{2z/L_g}$.

From the spatial coherence criterion (1.3) one sees that the required normalized emittance scales linearly with the beam energy. However, from the radiation wavelength (1.5) one sees that the radiation wavelength scales inversely quadratic with the energy. This illustrates clearly why short wavelength operation is the most challenging: it demands highest energies and at the same time minimum transverse emittance. The smaller the desired radiated wavelength, the more stringent requirements on the transverse emittance become. This is demonstrated in Fig. 1.2 which shows how the required undulator length and electron beam energy depend on radiated wavelength and undulator period in an X-FEL.

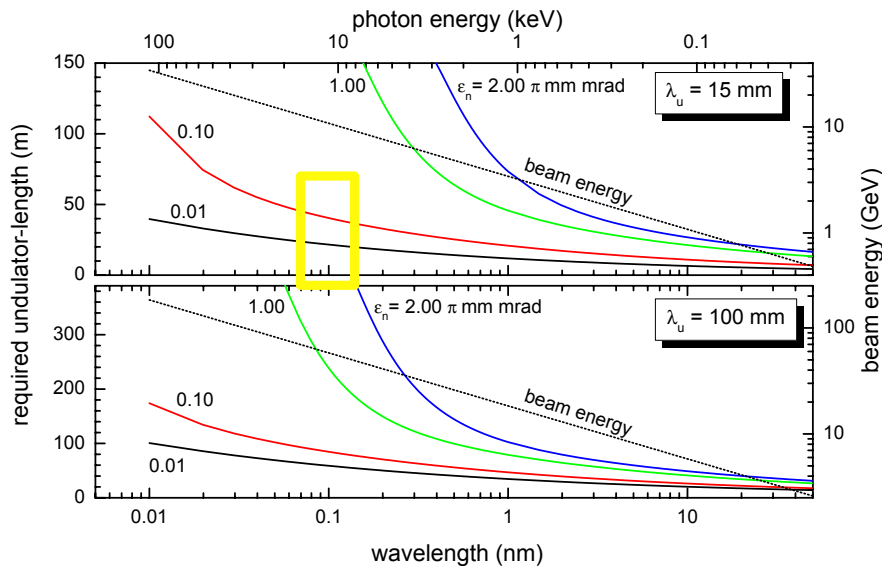


Figure 1.2: Required undulator length and electron beam energy in an X-FEL as functions of the radiated wavelength for several electron beam emittances and two different undulator period lengths. The plot illustrates clearly that at lowest electron beam emittances, 1 \AA radiation is possible with conventional undulator technology for beam energies below 10 GeV and undulators shorter than 100 m. Plot courtesy of [2].

There are currently several projects worldwide to build X-FELs. Among the furthest advanced projects are LCLS (Linac Coherent Light Source) in Stan-

ford CA, USA [9] and the European X-FEL Project at DESY in Hamburg, Germany [10]. These projects make use of high energy electron beams (up to 20 GeV) to reduce the geometrical source emittance requiring long (and thus expensive) linacs. Therefore they can make use of existing electron sources that deliver a beam with ≈ 1 mm mrad normalized transverse emittance.

A different approach to short wavelengths is to use a low emittance electron beam thus requiring a lower final electron beam energy, which in turn allows shorter and less expensive linacs. This approach is being taken at SCSS (SPring-8 Compact SASE Source) in Hyogo, Japan [11] where a thermionic electron source is expected to deliver a normalized transverse emittance of 0.4 mm mrad [12] allowing for 3.6 nm radiation at only 1 GeV beam energy [13]. Extending the low emittance strategy to even shorter wavelengths is the goal at PSI.

1.3 PSI's X-FEL and LEG Project

PSI is interested in an X-FEL as a companion synchrotron source to SLS. SLS is a successful 3rd generation light source which delivers high average brightness and ps pulses to experimental users since 2001. The proposed PSI X-FEL [14] will complement experimental user requirements by delivering high peak brightness photon bunches with pulse lengths in the fs range and wavelengths down to 1 Å. A comparison between the peak brightness of SLS and the proposed PSI X-FEL is given in Fig. 1.3.

The development at PSI aims for the realization of an X-FEL based on advanced concepts that will allow substantial downsizing of the facility. The design goals for the PSI X-FEL are 1 Å wavelength and lowest necessary energy in order to reduce the total length and cost of the X-FEL. The conditions shortest wavelength and lowest energy can only be fulfilled by using an electron source with ultra-low emittance. Therefore realization of the PSI X-FEL relies on a novel type of electron gun delivering unprecedented bright-

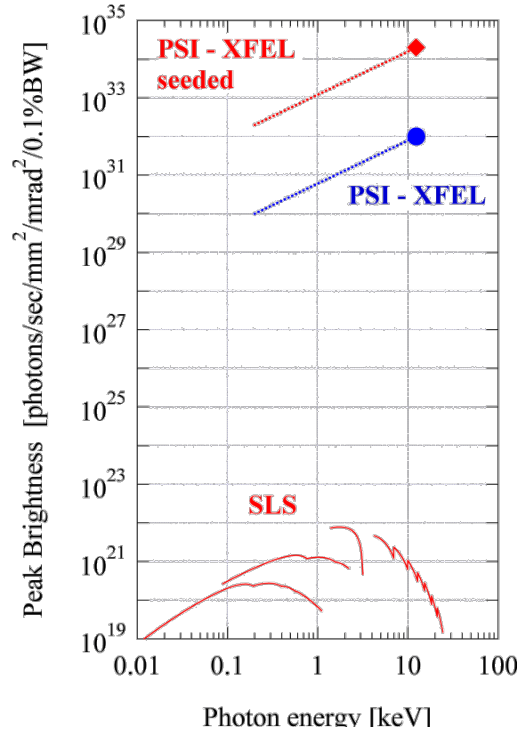


Figure 1.3: A comparison of peak brightness as a function of radiated photon energy for of the existing 3rd generation source SLS and the proposed 4th generation source PSI X-FEL. Plot courtesy of [2].

ness: 5.5 A peak current in 35 ps bunches with 0.05 mm mrad normalized transverse emittance. With such an electron source an FEL undulator section with 15 mm period and 45 m total length can be driven with a 5.8 GeV electron beam with a peak current of 1.5 kA delivering 1 Å radiation pulses with 10 Hz to experimental users [14, 15]. A summary of the X-FEL target parameters is given in Table 1.1.

The goals of PSI’s LEG Project are therefore to develop a novel type of electron gun with ultra-low emittance and a subsequent accelerating section capable of preserving this emittance, compressing the bunches to reach the desired peak current, and accelerating them to the final energy. A schematic of the proposed accelerator is given in Fig. 1.4.

Table 1.1: Goal parameters for the PSI X-FEL undulator [2].

Undulator Period	15 mm
Undulator Gap	5.97 mm
RMS Undulator Strength (K)	0.84
Number of Undulator Sections	8
Slice Duration	0.03 fs
Gain Length	1.4 m
Saturation Length	24 m
Uncorrelated Energy Spread	100 keV
Radiated Wavelength	1 Å
Total Length	45 m

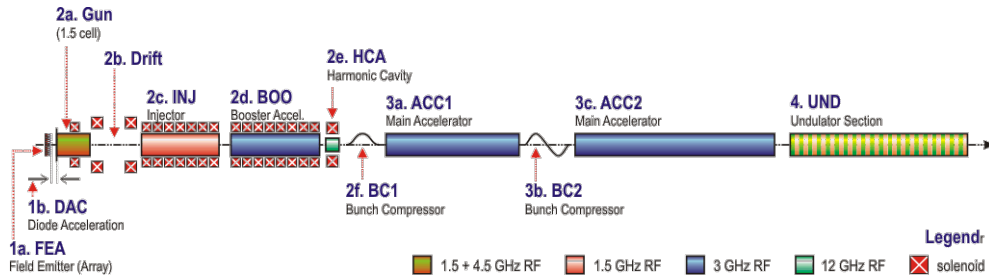


Figure 1.4: Schematic of the proposed PSI X-FEL. The accelerator consists of a gun, injector, booster, bunching sections and main accelerator sections. Following the accelerator an undulator section will emit the coherent 1 Å radiation for experimental users. Plot courtesy of [2].

As a candidate for a low emittance electron source an FEA (field emitter array) is being considered [16]. Such a source is an array of thousands of nano-tips from which electrons can be extracted through field emission by applying an electric field (field emission and FEAs will be described in more detail in Section 2.6.3). An additional grid only $\approx 2 \mu\text{m}$ away from the

tips (the so-called *gate layer*) can be used to trigger pulsed emission into the accelerating field of the actual gun. The tips emit electrons from a microscopic surface (on the order of a few μm^2). If a focusing layer is applied in addition to the gate layer, the beamlet emitted by each tip can be focused at emission to minimize divergence spread. In combination small source size and small source divergence spread should lead to the required ultra-low emittance source.

Table 1.2: Goal parameters for the LEG/X-FEL Project's pre-injector system [2].

Bunch Charge	0.2 nC
Peak Current	5.5 A
RMS Bunch Length	14.5 ps
Normalized Emittance (projected)	0.05 mm mrad
Final Energy	1 MeV
Total Length	2154 mm

Immediately after passing the focusing layer the electrons are accelerated by a pulsed DC HV field across a short gap (to preserve the low emittance from space charge blow-up; see Section 2.4) and into a first accelerating cavity. For the targeted 10 Hz repetition rate normal conducting accelerating structures are the cost optimized solution. The first cavity and a subsequent short drift are to be placed in a solenoid field for emittance compensation (see Section 2.5.2). The bunch is then accelerated to higher energies (where the transverse phase space distribution “freezes out”) by an injector and booster. At this stage the first magnetic bunch compressor will shorten the bunch and thus increase its peak current. The first main accelerating structure follows and accelerates the beam to 1 GeV after which the final bunch compressor shortens the bunch to 50 fs pulse length and the peak current reaches the

required 1.5 kA. The following S-band linac structures then accelerate the beam to its final energy of 5.8 GeV [14, 15].

Table 1.3: Goal parameters for the LEG/XFEL Project’s accelerator system [2].

Bunch Charge	0.2 nC
Peak Current	1.5 kA
RMS Bunch Length	0.05 ps
Normalized Emittance (slice)	0.1 mm mrad
Final Energy	5.8 GeV
Total Length	477.9 m

To ensure that the initial low emittance of the electron bunch after emission by the FEA is transported all the way to the undulator, dedicated measures throughout the entire accelerator have to be taken. Within the actual electron gun and the first accelerating sections this has two direct implications:

- The low emittance with which the electrons are emitted from the FEA has to be preserved until the bunch has acquired sufficiently high energies where the emittance is “frozen” due to the highly relativistic particle velocities.
- Emittance blow-up due to space-charge forces has to be compensated by implementing an appropriate compensation scheme at low beam energies.

The LEG Project has to develop a novel type low emittance gun and successfully master these two challenges to make the PSI X-FEL possible.

1.4 The LEG Project's 100 keV DC Gun Test Stand

The LEG Project initially needed to address three questions: Can FEAs be used as a low emittance electron source for an accelerator? What are the properties of the electron bunches emitted by such an FEA-based cathode? And finally, how can space charge compensation be employed to maintain the initial low emittance of the FEA-based beam? It was therefore decided to build the 100 keV DC Gun Test Stand. This test stand allows for the first time to investigate the transverse beam dynamics of a bunched electron beam emitted by a pulsed FEA source.⁵ The test stand consists primarily of a diode configuration accelerating low emittance electron bunches from a gated FEA and a solenoid magnet to compensate for emittance blow-up due to space charge forces at low energies; in addition diagnostic equipment required to resolve the low emittances reached with such a setup is included in the test stand.

This design and the commissioning of this test stand as well as the first experimental results obtained are the topic of this dissertation. The thesis covers the theory to understand the beam parameter requirements of the LEG Project and the design simulations for the gun, solenoid magnet and diagnostics of the test stand. Reconstruction of the full transverse phase space of the electron bunches — ultimately allowing online emittance optimization of an FEA-based electron beam — is presented. Finally results of the performance of first FEA samples are shown together with a characterization of the transverse properties of the bunches emitted by these samples.

⁵Naturally the longitudinal properties of the bunch are of interest too, even more so in the first RF cavities or before and after bunching sections. To reduce the complexity of the test stand, it was decided that longitudinal properties will not be investigated at this test stand. A test stand for the first RF cavity or a prototype of the bunching section will however require diagnostic equipment to investigate longitudinal phase space.

1.5 Thesis Outline

The thesis will begin by giving definitions and explaining the physical concepts required to describe electron beams. The important parameters for the LEG Project will be derived.

The third chapter deals with the simulations performed to design the test stand's gun, solenoid magnet and diagnostics module. It will show which beam parameters are to be expected from the chosen design and how the diagnostic equipment has been specified.

Chapter four outlines the technical implementation of the test stand; it presents all test stand elements and features. In addition the methods by which the diagnostic equipment can be used to reconstruct the transverse phase space properties are introduced.

The fifth chapter details calibration measurements required for test stand operation and reports on commissioning of the test stand and startup experience.

Chapter six is dedicated to measurement data, its acquisition and the derived results. It will highlight characterization of electron bunches emitted by the first FEA samples. A comparison between measured data and simulation is made as well.

In the final chapter a summary of the results is given together with an outlook on suggested future measurements and test stand activities. A couple of conclusions relevant to the LEG Project are drawn.

The appendix contains design drawings of the test stand. This is followed by the acknowledgments. The bibliography can be found at the very end.

Chapter 2

Theory & Framework

Excellent introductions to the physical concepts used in this thesis can be found in [3, 6, 7, 8, 17, 18, 19]. This chapter introduces these concepts and derives relevant properties for the 100 keV DC Gun Test Stand. It is a condensed summary of the above mentioned literature with emphasis on the LEG Project goals.

2.1 Phase Space Distributions

In an accelerator electron bunches can easily consist of 10^{10} particles or more. In order to describe the dynamics of such a bunch, it is therefore suitable to use the 6D phase space distribution $\Psi(\vec{q}, \vec{p})$ which is a function of the spatial coordinates $\vec{q} = (x, y, z)$ and momenta $\vec{p} = mc\gamma\vec{\beta}$. Since it is a density function it can be physically understood as the probability of finding a particle at (\vec{q}, \vec{p}) . The distribution can be normalized by integrating over the entire 6D phase space volume Γ

$$Q = \int_{\Gamma} \Psi(\vec{q}, \vec{p}) d\Gamma. \quad (2.1)$$

This normalization yields the total charge contained in the bunch. Such a system can be described by a Hamiltonian if the forces acting on the parti-

cles can be derived from a potential (conservative system).¹ The total time differential

$$\frac{d\Psi}{dt} = \frac{\partial\Psi}{\partial t} + \dot{q}_i \frac{\partial\Psi}{\partial q_i} + \dot{p}_i \frac{\partial\Psi}{\partial p_i} \quad (2.2)$$

of a stationary distribution is simplified with

$$[\Psi, H] = 0 \quad (2.3)$$

and therefore reduces to

$$\frac{d\Psi}{dt} = 0. \quad (2.4)$$

This equation is known as *Liouville's theorem*. According to the theorem, particles in phase space behave like an incompressible liquid. Phase space trajectories cannot cross each other (except at a singularity).² It is important to note that Liouville's theorem applies to local phase space densities; filamentation (e.g. a mismatched bunch rotating in a nonlinear RF waveform) for example is not a violation of the theorem.

In accelerators there is a preferred direction given by the beam path along the longitudinal coordinate z . Therefore it is often convenient to use projections of the full 6D phase space distribution $\Psi(\vec{q}, \vec{p})$ onto the 4D transverse phase space distribution $\Psi_{\perp}(x, y, p_x, p_y)$ and the 2D longitudinal phase space distribution $\Psi_{\parallel}(z, p_z)$. A priori, Liouville's theorem does not apply to projected distributions in subspaces. However, if particle motion is fully decoupled in one coordinate q_c , that is if

$$\frac{\partial^2\Psi}{\partial q_c \partial q_i} = 0 \quad \forall q_i \neq q_c. \quad (2.5)$$

¹Not all particle dynamics in an accelerator can be described by a conservative system. Exceptions are synchrotron radiation, wave-mechanical effects, collisions between beam particles, collisions between beam particles and rest gas, etc. However, for the dynamics investigated in this thesis, the systems are properly described by a Hamiltonian.

²Particle trajectories crossing in phase space would mean that two particles have the same position and velocity at one moment but different values later.

Liouville's theorem can be applied to the projected phase space distribution

$$\Psi_{n-1} = \int \Psi_n dq_c. \quad (2.6)$$

In general, motion in particle bunches in accelerators is coupled, but in certain simple situations (for example a perfect FODO channel with no skewed elements) it can be useful to approximate by using uncoupled subspaces of the full 6D phase space according to motion in the three spatial coordinates. In this approximation the phase space distribution is given by

$$\Psi(\vec{q}, \vec{p}) = \Psi_x(x, p_x) \Psi_y(y, p_y) \Psi_z(z, p_z). \quad (2.7)$$

It is important to note that Liouville's theorem does not apply to the projected distributions Ψ_i per se and that requiring constant local phase space density in one of the 2D subspaces Γ_i

$$\left. \frac{d\Psi_i}{dt} = 0 \right|_{i=x,y,z} \quad (2.8)$$

can a priori only be used as an approximation.

Phase space distribution density is a rather abstract quantity and not very handy to use in practice due to the large number of particles in a bunch. A self-evident attempt to simplify the description is therefore to introduce the statistical moments of a particle bunch distribution. The zeroth order moment has already been given in the normalization condition (2.1). The first order moment is given by

$$\langle \xi \rangle = \frac{1}{Q} \int \xi \Psi(\vec{q}, \vec{p}) d\Gamma. \quad (2.9)$$

For $\xi = q_i$ (spatial coordinates) this mean is the bunch centroid, commonly referred to as the bunch position. For $\xi = p_i$ this is the mean momentum. The second order moment is given by

$$\sigma_\xi^2 = \langle (\xi - \langle \xi \rangle)^2 \rangle = \langle \xi^2 \rangle - \langle \xi \rangle^2 = \frac{1}{Q} \int (\xi - \langle \xi \rangle)^2 \Psi(\vec{q}, \vec{p}) d\Gamma. \quad (2.10)$$

It is often more practical to use the standard deviation σ_ξ instead of the variance σ_ξ^2 (since the standard deviation σ_ξ has the same dimension as the variable ξ). The spatial standard deviations σ_{q_i} are commonly used as a measure for the beam size. These are RMS quantities defined for arbitrary distributions; the standard deviation σ does *not* indicate that bunches are assumed to have Gaussian distributions.

From these definitions, two widely used longitudinal parameters can also be derived: the momentum spread

$$\delta = \frac{\sigma_{p_z}}{\langle p_z \rangle} \quad (2.11)$$

and the peak current (assuming a Gaussian longitudinal distribution)³

$$\hat{I} = \frac{Q\beta c}{\sqrt{2\pi}\sigma_z}. \quad (2.12)$$

2.2 The Concept of Emittance

Essentially, there are two different approaches to introduce the concept of emittance. They originate from two different descriptions of a particle bunch in an accelerator, but they lead to equivalent definitions. Both will be given in this section.

2.2.1 Statistical Definition

The statistical moments derived in the last section can be used to define the area occupied by one standard deviation of a bunch in a plane in phase space

$$\tilde{A}_i = \pi \sigma_{x_i} \sigma_{p_i}. \quad (2.13)$$

³The equation makes use of the paraxial approximation $\beta_{x,y} \ll \beta_z \approx \beta$ which will be introduced in Eq. (2.18).

In accelerators there is often a correlation between a particle's position and momentum; the above definition can be corrected to take into account such a correlation⁴

$$\tilde{A}_i = \pi \sqrt{\langle (x_i - \langle x_i \rangle)^2 \rangle \langle (p_i - \langle p_i \rangle)^2 \rangle - \langle (x_i - \langle x_i \rangle)(p_i - \langle p_i \rangle) \rangle^2} \quad (2.14)$$

and normalized

$$A_i = \frac{\tilde{A}_i}{m_e c} = \pi \sqrt{\langle (x_i - \langle x_i \rangle)^2 \rangle \langle (\gamma \beta_i - \langle \gamma \beta_i \rangle)^2 \rangle - \langle (x_i - \langle x_i \rangle)(\gamma \beta_i - \langle \gamma \beta_i \rangle) \rangle^2}. \quad (2.15)$$

Phase space is usually not accessible directly since measurements reveal particle trace space properties; therefore it is convenient to use trace space. This leads to the definition of the *RMS emittance*

$$\varepsilon_i = \sqrt{\langle (x_i - \langle x_i \rangle)^2 \rangle \langle (x'_i - \langle x'_i \rangle)^2 \rangle - \langle (x_i - \langle x_i \rangle)(x'_i - \langle x'_i \rangle) \rangle^2}. \quad (2.16)$$

Without loss of generality, the 6D trace space coordinate system can be conveniently chosen centered with respect to the particle distribution ($\langle x_i \rangle = 0$, $\langle x'_i \rangle = 0$); the emittance can then be rewritten as

$$\varepsilon_i = \sqrt{\langle x_i^2 \rangle \langle x_i'^2 \rangle - \langle x_i x_i' \rangle^2}. \quad (2.17)$$

Under the following conditions

- monochromatic approximation: $\sigma_\gamma \approx 0$
- paraxial approximation: $u' \ll 1$

$$\beta_u = \frac{1}{c} \frac{du}{dt} = \frac{1}{c} \frac{du}{dz} \frac{dz}{dt} = u' \beta_z \approx u' \beta \quad (2.18)$$

the RMS emittance is easily related to the occupied phase space area by

$$\varepsilon_i = \frac{A_i}{\pi \gamma \beta} = \frac{\tilde{A}_i}{\pi m_e c \gamma \beta}. \quad (2.19)$$

⁴In order to apply Liouville's theorem, one is interested in local phase space density rather than in a global density and therefore the correlation is subtracted in the definition.

The RMS emittance is a geometrical emittance, i.e. it is the emittance as measured by an observer in the lab system. Due to *adiabatic damping* during acceleration, it reduces linearly with the energy increase [according to Eq. (2.19)]. Therefore it is convenient to define the *normalized RMS emittance*

$$\varepsilon_i^{(n)} = \frac{1}{m_e c} \sqrt{\langle x_i^2 \rangle \langle p_i^2 \rangle - \langle x_i p_i \rangle^2} \approx \gamma \beta \sqrt{\langle x_i^2 \rangle \langle x_i'^2 \rangle - \langle x_i x_i' \rangle^2} = \gamma \beta \varepsilon_i. \quad (2.20)$$

Thus the normalized RMS emittance is a measure of the phase space area occupied by the bunch. According to Liouville's theorem, $\varepsilon_i^{(n)}$ is only a constant of motion if particle motion is fully decoupled in i .

The emittance is defined for each spatial coordinate. The longitudinal emittance is $\varepsilon_{\parallel} = \varepsilon_z$; in this thesis if not otherwise specified, emittance always refers to the transverse RMS emittances $\varepsilon_x, \varepsilon_y$.

2.2.2 Optical Definition

In beam dynamics the optics of an accelerator are usually described by the Courant-Snyder parameters⁵ $[\beta, \alpha, \gamma]_u$ with

$$\begin{aligned} \alpha &= -\frac{\beta'}{2}, \\ \gamma &= \frac{1 + \alpha^2}{\beta}, \end{aligned} \quad (2.21)$$

which leads to the well known identity

$$\beta\gamma - \alpha^2 = 1. \quad (2.22)$$

If a bunch passes an optical system its measurable properties (given by the Σ -matrix) are determined by the optical system (given by the optical transfer

⁵These parameters are not to be confused with the relativistic velocity $\beta = v/c$ and energy $\gamma = (1 - \beta^2)^{-1/2}$.

matrix \mathcal{M}) and the bunch's “temperature” ε_u

$$\Sigma_u = \begin{pmatrix} \langle uu \rangle & \langle uu' \rangle \\ \langle uu' \rangle & \langle u'u' \rangle \end{pmatrix} = \varepsilon_u \mathcal{M}_u = \varepsilon_u \begin{pmatrix} \beta_u & -\alpha_u \\ -\alpha_u & \gamma_u \end{pmatrix}. \quad (2.23)$$

This “temperature” is the geometrical emittance of the bunch. From Eq. (2.22) it follows immediately that

$$\varepsilon_u = \sqrt{|\Sigma_u|} = \sqrt{\langle u^2 \rangle \langle u'^2 \rangle - \langle uu' \rangle^2}. \quad (2.24)$$

For particles in an accelerator, linear particle motion is described by

$$u'' + k(s)u = 0 \quad (2.25)$$

and it can be shown that [3]

$$\begin{pmatrix} u & u' \end{pmatrix} \mathcal{M}_u \begin{pmatrix} u \\ u' \end{pmatrix} = \beta u'^2 + 2\alpha uu' + \gamma u^2 = \varepsilon_u. \quad (2.26)$$

This equation states that the emittance is a constant of motion and that particle motion in real space is represented by an ellipse in trace space, in other words, the density lines in trace space are ellipses. This is depicted in Fig. 2.1.

The RMS beam size is given by

$$\sigma_u = \sqrt{\langle u^2 \rangle} = \sqrt{\beta_u \varepsilon_u} \quad (2.27)$$

and the absolute RMS divergence spread is given by

$$\sigma_{u'} = \sqrt{\langle u'^2 \rangle} = \sqrt{\gamma_u \varepsilon_u}. \quad (2.28)$$

Particles within 1 standard deviation of the spatial and angular distribution are enclosed by an ellipse with the area

$$A_u = \pi \langle u^2 \rangle \langle u'^2 \rangle \Big|_{\alpha=0} = \pi \sqrt{\beta_u \varepsilon_u} \sqrt{\varepsilon_u / \beta_u} = \pi \varepsilon_u. \quad (2.29)$$

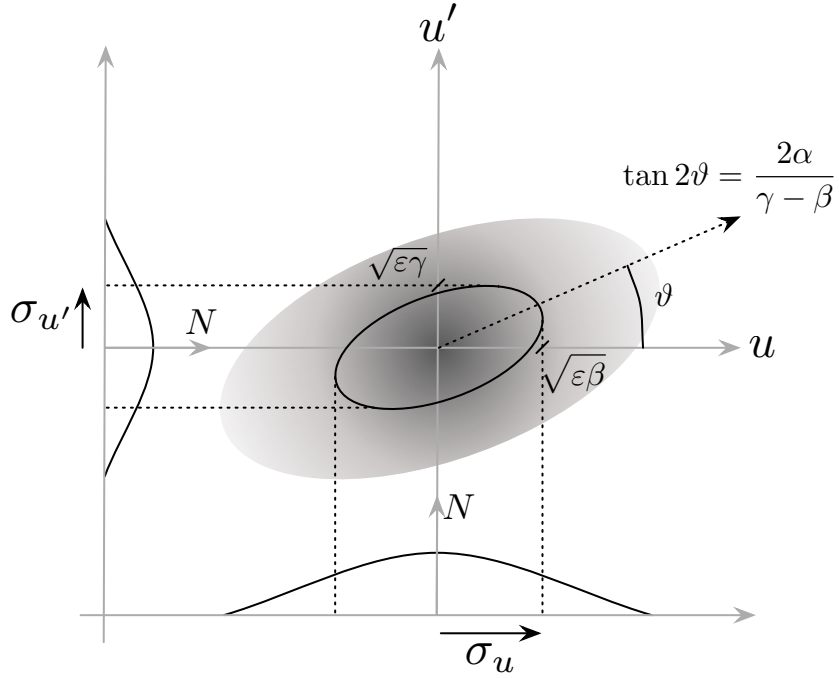


Figure 2.1: A particle bunch centered in trace space; density lines are ellipses. The relation between the trace space ellipse and the Courant-Snyder parameters is shown. The angle ϑ is the inclination of the ellipse; it is a measure for the bunch's divergence ($0 < \vartheta < \pi/2$) or convergence ($\pi/2 < \vartheta < \pi$).

The emittance derived in the beam optics approach (2.24) is a geometrical emittance; it is equivalent to the geometrical emittance derived in (2.17).

The factor π in Eq. (2.29) is often a source of confusion. The emittance defined here is the area of the ellipse divided by π . In some literature the emittance is defined as the area of the ellipse and therefore has to include the factor π . Depending on the underlying definition used emittances are sometimes given in units of [m rad] or [π m rad].

2.2.3 The Envelope Equation

A direct solution of Eq. (2.25) cannot be given without knowledge of the function $k(s)$ given by the optics of the accelerator.

However, the ansatz

$$u(s) = A \xi(s) \cos(\phi(s) + \phi_0), \quad (2.30)$$

which is similar to a harmonic oscillator, but with a variable phase $\phi(s)$ and an amplitude function $\xi(s)$, can be inserted into the equation of motion (2.25) rendering the phase

$$\phi(s) = \int_0^s \frac{ds}{\xi^2} \quad (2.31)$$

and the amplitude equation

$$\xi'' + k(s)\xi - \frac{1}{\xi^3} = 0, \quad (2.32)$$

which again depends explicitly on the optics of the accelerator given by $k(s)$.

Differentiation of Eq. (2.30) leads to an ellipse equation

$$\xi^2 u'^2 - 2\xi\xi'uu' + \left(\xi'^2 + \frac{1}{\xi^2}\right)u^2 = A^2, \quad (2.33)$$

which is identical to Eq. (2.26) for

$$\begin{aligned} \varepsilon_u &= A^2, \\ \beta_u &= \xi^2, \\ \alpha_u &= -\xi\xi' = -\frac{\beta'_u}{2}, \\ \gamma_u &= \xi'^2 + \frac{1}{\xi^2} = \frac{1 + \alpha_u^2}{\beta_u}. \end{aligned}$$

With $\sigma_u = \sqrt{\beta_u \varepsilon_u} = \xi \sqrt{\varepsilon_u}$ the envelope equation is derived

$$\sigma_u'' + k(s)\sigma_u - \frac{\varepsilon_u^2}{\sigma_u^3} = 0. \quad (2.34)$$

It is important to note here that the optics of an accelerator define the amplitude function entirely as shown in Eq. (2.32). The amplitude function is therefore independent of the particle ensemble inserted into an accelerator.

The envelope function however, depends on the optics *and* the emittance as can be seen in Eq. (2.34).

It can be shown [20] that space charge forces (see Section 2.4) can be included in the envelope equation leading to its final form⁶

$$\sigma_u'' + k(s)\sigma_u - \frac{\varepsilon_u^2}{\sigma_u^3} + \frac{K}{\sigma_u} = 0, \quad (2.35)$$

where K is the *generalized perveance* of the beam

$$K = \frac{2I}{I_A (\beta\gamma)^3}, \quad I_A = \frac{4\pi\varepsilon_0 m_e c^3}{q} \approx 17 \text{ kA}, \quad (2.36)$$

where I is the peak current of the bunch and the constant I_A is called the *Alfvén current*.

The envelope equation represents the equation of a (damped) harmonic oscillator with two additional terms: a term holding the emittance and a term holding the perveance. The emittance term is a consequence of Liouville's theorem: it ensures the beam size cannot shrink to infinitely small size. The perveance term is the so-called space charge term: it states that repulsive self forces within the beam lead to growth of the beam size. It is common to calculate the ratio of the space charge and emittance terms

$$R_{\text{sc}} = \frac{K/\sigma_u}{\varepsilon_u^2/\sigma_u^3} = \frac{K \sigma_u^2}{\varepsilon_u^2} = \frac{2 I \sigma_u^2}{I_A \beta\gamma (\varepsilon_u^{(n)})^2}. \quad (2.37)$$

Particle bunches with $R_{\text{sc}} \gg 1$ are *space charge dominated* or laminar; these are bunches with high peak current. Particle bunches with $R_{\text{sc}} \ll 1$ are *emittance dominated* or thermal.

2.2.4 Slice and Projected Emittance

The previously introduced emittance is considered a property of the entire bunch. In a SASE X-FEL it is however of interest to know the emittance

⁶This form of the envelope equation is for coasting beams. If the beam is accelerated $\gamma' \neq 0$, an additional damping term $\frac{\gamma'}{\beta^2\gamma}\sigma'$ has to be inserted. This is the adiabatic damping term which states that beam size decreases under acceleration.

within a temporal/longitudinal slice of the bunch; this is the so-called *slice emittance*. The motivation is essentially given by two considerations:

- In a SASE X-FEL the coherent radiation has its origin in the microbunching of the particle bunch in the undulator and hence it is of interest to know the emittance within the microbunches as they are the actual sources of the radiation.
- Space charge forces (see Section 2.4) depend on the longitudinal position within the bunch due to the longitudinal charge modulation [20]. These forces act as defocusing lenses of varying strength. After a drift different parts of the bunch will have rotated around the origin of trace space at different frequencies. To an observer in the lab system this appears as a “smearing out” of trace space distribution (see Section 2.5.2).

Since the overall bunch emittance originates from a projection of all the slice distributions it is always larger than the slice emittances. The overall bunch emittance is referred to as the *projected emittance* to avoid confusion. In this thesis, unless otherwise specified, emittance always refers to projected emittance.

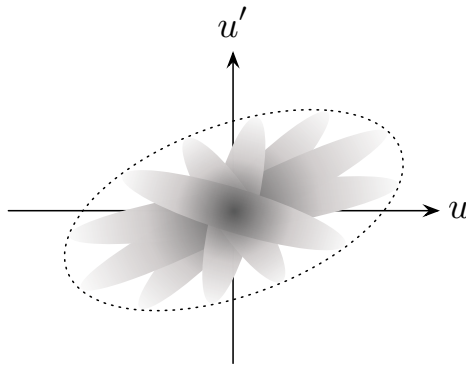


Figure 2.2: A bunch in trace space: different slices of the bunch have different ellipses. Together they form the projected emittance which is the emittance of the entire bunch.

Figure 2.2 is a simple illustration how a bunch consisting of low emittance slices can have a much larger projected emittance. Most emittance measurement techniques make use of screens that image the entire bunch and hence deliver projected emittances. If a time-resolving measurement technique is used (for example a streak camera) where the beam profile is determined for different parts of the bunch, the slice emittance can be measured.

In simulations usually the entire bunch data is generated at a given time step and emittance values derived are projected emittances. If slice emittances need to be known, a simple calculation can be used as an approximation [21]: A weighting function is introduced

$$w_i = e^{-\frac{(t_i-t_0)^2}{2\sigma_t^2}} = e^{-\frac{(z_i-z_0)^2}{2c^2\beta_z^2\sigma_z^2}} \quad (2.38)$$

with the corresponding normalization factor

$$W = \sum_{i=1}^N w_i. \quad (2.39)$$

Averages are then calculated using the weighting function for a slice located at z_0 and with a length σ_z according to

$$\langle u^2 \rangle = \frac{1}{W} \sum_{i=1}^N w_i u_i^2 \quad (2.40)$$

and similarly for $\langle u'^2 \rangle$ and $\langle uu' \rangle$. These averages can then be used to calculate the slice emittance (see Section 3.4).

2.3 Brightness

As mentioned in the introduction, brightness is the figure of merit for light sources. The brightness of a light source is the brightness of its photon beam which is directly connected to the brightness of the electron beam driving the light source. A definition of both the electron and photon beam brightness is given in this section.

2.3.1 Definition

Electron Beam Brightness

In the scope of a SASE X-FEL a high-quality electron beam can be characterized by

- high electron flux $\propto \frac{\dot{Q}}{\sigma_x \sigma_y}$
- high peak current $\propto \frac{Q}{\sigma_z}$
- small energy spread $\propto \sigma_\gamma$
- small angular spread $\propto \sigma_{x'} \sigma_{y'}$

Therefore an adequate figure of merit for the electron beam in a SASE X-FEL is the *brightness* defined as

$$\mathcal{B} = \frac{Q}{\varepsilon_x \varepsilon_y \varepsilon_z}. \quad (2.41)$$

It is essentially the electron density in 6D phase space. As defined for the emittance, there is a normalized brightness independent of the beam energy

$$\mathcal{B}^{(n)} = \frac{Q}{\varepsilon_x^{(n)} \varepsilon_y^{(n)} \varepsilon_z^{(n)}} \approx \frac{\mathcal{B}}{(\gamma\beta)^3}. \quad (2.42)$$

It is sometimes practical to use projections of 6D brightness. Examples are the normalized transverse brightness

$$\mathcal{B}_\perp^{(n)} \propto \frac{Q}{\varepsilon_x^{(n)} \varepsilon_y^{(n)}} \quad (2.43)$$

and the normalized longitudinal brightness

$$\mathcal{B}_\parallel^{(n)} \propto \frac{Q}{\sigma_\gamma}. \quad (2.44)$$

Photon Beam Brightness

As for the electron beam, brightness can be defined for the photon beam. There are several definitions in use depending on their application. Sometimes brightness is given as photon flux per solid angle and relative bandwidth [6]

$$\mathcal{B}_\gamma = \frac{\dot{N}_\gamma}{\pi^2 \sigma_r^2 \sigma_{r'}^2 (d\omega/\omega)} \quad (2.45)$$

with a simple expression for the maximum brightness for a diffraction limited photon beam [see Eqs. (1.1) and (1.2)]

$$\mathcal{B}_{\max} = \dot{N}_\gamma \frac{4}{\lambda^2} \left(\frac{d\omega}{\omega} \right)^{-1}. \quad (2.46)$$

For the bandwidth term ($d\omega/\omega$) used to normalize the photon flux, it is quite common to use 0.1% of the energy bandwidth. Depending on the literature brightness is sometimes also called brilliance.⁷ In this thesis the brightness defined in Eq. (2.41) will be considered the figure of merit for a SASE X-FEL injector. Brightness is maximized by reaching high peak current while retaining lowest emittance.

2.3.2 Brightness Limitations

Since brightness is the figure of merit for the design of a SASE X-FEL it is of interest to investigate brightness limitations. Assuming a source is found capable of delivering the required peak current, the main interest focuses on emittance contributions limiting the achievable brightness:

- **Cathode:** Surface roughness of the emission area and thermal emittance: Initially electrons are emitted in various directions with finite

⁷In [3] it is suggested to use “Brilliance” (brilliance) for the here defined brightness and “Leuchtdichte” (brightness) for the photon flux per solid angle, per 0.1% BW, and per unit current of the electron beam.

energy; a minimum contribution comes from the thermal energy of the electrons (Maxwell-Boltzmann distribution), i.e. ≈ 25 meV at room temperature (see Section 2.6.1).

- **Space charge forces** at low energies during first stages of acceleration. At high energies these forces become negligible, but in the first part of an accelerator they can lead to substantial emittance growth (see Section 2.4).
- **RF nonlinearities:** The bunch will be accelerated in RF cavities where transverse and more importantly longitudinal variations of the electric field are present. These variations can lead to RF-induced emittance growth.

The total “emittance budget” of the accelerator is given by [22]⁸

$$\varepsilon_{u,\text{tot}}^{(n)} \geq \varepsilon_{u,\text{th}}^{(n)} + \varepsilon_{u,\text{sc}}^{(n)} + \varepsilon_{u,\text{rf}}^{(n)}. \quad (2.47)$$

This equation states that optimization of one of the emittance terms is inadequate and all contributions have to be minimized. In the scope of the LEG Project it is thus not sufficient to find a source delivering high peak current with low thermal emittance; it is just as important to conserve this low emittance during the first stages of acceleration and throughout the RF accelerating structures up to the undulator.

2.4 Space Charge Forces

In a SASE X-FEL injector high charge densities are required. Thus the electric charge of the electron bunch becomes a major contribution to the

⁸In some literature it is indicated that the total emittance is approximated by the quadratic sum of the emittance contributions due to statistical independence. This is absolutely wrong. The total emittance can be much larger; in the best case the total emittance is the sum of the contributions.

forces acting on individual electrons in the bunch. The interaction between the bunch charge and a bunch particle can be direct or indirect.

Electromagnetic fields excited by the bunch in the surrounding structures can act back on parts of the bunch or on a following bunch. These so-called *wake field effects* are an indirect mechanism. They are important for transport over long distances (for example bunches stored in a storage ring) or when a bunch is close to conducting surfaces (for example cavity irises or narrow-gap undulators). These effects will however not be further investigated in this thesis.

Direct interaction, where the charge of the entire bunch acts on a single particle within the bunch is referred to as *space charge effect*. Space charge forces lead to a distortion of the bunch's phase space distribution, introduce coupling between different conjugate coordinates, and therefore projections of phase space density on phase planes can change as well. In general, space charge forces can lead to emittance growth.

Space charge forces are primarily a concern at low energies. This can be demonstrated using a simple model for the bunch in an accelerator: the continuous uniform cylindrical beam model [20]. From Gauss' law the radial electric field of the bunch is expressed by

$$\iint \vec{E} d\vec{\sigma} = \frac{1}{\varepsilon_0} \iiint \rho dV \quad \longrightarrow \quad E_r = \frac{\rho r}{2\varepsilon_0} = \frac{I r}{2\varepsilon_0 \pi r_0^2 \beta c} \quad (2.48)$$

for $r \leq r_0$ where r_0 is the bunch radius. From Ampère's law the angular magnetic field is derived

$$\oint \vec{B} dl = \mu_0 \iint J d\vec{\sigma} \quad \longrightarrow \quad B_\theta = \frac{\mu_0 J r}{2} = \mu_0 \frac{I r}{2\pi r_0^2} = \mu_0 \varepsilon_0 \beta c E_r. \quad (2.49)$$

Thus the Lorentz force has only a radial component

$$F_r = q (E_r - \beta c B_\theta) = q(1 - \beta^2) E_r = \frac{q E_r}{\gamma^2}. \quad (2.50)$$

The radial force is linear in r and scales inversely with the square of the energy. At high energies the attractive magnetic force compensates the repulsive electric force.

Transverse motion with space charge forces can be expressed as

$$\frac{d^2u}{dt^2} = \frac{qE_u}{\gamma^3 m_e} \Big|_{u=x,y}. \quad (2.51)$$

In a continuous uniform beam the longitudinal space charge forces have to cancel due to symmetry. For a real bunch with finite length the variation of the charge distribution at the head and tail gives rise to space charge forces. Equation (2.51) holds also for longitudinal motion although there is no magnetic focusing force in longitudinal direction: For $p_z = qE_z$ relativistic corrections lead to the identical result

$$\frac{d^2z}{dt^2} = \frac{qE_z}{\gamma^3 m_e}. \quad (2.52)$$

This explains why space charge defocusing is primarily a concern in the non-relativistic regime.

In a high-brightness injector system the bunch starts with nearly zero energy. Therefore, space charge forces are not relativistically reduced and thus lead to an immediate blow-up of the projected emittance. In order to minimize this blow-up the first acceleration sections have to be designed to accelerate the bunch as quickly as possible to energies where space charge forces become negligible ($\gamma > 10 \rightarrow E_{\text{kin}} > 5 \text{ MeV}$).

An obvious solution would be to accelerate the bunches in a pulsed DC accelerating gap right after emission. Assuming 1 GV/m accelerating gradient, a 5 mm gap would be sufficient. It has however been shown [23] that highest accelerating gradients are not purely beneficial due to the large nonlinear electric field components at the anode iris leading to strong emittance growth. The choice of the proper accelerating gradient and length of the accelerating gap will therefore be carefully balanced between highest acceleration and tolerable field nonlinearities.

2.5 Phase Space Manipulation Techniques

Previously it was assumed that a source with high peak current and low emittance has to be found for the success of PSI's LEG and X-FEL projects. Immediately the question arises if a source's peak current can be further increased or if any emittance growth can be reduced further along the accelerator in order to reach the requirements of the undulator for SASE X-ray lasing. Three examples of such phase space manipulation techniques are given here. It will be shown that two of the proposed techniques are necessary and one is not applicable in a X-FEL.

2.5.1 Bunch Compression

Since emittance blow-up due to space charge forces at low energies has its origin in the high charge densities of the bunch, one would prefer acceleration of low charge densities until the relativistic reduction of space charge forces prevents emittance blow-up. This however requires the charge density to be increased at high energies in order to reach the necessary peak current. Liouville's theorem does not prohibit such a scheme as long as the total phase space density is left unchanged in the process. Essentially, if the longitudinal bunch size σ_z is reduced in order to increase the charge density (hence the expression "bunch compression"), Liouville's theorem (in the approximation that the longitudinal phase plane is decoupled from transverse phase space and thus longitudinal emittance is preserved) requires the energy spread σ_γ to increase

$$\varepsilon_z^{(n)} = \text{const} \quad \longrightarrow \quad \sigma_z \sigma_\gamma = \text{const}. \quad (2.53)$$

This statement immediately leads to an expression for the amount of possible compression

$$\frac{\sigma_z}{\sigma_{z,0}} = \frac{\sigma_{\gamma,0}}{\sigma_\gamma}. \quad (2.54)$$

Technically this can be implemented by velocity bunching (positive correlation between energy and phase in the bunch plus a drift space) or by using

dispersive schemes. In the LEG Project bunch compression will be used at high energies where space charge forces are relativistically reduced. At these energies velocity bunching is inefficient and therefore a dispersive method is appropriate.

In such a compression scheme the gun delivers a long electron bunch with reduced charge density thus reducing emittance blow-up due to space charge forces. The bunch is immediately accelerated to ultra-relativistic velocities where space charge forces “freeze out”. At this point a linear energy chirp is introduced in longitudinal phase space. This can be accomplished by injecting the bunch into an RF cavity close to the positive zero-crossing where the energy-phase relation is approximately linear. Once the bunch has acquired the energy chirp it then passes a dispersive section (in a linac this is usually a magnetic chicane consisting of three or four dipole magnets) where the bunch is compressed due to its energy variation: The head of the bunch has a higher energy and thus travels on a longer dispersive path through the chicane while the tail at lower energy travels on the shorter inner path; together this leads to a shorter resulting bunch length $\Delta\sigma_z < 0$. Liouville’s theorem is not violated by this procedure because the energy spread has increased (energy chirp in RF cavity) while the bunch length decreased.

Magnetic chicanes for bunch compression can however also be a source of emittance blow-up. Such blow-up can arise from chromatic aberrations (non-linear dispersive effects in the horizontal plane) or from coherent synchrotron radiation (CSR) where the significant amount of radiation generated in the bends (coherent emission) leads to a time-correlated energy spread in the bunch. Since the energy spread is generated in a dispersive section, it transforms into angular spread and causes projected emittance growth [24, 25]. It has also been demonstrated that space charge forces can lead to emittance growth in bending magnets even at high energies [26]. Therefore magnetic chicanes require careful design in order to ensure that the emittance of the bunch is actually reduced.

Since there are presently no known low emittance sources capable of delivering the 1.5 kA of peak current required by the PSI X-FEL undulator and in order to reduce space charge forces in the low energy regime, it is foreseen to make use of magnetic bunch compression with two separate chicane sections, giving in total a compression factor of roughly 15 [15].

2.5.2 Emittance Compensation

Linear Emittance Compensation

It has been detailed by Carlsten [27] that to first order transverse space charge forces act as a defocusing lens with a strength depending on the longitudinal position within the bunch (corresponding to the longitudinal variation of charge density). Due to the variation of these forces, in a focusing channel different slices in the bunch will rotate at different frequencies around the origin in phase space. This leads to a projected emittance which is larger than the slice emittance. Carlsten proposes an emittance compensation scheme where proper focusing rotates phase space distributions of individual slices in such a way that the linear part of the defocusing space charge force is compensated and thus the growth of projected emittance is strongly reduced.

Figure 2.3 demonstrates how the projected emittance of a bunch grows due to space charge forces and how proper focusing can be used to compensate for this growth. In *a)* the bunch's particle distribution is shown in configuration space just after emission. *b)* shows the corresponding trace space representation with low emittance; there is no correlation between position and momentum. *c)* is after a drift from the source; different slices of the bunch show different correlations in trace space (according to the longitudinal variation of space charge forces) leading to an increased emittance. *d)* shows the bunch just after passing the focusing lens; emittance has further increased. *e)* is after a drift space; the bunch is still converging. *f)* is after further drift, just before the beam waist; while the bunch has continued to

converge in the drift, space charge forces act as a defocusing lens. *g)* shows the bunch right after the beam waist; the slices are now starting to align in trace space and thus the projected emittance decreases. *h)* is after a further drift; the slices have aligned and the emittance has been reduced compared to the the initial emittance seen in *c)*. The remaining emittance increase is caused by nonlinearities in the space charge forces which cannot be compensated by this scheme.

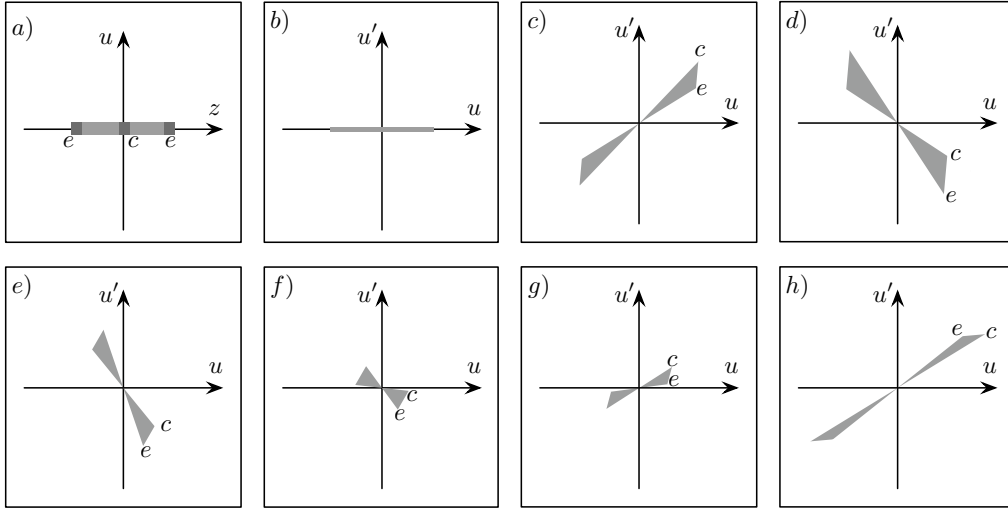


*Figure 2.3: Schematic showing emittance compensation as proposed by Carlsten [27]. The label c denotes the bunch center, label e denotes bunch ends. *a)* shows the particle distribution of a bunch just after emission in configuration space. *b) – h)* show the bunch evolution (focusing lens and compensation channel) in trace space. The difference in emittance between *c)* and *h)* is the result of emittance compensation. Image according to [7].*

Essentially, the proper overlap of the slice distributions in trace space renders the lower projected emittance values at the end of the compensation channel. Direct experimental evidence for this emittance compensation picture is given in [28] where the emittances of individual slices of a bunch are measured in order to directly observe the emittance compensation process.

If an emittance minimum can be achieved at a location where the bunch undergoes strong acceleration, space charge forces will “freeze out”, preserving the low emittance attained through compensation. Such a scheme can be implemented by using a solenoid magnet to focus the bunch in both transverse directions just after emission. At the location of minimum emittance it enters an RF cavity and is accelerated to relativistic energies. It is foreseen to use solenoid magnets for emittance compensation in the LEG Project’s injector system [15] just after the DC acceleration gap and before the 1.5 cell 2-frequency injector cavity.

Busch’s Theorem and Bucking Coils

At the entrance of a solenoid magnet the magnetic fringe field acts on the particle bunch. If $z = 0$ is a location far away from the magnet and z_0 is at the solenoid magnet’s center, the magnetic field can be expressed by

$$\begin{aligned}\vec{B}(z = 0) &= 0, \\ \vec{B}(z_0) &= B_0 \vec{e}_z, \\ B_\theta &= 0,\end{aligned}\tag{2.55}$$

where the condition for B_θ is due to rotational symmetry. The solenoid field between 0 and z_0 is given by

$$\vec{B} = B_r \vec{e}_r + B_z \vec{e}_z.\tag{2.56}$$

The transverse momentum of a particle is then

$$p_\theta = \int_t F_\theta dt = \int_t e \frac{dz}{dt} B_r dt = \int_z e B_r dz.\tag{2.57}$$

Using Gauss' theorem

$$\begin{aligned}
0 &= \iiint_V \vec{\nabla} \cdot \vec{B} dV = \iint_{\partial V} \vec{B} \cdot d\vec{\sigma} \\
&= \int_z \int_0^{2\pi} B_r R d\theta dz + \int_0^{2\pi} \int_0^R (B_{z,\text{in}} - B_{z,\text{out}}) r dr d\theta \\
&= 2\pi R \int_z B_r dz + \int_0^{2\pi} \int_0^R \Delta B_z r dr d\theta \\
&= 2\pi R \frac{p_\theta}{e} + \pi R^2 \Delta B_z.
\end{aligned} \tag{2.58}$$

This gives an expression for the angular momentum acquired by the particle in the solenoid fringe field; it is known as *Busch's theorem*

$$p_\theta = -\frac{eR}{2} \Delta B_z, \tag{2.59}$$

where $\Delta B_z = B_0$ for the conditions given in (2.55). Busch's theorem states that a particle entering the solenoid off axis receives an angular kick proportional to the particle's displacement from the beam axis and the solenoid's longitudinal magnetic field strength. When the particle exits the solenoid it will receive the reverse kick canceling the entry kick and thus the solenoid's total angular momentum contribution is zero. However, if there is a residual magnetic field on the cathode plane, this compensation mechanism does not lead to full cancellation and hence the particle acquires additional angular momentum. Since this corresponds to an increase in emittance, it has to be avoided by all means.

If the solenoid magnets are installed in vacuum, negligible residual magnetic field on the cathode can be accomplished by enclosing the solenoid windings in a magnet iron (high relative magnetic permeability μ_r) yoke casing to confine the magnetic field. If the solenoid magnets are installed outside of the vacuum system, the yoke will have a large aperture to hold the vacuum chamber and hence the magnetic field will not be sufficiently confined leading to "field leak" onto the cathode. Therefore, *bucking coils* (counter coils) are installed in the vicinity of the cathode and tuned to exactly cancel any

residual magnetic field on the cathode. It has been demonstrated that proper tuning of the bucking coil can reduce the final bunch emittance by substantial amounts; a very nice example is given in [29] where the properly adjusted bucking coil reduces the emittance by almost a factor 2.

Nonlinear Emittance Compensation

As indicated in Fig. 2.3 the proposed compensation scheme can only compensate linear space charge forces. Nonlinear forces lead to emittance blow-up which cannot be compensated by this scheme [hence the finite emittance increase shown in schematic *h*) of Fig. 2.3]. It has however been proposed [30] to counteract nonlinear space charge blow-up by accelerating the electron bunch in nonlinear electrostatic fields where nonlinear electric field components cancel the nonlinear space charge components. In the initial accelerating gap, nonlinearities of the electric field are to be expected mainly at the anode iris as a consequence of the rounded electrode surfaces close to the beam path. It is therefore to be expected that proper dimensioning of the anode iris, electrode angle, etc. can lead to a reduced emittance at the exit of the gun. In Section 3 this approach will be taken and simulations will demonstrate that transverse projected emittance can be reduced through proper design of the DC accelerating diode configuration.

2.5.3 Radiation Damping

Bunch compression and emittance compensation work within the boundaries set by Liouville's theorem. It is also of interest to investigate techniques to reach low emittance outside of the Liouville constraints. One such method is to use radiation damping to reduce the phase space volume occupied by the bunch thus reducing the emittance. This technique, also referred to as *cooling*, is widely used in storage ring based synchrotron sources or in high energy accelerator *damping rings*.

The concept makes use of the fact that synchrotron radiation has a longitudinal and transverse momentum component while in the RF cavities the bunch is accelerated only in the longitudinal direction. This mechanism leads to a reduction of transverse momentum over many revolutions and is therefore called *adiabatic damping*. Because the emission of synchrotron radiation is a quantum process an equilibrium transverse emittance is reached. In addition, throughout the damping ring evolution the bunch length and energy spread reach an equilibrium longitudinal emittance influenced by the RF bucket. The resulting bunch length is much larger than what a typical S-band linac generates and thus the damping ring would effectively reduce the peak current values attained by the linac injector system. This is therefore not a suitable method to reach low emittance in a SASE X-FEL.

2.6 Electron Emission

This section compares present-day electron sources in the scope of the LEG Project. It will motivate why the two most common electron emission principles are not suitable for the LEG Project and introduce field emission as a proposed alternative. In order to compare electron sources with respect to emittance it is important to first introduce the concept of source emittance and thermal emittance — the fundamental emittance limitation of any electron source.

2.6.1 Thermal Emittance

In an electron source electrons have to be excited from the bound state into vacuum. This requires a minimum excitation energy given by

$$\phi_{\min} = \phi_w - \Delta\phi_{\text{sch}}, \quad (2.60)$$

where ϕ_w is the work function of the source material and the correction term

$\Delta\phi_{\text{sch}}$ is given by

$$\Delta\phi_{\text{sch}} = \sqrt{\frac{qE_z}{4\pi\epsilon_0}}. \quad (2.61)$$

This is due to the *Schottky effect*: The effective work function is reduced when the emitting material is brought into an external electric field which effectively reduces the potential barrier.

In order to extract electrons from the material, they have to be excited by an energy $\phi_e > \phi_{\text{min}}$. The difference between this excitation energy and the total work function is the initial kinetic energy of the extracted electrons

$$E_{\text{kin},0} = \phi_e - \phi_{\text{min}} = \phi_e - \left(\phi_w - \sqrt{\frac{qE_z}{4\pi\epsilon_0}} \right). \quad (2.62)$$

A priori this initial kinetic energy is distributed among all momentum components in positive half-space (accelerating gap), i.e. into a 2π solid angle. The source size and the initial transverse momenta lead to an intrinsic emittance called *source emittance*.

Ultimately the minimum initial transverse energy of electrons coming from any source is the thermal energy $\frac{3}{2}k_B T$. A simple approximation [31] shows how this energy can be related to the transverse source emittance: The thermal energy of the cathode is given by

$$W = \frac{3}{2}k_B T \quad \longrightarrow \quad \langle W_u \rangle = \frac{1}{2}k_B T, \quad \langle W_z \rangle = \frac{1}{2}k_B T - \phi_{\text{min}}. \quad (2.63)$$

The transverse energy of the particle after emission is therefore given by

$$\frac{1}{2}m_e \langle v_u^2 \rangle = \frac{1}{2}k_B T \quad (2.64)$$

leading to a transverse momentum

$$\sqrt{\langle p_u^2 \rangle} = \gamma m_e \sqrt{\langle v_u^2 \rangle} = \gamma \sqrt{m_e k_B T}. \quad (2.65)$$

The source size is given by

$$\sqrt{\langle u^2 \rangle} = \frac{r_c}{2}. \quad (2.66)$$

Finally, since there is a priori no correlation between position and transverse momentum in the emission process

$$\langle u p_u \rangle = 0. \quad (2.67)$$

Thus the normalized emittance of the source is given by

$$\begin{aligned} \varepsilon^{(n)} &= \frac{1}{m_e c} \sqrt{\langle u^2 \rangle \langle p_u^2 \rangle - \langle u p_u \rangle^2} \\ &= \frac{\gamma r_c}{2} \sqrt{\frac{k_B T}{m_e c^2}}. \end{aligned} \quad (2.68)$$

This is the *thermal emittance*. It scales linearly with the source size and with the square root of the source temperature. It is the minimum emittance that can be achieved with a given source. The choice of a source for the LEG Project's gun will depend primarily on its thermal emittance.

The thermal emittance is a difficult property to measure. The emittance blow-up due to space charge forces and nonlinear RF field contributions usually mask the comparably low thermal emittance. A nice example of measuring a source's thermal emittance is given in [29] where short bunches are generated to avoid emittance growth due to RF fields and the bunch charge is successively reduced until an emittance threshold can be identified as the thermal emittance of the source.

2.6.2 Survey of Electron Emission Sources

This section will present the two most common emission principles used in electron sources. The underlying physics will be briefly introduced and it will be explained why both source types do not fulfill the requirements set up by the LEG Project. The following section will then introduce an alternative concept proposed for the LEG Project.

Thermionic Emission Sources

Thermionic emission sources were the first electron sources available [18]. Essentially electrons are heated to sufficiently high temperatures where they can escape the conduction band and enter vacuum. The emission current is given by the *Richardson-Dushman law* [32]

$$J = AT^2 e^{-\phi_w/(k_B T)}, \quad (2.69)$$

where $A \approx 120 \text{ A K}^{-1} \text{ cm}^{-2}$. This illustrates that in order to reach sufficiently high currents, thermionic cathodes have to be operated at temperatures in the vicinity of 2000 K. As an example, for copper with $\phi_w = 4.6 \text{ eV}$ the maximum current density at $\approx 1950 \text{ K}$ ($T_{\text{melt}} \approx 3000 \text{ K}$) is limited to $\approx 500 \mu\text{A}/\text{cm}^2$. Hence larger emitting surfaces are required. Operated at such high temperatures, already a 1 cm diameter cathode will have a source emittance of $\approx 2 \text{ mm mrad}$ according to Eq. (2.68).

Modern dispenser cathodes have reduced operation temperatures to $\approx 1000 \text{ K}$ and they reach currents as high as $\approx 100 \text{ A}/\text{cm}^2$ due to layers of material with lower work functions, however they are very sensitive to contamination and require excellent UHV conditions. In order to reach high currents, source sizes on the order of mm have to be taken into account. For these reasons many current X-FEL projects do not make use of thermionic guns. An exception is the SCSS Project [11, 13] where a single CeB_6 crystal with 3 mm diameter is expected to deliver 0.5 nC at $\approx 1700 \text{ K}$ with a thermal emittance of only 0.4 mm mrad!

A further disadvantage of thermionic sources is that they a priori deliver DC beams. In order to emit bunched beams the source needs to be pulsed. This can be done with a grid (leading to emittance dilution) or by using bunching cavities and choppers. The latter has to be done with great care in order not to spoil the emittance. The SCSS Project [11] is presently trying to experimentally prove the feasibility of this concept.

Photo-electric Emission Sources

Photo-electric emission is a quantum mechanical effect where the momentum of an incident photon is transferred to an electron which can then leave the bound state and enter vacuum. It has the distinct advantage over thermionic emission that electrons are emitted at room temperature which according to Eq. (2.68) leads to a lower thermal emittance.

There are many factors involved in the process (material, reflectivity, penetration depth, escape length, etc.); they are combined in the *quantum efficiency* (QE) which essentially gives the number of electrons emitted for a given number of incident photons. Typical QE values are below 10%. The number of emitted electrons is also a function of the incident laser power and wavelength [7]

$$N_e = 7.74 \cdot 10^{15} QE[\%] W[\mu\text{J}] \lambda^{-1}[\text{nm}^{-1}]. \quad (2.70)$$

A great advantage of photo-emission guns is that the time structure of the emitted particle bunch is given by the laser pulse. Due to the abundance of short pulse laser systems, ultra-short electron bunches can be achieved directly at the source through photo-electric emission.

Metals have shown current densities in excess of ≈ 100 kA/cm² [33]. However, such large current densities require high power lasers operating at very short wavelength. This short wavelength leads to a fundamental emittance limitation of photo-electric sources: At short wavelength the incident photon energy ϕ_e is large compared to the work function ϕ_w which leads to a large initial kinetic energy $E_{\text{kin},0}$, therefore to large transverse momenta and hence to a large source emittance. If a longer wavelength is used to reduce the initial kinetic energy, the number of emitted electrons reduces. This then requires that the laser illuminates a larger cathode area and according to Eq. (2.68) this increases the source emittance as well.

For a copper photo-cathode ($\phi_w = 4.6$ eV) with 1 mm diameter spot size the minimum achievable emittance is ≈ 1 mm mrad. At PITZ [34] a photo-

electric gun with a Cs₂Te cathode and a 253 nm UV laser is producing 1 nC electron bunches with a normalized transverse emittance of 1.6 mm mrad [35].

2.6.3 Field Emission and Field Emitter Arrays

Thermionic and photo-electric emission are currently both not capable of delivering the required 5.5 A peak current with a source emittance below 0.05 mm mrad as required by PSI's LEG and X-FEL Projects (see Table 1.2). Therefore an alternative electron source has to be found; due to Eq. (2.68) preferably a source operated at room temperature. Assuming electrons are emitted at room temperature and the thermal emittance has to be less than the required source emittance, this gives an upper limit for the emission area

$$r_c < \frac{2 \varepsilon_{\text{th}}}{\gamma} \sqrt{\frac{m_e c^2}{k_B T}} = 0.45 \text{ mm.} \quad (2.71)$$

In other words a source has to be found that delivers the required peak current with 0.05 mm mrad emittance from a surface of just 0.64 mm²!

Field Emission

A candidate for such an emission process is field emission. Field emission is a quantum process where electrons tunnel through the potential barrier from the conduction band into vacuum without being excited to energies above the work function. This has the advantage that initial kinetic energies are low, leading to lower initial transverse emittance and thus to a low source emittance.

In metals work functions on the order of a few eV lead to large potential barriers and thus to negligible tunneling probabilities. However, the Schottky effect [see Eq. (2.61)] can be used to reduce the potential barrier: the cathode is put in a strong external electric field which reduces the barrier thickness and thus increases tunneling probability. Since the Schottky effect

is a weak function of the electric field, very large fields (on the order of a few GV/m) are required to generate sufficient current densities. However, surface enhancement (local field line concentration due to surface roughness or protrusions from a surface) can reduce the required external field strength. The relation between applied electric field E , field enhancement⁹ β and field-emitted current is given by the *Fowler-Nordheim law* [7]

$$J_{\text{FN}} \approx 1.54 \cdot 10^{-6} \frac{\beta^2 E^2}{\phi_w} \exp\left(-6.83 \cdot 10^9 \frac{\phi_w^{3/2}}{\beta E}\right). \quad (2.72)$$

The common approximation given here is valid for $T < 600$ K and $J_{\text{FN}} < 10^{12}$ A/m² and omits a correction to ϕ_w (very weak polynomial in $\sqrt{\beta E}/\phi_w$).

Field emission can be triggered in essentially two ways: Either through the application of very high electric surface fields E or by applying moderate field strengths to a surface with a large geometric enhancement β . The former is unpractical since it requires field strengths of several GV/m whereas the latter is a well known effect — for example as a source of dark current around cavity irises.

Single Tip Emitters

One possibility to build a field emission electron source is to use a very sharp tip (“needle tip”) brought into an accelerating electric field on the order of a few MV/m. Since the tip has an extremely small surface ($\approx 1 \mu\text{m}$) the source emittance will remain below the requirements. If the external field is applied for a very short time, breakdown can be avoided, however, the amount of charge drawn from the tip is reduced as well. Previous experiments [36] with field emission from single tips have shown that the emitted current is

⁹It is common to denote field enhancement with β . It should not be mistaken with the relativistic velocity or the Courant-Snyder parameter! β is roughly the mean ratio between height and radius of a surface protrusion; it is dimensionless.

below 1 A over 1 ns and thus the peak current is too low for use in the LEG Project's gun.¹⁰

Field Emitter Arrays

Another approach to field emission from tips is to use an entire array of tips, a so-called *field emitter array (FEA)*. Such an FEA consists of many microscopic tips where each tip emits one *beamlet*. If a sufficient amount of tips is used large peak currents can be drawn. An example of a simple FEA is given in Fig. 2.4.

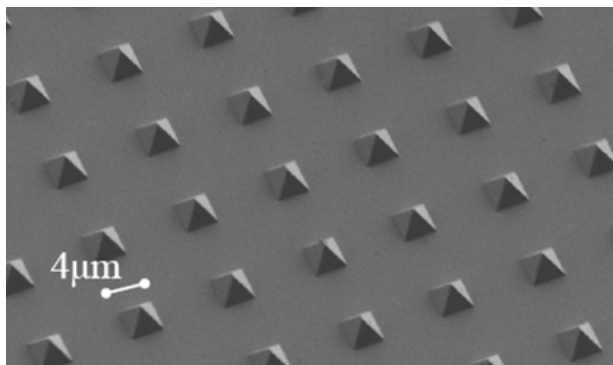


Figure 2.4: A simple FEA consisting of pyramidal molybdenum tips. The moulding technique used at PSI/LMN [38] produces 1 – 4 μm (depending on the wafer) high tips on top of a 200 nm molybdenum layer (evaporated) and a 300 μm nickel plate (electroplated). Image courtesy of [2].

One disadvantage of such an FEA is that considerable non-uniformities of emission current can arise due to the highly nonlinear dependence of field

¹⁰Most recent needle tip experiments [37] have shown that 5.5 A peak current can be extracted from a single tip by using laser-assisted field emission. In this technique a laser pulse is shone onto the cathode tip immediately before the HV pulse is applied. The laser photons have an energy below the work function so that photo-electric emission is avoided, but the photon energy excites the electrons in the conduction band thus reducing the potential barrier and increasing the tunneling probability. For a given external electric field the emission current is increased compared to pure field emission.

emission on the quality of the tips (i.e. variations of the local work function ϕ_w or field enhancement β). It has been shown in simulations that such non-uniformities can lead to strong emittance growth if the correlation length is large [23]. Great care has to be taken in the manufacturing process to make the tips identical in order to ensure uniform low emittance emission.

Pulsed HV has to be applied to trigger bunched emission from an FEA. It is technically very challenging to apply several MV within a few ps over a 1 mm gap in vacuum in order to generate \approx GV/m electric field to trigger emission. Therefore there are FEAs with a *gate layer*. Similar to the grid of a triode, this gate layer triggers emission from the tips if a positive bias voltage is applied to the gate layer with respect to the tip layer. Since the gate layer is only $\approx 1 \mu\text{m}$ away from the tips already rather low potential differences on the order of 100 V are sufficient to control emission from the tips. The gate layer has holes to allow the emitted electrons to pass from the tips to the accelerating gap. An example of a gated FEA is given in Fig. 2.5.

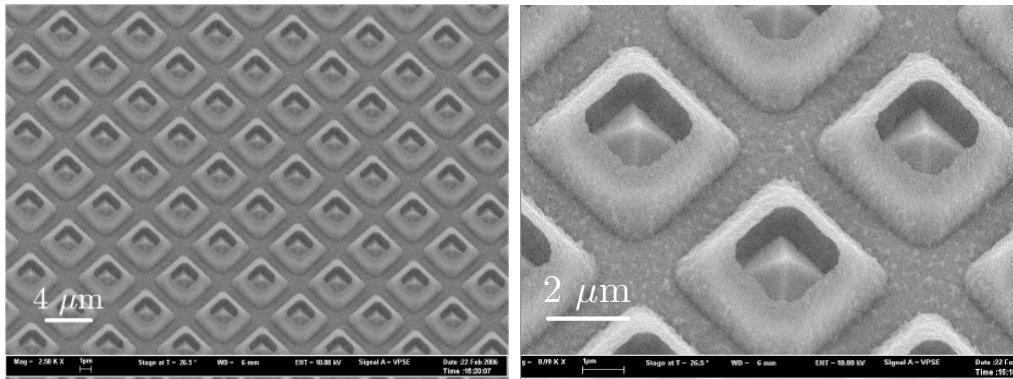


Figure 2.5: A gated FEA consisting of pyramidal molybdenum tips, a $1.2 \mu\text{m}$ thick silicon-oxide dielectric layer, and a $\approx 200 \text{ nm}$ molybdenum gate layer above the tips. The substrate used here is nickel. The FEA was produced at PSI/LMN [38]. Image courtesy of [2].

The disadvantage of the gated FEA is that electrons are emitted into a fairly large cone above each tip ($\approx 20^\circ$ opening angle [39]) due to nonlinearities of

the electric field between the tips and the gate. Although the emission areas on the FEA are very small, this leads to an increased source divergence, thus to higher source emittance and must therefore be avoided. One attempt to reduce the source divergence is to introduce an additional layer on top of the gate layer, the so-called *focusing layer*. This layer is put at a negative voltage bias with respect to the gate layer in order to reduce the transverse momentum of the extracted electrons. Simulations have shown that this leads to a reduced emittance compared to purely gated FEAs [40]. An example of a gated FEA with focusing layer is given in Fig. 2.6.

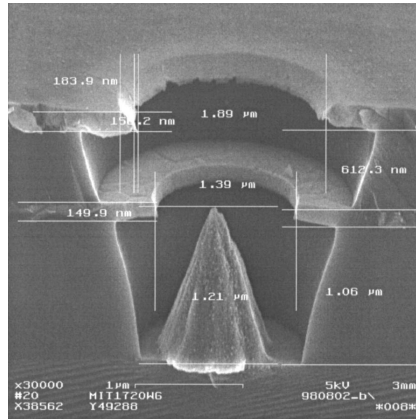


Figure 2.6: Cut through a single tip of a gated FEA with focusing layer produced at MIT. Dimensions are given. The tip on the silicon substrate is made from molybdenum (chromium added to reduce built-in stress), the gate and focusing layer from doped poly-silicon, and the insulator from silicon oxide. Image taken from [41].

In the experiments reported in this thesis *Spindt-type* (named after the inventor, Charles A. Spindt) gated FEAs from SRI International [42] have been used.¹¹ These cathodes have 50,000 approximately conical molybdenum tips

¹¹At the time the test stand was designed and built, there were no focused and gated FEAs available. The Spindt-type FEAs from SRI were the only gated source obtainable. In the meantime PSI/LMN [38] has started in-house production of gated and focused FEAs.

on a circular area with 1 mm diameter. The tips are grown on a p-doped silicon wafer with 10 – 30 Ω cm resistivity; they are separated from the gate layer by a 1 μ m thick dielectric layer. There is no focusing layer. The capacitance due to the overlapping electrodes has been measured to be 150 pF [36]. The FEA is on top of a typically 0.5 mm thick and 2.5 mm wide square silicon chip. The chip is attached to a TO-5 mount with one lead connected to the tips and four leads in glass insulators making a connection to the gate contact disk (see Section 4.3.2). A cut through the surface of a Spindt-type FEA is shown in Fig. 2.7.

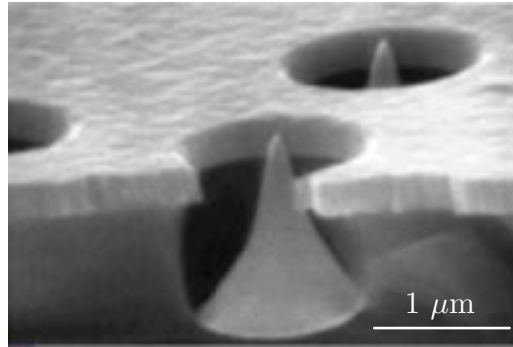


Figure 2.7: Cut through a Spindt-type FEA from SRI. The molybdenum tips are grown on a p-doped silicon substrate and are covered by a $\approx 1 \mu$ m thick dielectric made from silicon-oxide. It is covered by a molybdenum gate layer. Image taken from [42].

Chapter 3

Simulation

This chapter presents the simulations performed to specify the test stand gun, solenoid, and diagnostics. It is mainly a condensed summary of the extensive parameter studies performed for the “Test Stand Design Study” [43]. The first section begins by giving the input parameters for simulations of the actual gun; it then presents the derived geometry. The following sections focus on the solenoid and diagnostics simulations as well as design considerations. Finally an example of slice emittance simulation is given and two important tolerances for the gun setup are specified. Several components of the test stand are introduced in this chapter, but only the specifications relevant for beam dynamics simulations are given here. Design details and the actual technical implementation are presented in the next chapter.

3.1 Gun Design

The actual gun consists of the FEA, a surrounding cathode electrode structure, a gap where the 100 kV potential difference accelerates the emitted electrons, and the anode with an iris to allow particles to pass to the next section of the test stand. The commercial code MAFIA [44] was chosen to simulate the gun due to its availability on a dedicated workstation at PSI

and because it allows modeling of the exact gun geometry as well as tracking of particles with high precision through the accelerating gap. Due to the cylindrical symmetry of the gun the 2.5D module was used together with the electrostatic solver for the electric fields generated within the accelerating gap.

In parameter study runs up to 200,000 macro-particles were tracked through the structure. For quick checks and preliminary tests only 5,000 macro-particles were used in order to reduce computation time and memory requirements. As a result of convergence studies, most parameter studies were performed with 20,000 macro-particles; this reduced statistical noise to an insignificant amount while keeping run times manageable. Simulating the gun and tracking 20,000 macro-particles through the entire structure (≈ 500 mm) still required run times of up to 12 hours depending on the mesh applied.

A non-equidistant cylindrical mesh was chosen so that greatest mesh density could be generated around the actual beam path while using less mesh points further away from the beam axis in order to reduce run time and keep memory consumption within the maximum available amount (≈ 1 GB). The gun and solenoid geometry was fully resolved within $10\sigma_r$ around the beam. Further away from the beam axis the mesh density was reduced in two steps: first by a factor 3, then by a factor 5. Downstream of the solenoid the longitudinal mesh density was reduced by 60%. Appropriate mesh size was verified with convergence studies.

3.1.1 Input Parameters

The boundary conditions for the design of the gun were given by the maximum size available (roughly 60 mm diameter and 50 mm length) and the accelerating voltage of 100 kV. The voltage was chosen as the maximum voltage that can still be handled in an experiment bunker without the need for special insulation, oil tanks, etc. The cathode was to be put on -100 kV potential with respect to a grounded anode. At the time these simulations

were performed, first information on commercially available FEAs was being acquired; therefore assumptions for FEA dimensions and performance had to be made without samples or experimental evidence. The FEA was expected to deliver 100 mA peak current¹ in a Gaussian pulse cut off at $\pm 3\sigma_t$. A pulse width of $\sigma_t = 20$ ps was chosen because at the time it was the goal parameter for the LEG Project's pre-injector (in the meantime the value has been set at 14.5 ps, see Table 1.2). In order to get 100 mA peak current within a bunch with the chosen σ_t , a bunch charge of ≈ 5 pC was inserted according to

$$Q = \int I(t) dt = \int \hat{I} \exp\left[-\frac{(t-t_0)^2}{2\sigma_t^2}\right] dt. \quad (3.1)$$

It was expected that the FEA would occupy an area with ≤ 1.5 mm diameter and have an active emitting area of 100 μm . The initial energy is given by the gate voltage which was estimated to be around 50 V leading to a choice of $\gamma_0 = 1.0001$. The initial divergence was chosen to be zero as expected from an FEA with a focusing layer set to the appropriate voltage with respect to the gate layer. This leads to an approximated initial emittance of zero. Although the thermal transverse emittance of the here described FEA is roughly 10^{-8} m rad according to Eq. (2.68), the emittance growth due to space charge forces is expected to be much larger; therefore assuming a source divergence of zero will not introduce a significant error. A summary of the input parameters is given in Table 3.1.

3.1.2 Optimization

Considerations and Strategy

The simplest approach to a gun would be to think of two metallic plates where one holds the FEA (cathode) and the other contains a small hole, the

¹This is considerably less than required by the LEG Project (see Table 1.2), but it is sufficient to form a space charge dominated beam according to Eq. (2.37).

Table 3.1: Input parameters for simulations of the gun.

Macro-particles	20,000
Cathode Potential	−100 kV
Active Emitter Radius	100 μm
Pulse Form	Gaussian, cut-off at $\pm 3\sigma_t$
Pulse Length σ_t	20 ps
Bunch Charge Q	5 pC
Initial Energy γ_0	1.0001

so-called *iris*, in order to allow particles to pass into the following structures (anode). This design is easy to implement, but it has a few drawbacks.

Firstly, the anode iris acts as a defocusing electrostatic lens and will produce a divergent beam. The nonlinearities of this field will also give rise to emittance blow-up (see the last part of Section 2.5.2). One way to counter-act these two effects is to use conical rather than flat electrodes in order to reduce the angle between the electrode surface and the beam axis to values below 90° . Similar to the so-called Pierce Angle [45] used to achieve laminar particle motion in the beam at the exit of the gun, an angle has to be found where the electrostatic focusing properties of the field in the gap compensate the defocusing electrostatic forces at the iris on one hand, and minimize the emittance at the end of the gun on the other.

Secondly, on the edge of the iris very high electric field strengths are to be expected due to the geometric field enhancement of a sharp edge. This local peak field strength has to be minimized to avoid HV breakdown which could severely damage the FEA. This can be accomplished by enlarging the iris radius and/or smoothing its edge to increase the radius of curvature. The level of smoothing is mainly given by the manufacturing process, but the radius is a degree of freedom that can be used to optimize. Of course increasing the iris radius will come at the expense of additional defocusing. Therefore,

optimizations of the iris size and electrode angle have to be performed iteratively to reach lowest emittance while maintaining manageable surface peak field strength.

Thirdly, the iris size has to be chosen large enough to avoid particle scraping. The bunch should pass the iris without any particle loss. Particle losses on the iris can lead to adsorption of anode surface molecules which are then ionized and back-bombarded onto the FEA possibly causing severe damage. In addition the iris channel² has to be widened with increasing length to prevent scraping of a divergent bunch after it has passed the actual iris entry.

Finally, the accelerating gap can be varied. Increasing the gap will reduce the peak surface fields, but it will also reduce the accelerating gradient and allow additional space charge blow-up which causes emittance growth. Therefore the shortest gap is chosen that will limit surface peak fields to 20 MV/m which is considered manageable under UHV conditions with clean and well polished surfaces [46].

Resulting Design

The design resulting from these considerations is shown in Fig. 3.1. A circular area with 1.5 mm diameter at the center of the cathode has been reserved for the FEA. The two electrodes have been put at a 65° angle with respect to the beam axis since simulations show this angle minimizes the emittance at the exit of the gun (see Fig. 3.2).

An iris radius of 0.5 mm was chosen in order to minimize emittance while still avoiding particle loss.³ This is depicted in Fig. 3.3 where the seemingly large

²The iris is not just a hole in a thin plate. It is rather a channel through the anode structure. Due to technical considerations the anode is expected to have a thickness of roughly 30 mm.

³In the test stand setup the iris radius has been increased to 750 μm since the finally installed FEA has an active emitting area with 500 μm radius rather than the originally expected 100 μm . For this FEA type, simulations showed that particle loss would occur for radii below 750 μm .

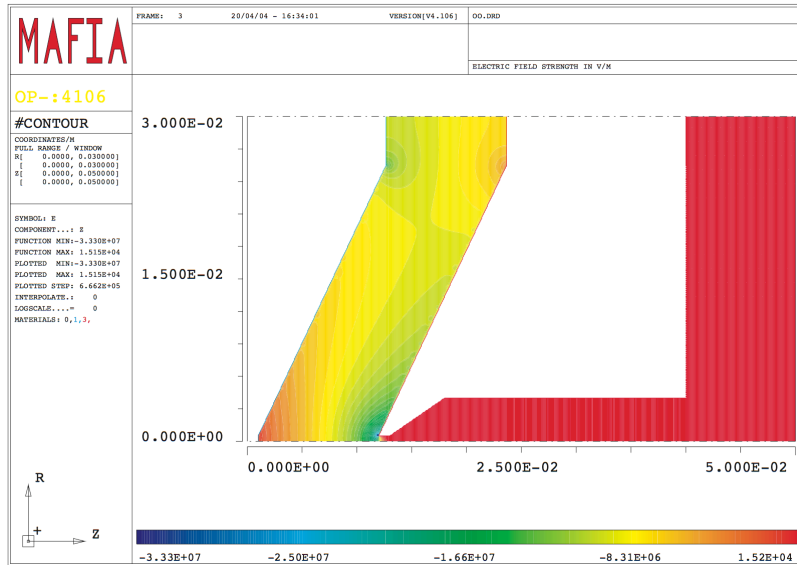


Figure 3.1: The resulting gun design. The plot shows r vs. z in [m] and the longitudinal electric field strength in [V/m] given by the color scale on the bottom. The white structure on the left side is the cathode, the white structure on the right is the anode.

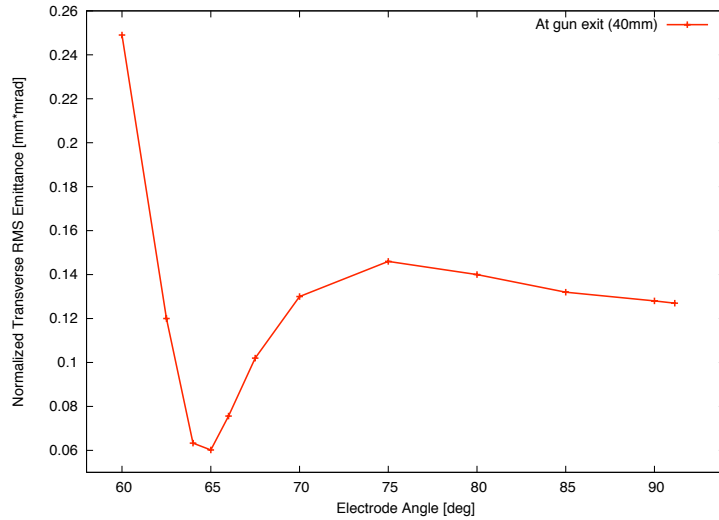


Figure 3.2: Normalized transverse emittance at the exit of the gun as a function of the gun electrode angle. In this design, the minimum emittance is reached at 65°. For smaller angles, over-focusing occurs at the iris.

growth of transverse normalized emittance at the gun exit for iris radii below 0.5 mm is caused by particle loss on the iris.⁴ For larger radii the emittance increases due to an increase of nonlinear electrostatic field components.

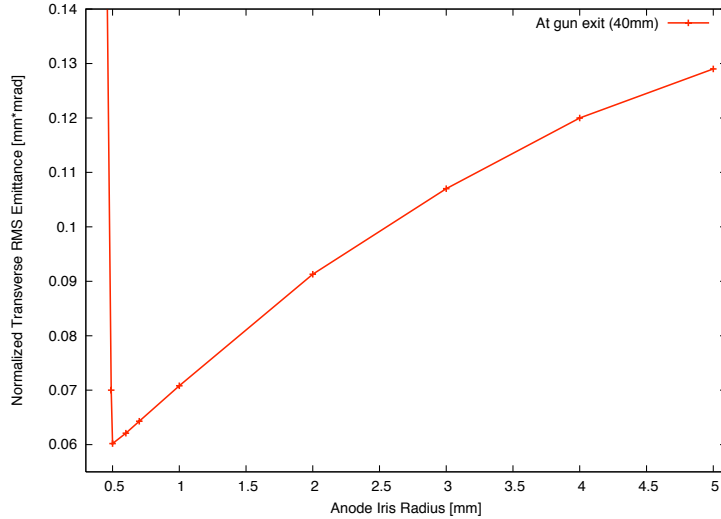


Figure 3.3: Normalized transverse emittance at the exit of the gun as a function of the anode iris radius. In this design the minimum emittance is reached for a radius of 0.5 mm. For radii below 0.5 mm the emittance seems to increase strongly; this is due to particle loss on the anode iris.

The maximum electric field strength occurs on the anode iris as anticipated (see Fig. 3.1). For the chosen anode iris radius, a gap of 11 mm limits the peak surface field to 20 MV/m on the iris while offering 9.1 MV/m average accelerating gradient on axis. Peak electric field strength as a function of the gap size is shown in Fig. 3.4. If vacuum and surface conditions allow, the gap can be further reduced to decrease space charge forces and hence emittance blow-up.

Finally, the design includes an anode channel with 8 mm diameter down-

⁴It is not the loss of particles that causes the growth in emittance per se. The emittance increase is caused by the simulation which puts particles that have collided with material at very far away locations. This leads to a perceived emittance growth.

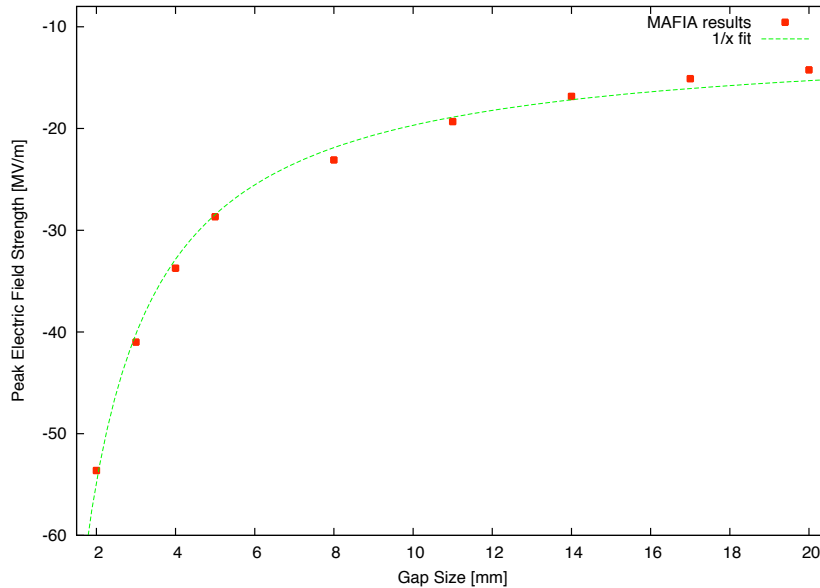


Figure 3.4: Peak longitudinal electric field strength as a function of the accelerating gap size. Due to HV breakdown concerns it was chosen to limit the peak surface field to 20 MV/m which renders a gap of 11 mm.

stream of the iris. This should allow passage of fairly divergent bunches without particle loss. The optical properties of the gun are given by the iris dimensions on the side towards the gap. Therefore the narrow iris can be thin (1 mm) and the channel in the field-free region downstream is enlarged without influencing the gun optics.

3.2 Solenoid Design

The solenoid magnet is intended to focus the beam and perform emittance compensation as detailed in Section 2.5.2. It was decided to use an in-vacuum solenoid magnet in an iron magnet yoke in order to use a smaller magnet and to forgo a bucking coil close to the cathode and on HV potential. The boundary conditions for the solenoid magnet were given by maximum available size (roughly 40 mm radius and 50 mm length). The magnet had

to be enclosed in a magnet iron case (high relative magnetic permeability μ_r) in order to confine the magnetic field. It was required to have a focal length of as little as 12 mm for 100 keV electrons.

The resulting design [47] called for 1000 windings with a maximum solenoid current of 3.6 A running from an inner radius of 6 mm to an outer radius of 32 mm over a length of 20 mm. To form the yoke, 4 mm thick disks are placed before and after the windings and a 1 mm thick cylinder encloses the entire assembly over the total length of 28 mm. The simulated solenoid design is depicted in Fig. 3.5.

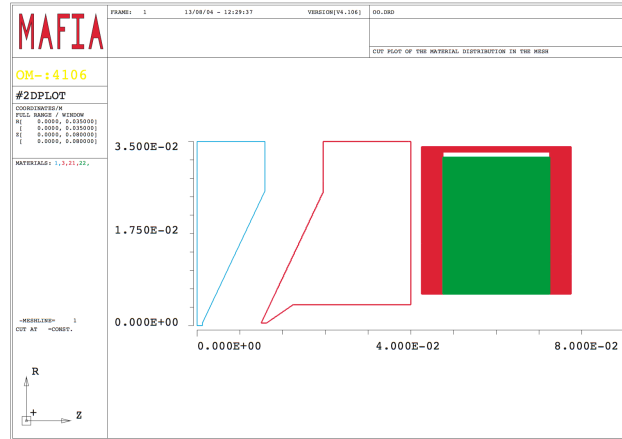


Figure 3.5: The resulting solenoid design next to the cathode (in blue) and anode (in red). The plot shows r vs. z in [m]. The red structure on the right side is the yoke surrounding the windings (in green).

The 3.6 A maximum solenoid current corresponds to 6.83 A/mm² average current density in the windings. This current density and the solenoid geometry was fed to the MAFIA magnetostatic solver. The resulting longitudinal magnetic field is shown in Fig. 3.6. The symmetric field profile is confined well by the yoke preventing field leakage onto the cathode. The peak magnetic field on axis is slightly more than 200 mT which fulfills the specifications.

The RMS beam size for different solenoid settings is shown in Fig. 3.7. The

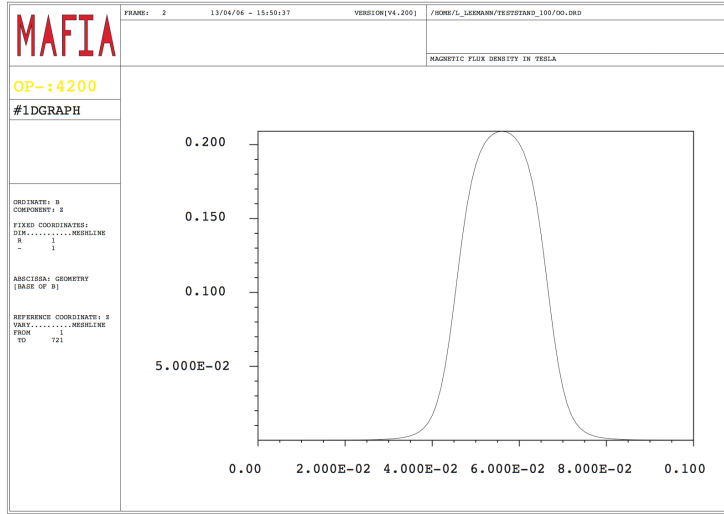


Figure 3.6: Longitudinal magnetic field strength generated on axis by the solenoid magnet. The plot shows B_z in [T] vs. z in [m]. The maximum field strength is at the center of the solenoid magnet ($z = 56$ mm). The yoke confines the field to prevent field leakage onto the cathode (located at $z = 1$ mm).

beam waist created downstream of the solenoid is clearly visible; solenoid current tuning will allow adjustment of this waist location to a designated spot in the diagnostics section following the solenoid magnet. With increasing solenoid current, the beam is focused and the radius at the waist location is reduced. The longitudinal position of this waist approaches the solenoid for increasing solenoid currents. As expected, stronger foci produce more divergent beams.

The normalized transverse emittance for different solenoid settings is shown in Fig. 3.8. The emittance blow-up in the solenoid is due to the fact that MAFIA calculates projected emittance values as mean values of all bunch particles at certain time steps rather than at a certain location. In the vicinity of the solenoid magnet different parts of the bunch are rotated and focused differently by the solenoid. MAFIA's averaging thus shows a blow-up of the projected emittance that extends throughout the entire solenoid and its fringe fields; if one would observe slice emittance evolution for a

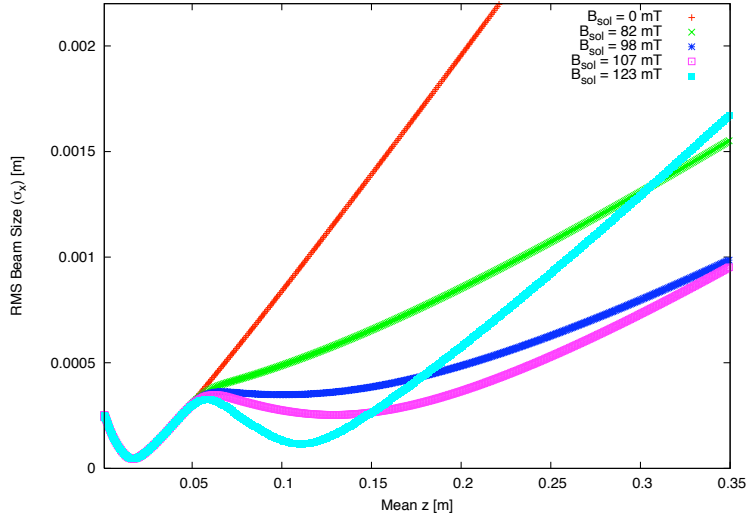


Figure 3.7: RMS beam size plotted as a function of the mean longitudinal position for different solenoid settings. The first data set (red) shows radius evolution without solenoid focusing.

single slice in the solenoid, the blow-up would not occur. Once the bunch has fully passed the solenoid magnet the resulting emittance reaches values comparable to those before the solenoid. With increasing solenoid current the resulting emittance downstream of the solenoid is reduced compared to the entirely uncompensated beam. The minima following the solenoid are a consequence of emittance compensation as detailed in Section 2.5.2.

An example demonstrating how proper solenoid tuning can reduce the emittance as described by the linear emittance compensation scheme is given in Fig. 3.9. The plot shows the normalized transverse emittance at a location downstream of the solenoid magnet; there is a global minimum for $B_{\text{soli}} = 115$ mT.

By varying the solenoid current the longitudinal position of the emittance minimum can be adjusted. However, the absolute value of this minimum changes as well. Within the space available for the diagnostics, a solenoid setting generating an overall emittance minimum has been found as shown in Fig. 3.10. Such a minimum is found for $B_{\text{soli}} = 119$ mT at $z = 182$ mm; in an

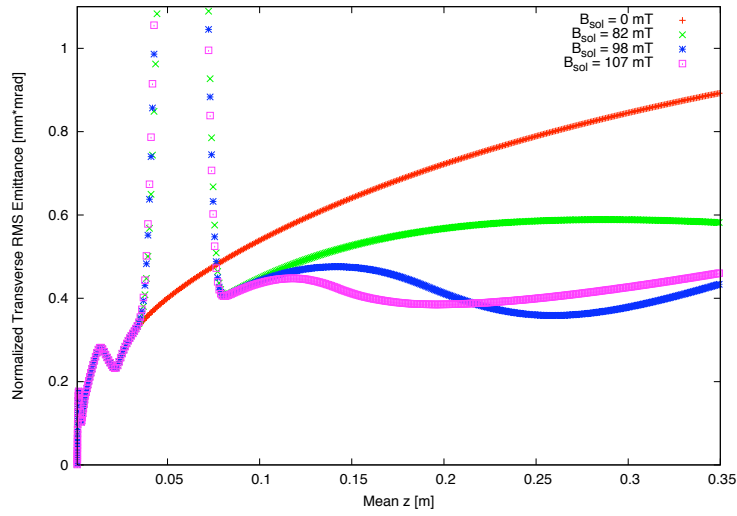


Figure 3.8: Normalized transverse emittance plotted as a function of the mean longitudinal position for different solenoid settings. The first data set (red) shows emittance evolution without solenoid focusing, which clearly shows the blow-up caused by space charge forces. With proper solenoid focusing the downstream emittance can be reduced (emittance compensation).

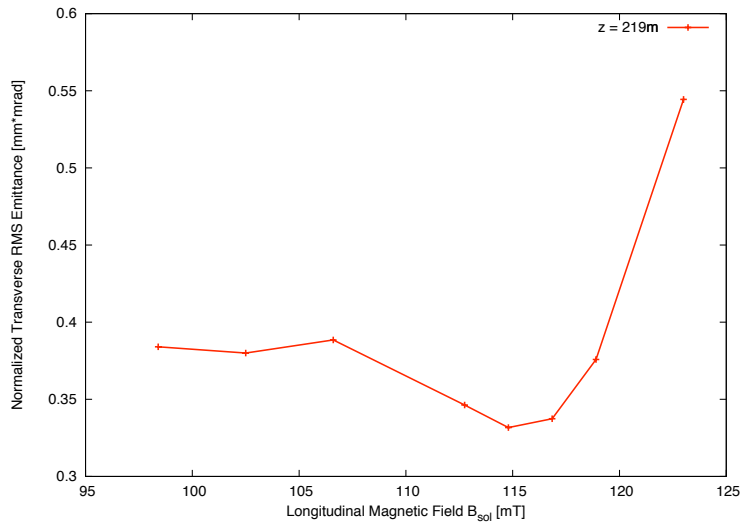


Figure 3.9: Normalized transverse emittance at $z = 219$ mm (diagnostics section) plotted as a function of the longitudinal magnetic field generated by the solenoid. There is a global minimum for $B_{sol} = 115$ mT.

actual pre-injector setup this would be a suitable location for an accelerating section to quickly accelerate the bunch to ultra-relativistic energies in order to preserve the low emittance.

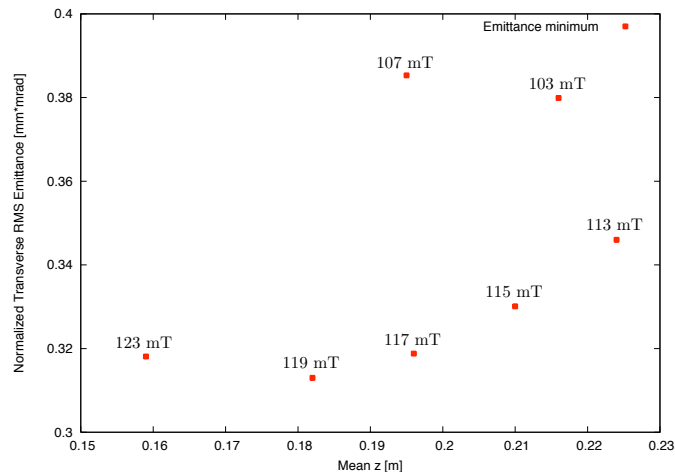


Figure 3.10: Emittance minima and corresponding longitudinal positions plotted for different solenoid strengths. There is an overall minimum for a solenoid setting of $B_{sol} = 119$ mT at $z = 182$ mm.

3.3 Specifications for Diagnostics

Slits, slit arrays, pinhole arrays, and a pepper-pot⁵ will be used to measure the transverse emittance of bunches emitted from FEAs (see Section 4.7.3). The pepper-pot mask can be moved longitudinally through the beam, while the other masks are inserted into the beam at a fixed longitudinal position. However, whereas the pepper-pot is attached to the screen monitor and there is a fixed distance between its hole array and the screen, the distance between the screen monitor and the other inserts is variable and can be used to optimize the resolution and intensity of the image. Simulations

⁵A pepper-pot is basically a pinhole array attached to a screen.

of the emittance measurement for different insert types can be used to verify that design parameters (hole/slit width, pitch, distance to screen) have been properly chosen and to check the precision of the emittance reconstruction.

These emittance measurements require that beam size and divergence can be properly reconstructed. Proper resolution of bunch size implicates that enough slits/holes are hit by the bunch so the beam envelope can be recognized. Proper resolution of the bunch divergence requires that the images of the slits/holes can be distinguished from each other; apart from preventing overlap of the images this requires a sufficient image SNR.

An additional constraint is given by the mask thickness. If the mask thickness is small compared to the hole/slit size the observable phase space distribution is a slice with sharp boundaries in configuration space and full divergence resolution. If the hole/slit size becomes comparable to the thickness of the mask an angular acceptance of the measurement has to be considered. The hole/slit opening angle gives a maximum angular resolution [48]

$$u'_{\max} = \frac{2r}{s}, \quad (3.2)$$

where $2r$ is the hole diameter or slit width and s is the thickness of the mask. The reconstructible bunch fraction in phase space is no longer a slice, but a parallelogram given by the hole/slit size and the maximum angular acceptance. This is depicted in Fig. 3.11.

Due to the low energy of the electrons in the test stand a very thin tungsten mask can be used. The mask thickness of $100 \mu\text{m}$ allows divergences as large as 100 mrad to be resolved with hole/slit width as small as $10 \mu\text{m}$ radius. Optimization of the masks will therefore consider $10 \mu\text{m}$ the lower limit for hole/slit width.

After several parameter studies to optimize the measurement resolution the following pepper-pot mask dimensions were chosen: $50 \mu\text{m}$ diameter holes with a pitch of $320 \mu\text{m}$. This allows sufficient resolution of the focused and unfocused beam at three different reference positions in the diagnostic section

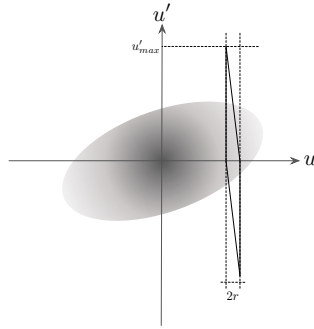


Figure 3.11: An example demonstrating the effect of angular acceptance of a hole/slit mask when reconstructing a trace space distribution. Rather than observing a bunch slice, one observes parallelograms. If the mask is tilted with respect to the beam path, the parallelogram is shifted vertically in trace space.

(right after the solenoid magnet, at the end of the diagnostics section, and an intermediate position). Examples of these simulations are shown in Figs. 3.12 and 3.13.

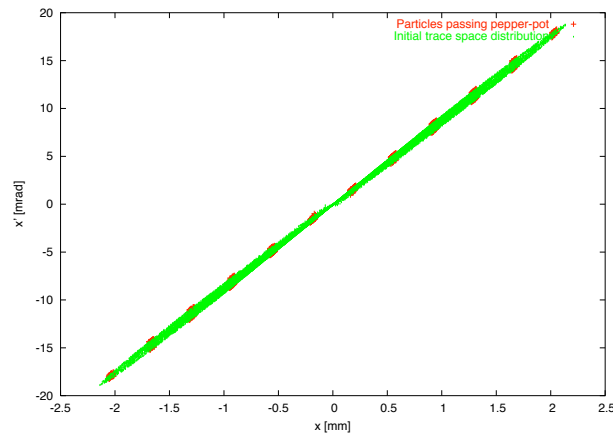


Figure 3.12: A bunch in trace space (green) and the particles in the beamlets behind the pepper-pot mask (red). The pepper-pot has $50 \mu\text{m}$ diameter holes with a pitch of $320 \mu\text{m}$. The bunch plotted here is seen right after the solenoid magnet; it is however unfocused and hence diverging.

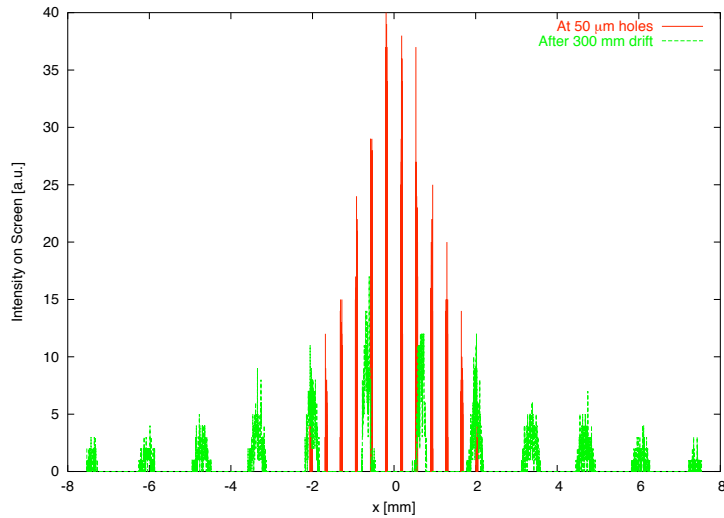


Figure 3.13: The beamlets formed by the pepper-pot shown in Fig. 3.12 now seen on the screen monitor: right after the pepper-pot (red) and after a 300 mm drift. From the shift of the distribution centroids, the divergence centroid of each beamlet of the bunch can be calculated. The widening of the beamlets gives the divergence spread within a bunch slice.

All other masks are inserted at the location of smallest beam size and lowest emittance (for a properly tuned solenoid). The holes/slits are therefore chosen smaller ($20 \mu\text{m}$ diameter) and arranged closer ($170 \mu\text{m}$ pitch). A simulation example for a slit array measurement is given in Figs. 3.14 and 3.15. In the example a distance of 150 mm is chosen between slit array and screen monitor. It is desirable to maximize beamlet image size, but at the same time the beamlet images have to remain distinguishable.

A simulation for trace space reconstruction with slit arrays is given in Fig. 3.16. A Gaussian bunch with 50,000 macro-particles and an assumed emittance of 0.08 mm mrad has been generated. The macro-particles are tracked through the slits and a subsequent 150 mm long drift. The screen monitor ($2 \mu\text{m}$ resolution assumed) image is then used to reconstruct the trace space distribution and calculate the emittance. The emittance calculated from the reconstruction differs from the emittance derived from the entire bunch data by only 11%.

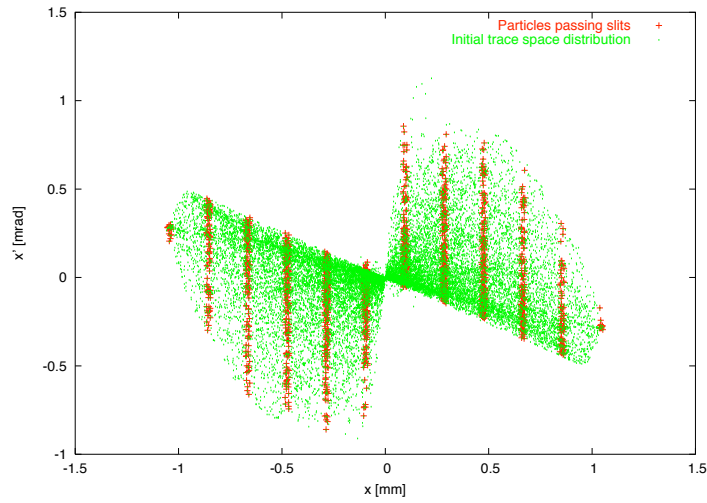


Figure 3.14: A bunch in trace space (green) and the particles in the beamlets behind the slit array mask (red). The slit array has $20\ \mu\text{m}$ wide slits with a pitch of $170\ \mu\text{m}$. The bunch plotted here is focused at the location of the slit insert.

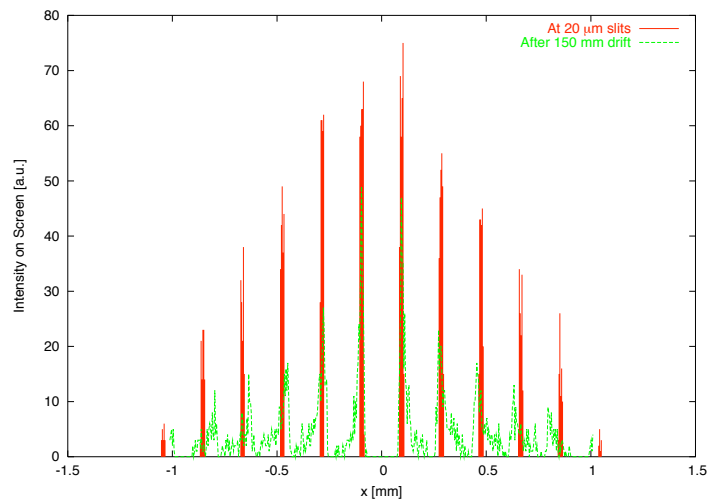


Figure 3.15: The beamlets formed by the slit array shown in Fig. 3.14 now seen on the screen monitor: right after the slit array (red) and after a 150 mm drift. From the shift of the distribution centroids, the divergence centroid of each beamlet of the bunch can be calculated. The widening of the beamlets gives the divergence spread within a bunch slice.

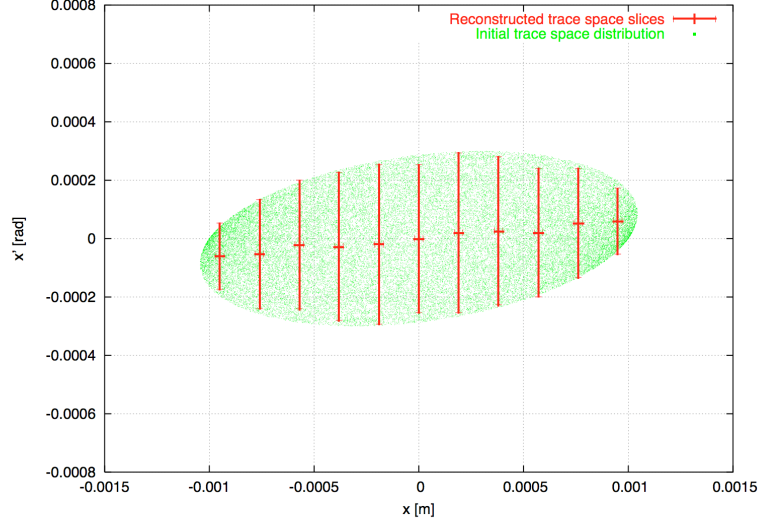


Figure 3.16: A bunch in trace space (green) and the trace space slices reconstructed from a simulated slit array measurement (red). The slit array has $20\ \mu\text{m}$ wide slits with a pitch of $170\ \mu\text{m}$. The drift between slit array and screen monitor is $150\ \text{mm}$.

3.4 Slice Emittance from MAFIA Data

MAFIA calculates projected emittances of the bunch at specified times; the bunch centroid given together with the emittance data is however an average over all longitudinal positions of particles in the bunch at that time. The emittance of the bunch at a certain location is therefore not at all identical with the emittance value calculated by MAFIA. This is somewhat unfortunate since in the actual experiment projected emittance is always derived at a certain location and not at a certain time.

For slice emittance values this problem does not exist. A MAFIA data dump for a given time can be used with the approximation given in Section 2.2.4 to calculate slice emittance values for all positions in the bunch and (almost) arbitrary slice lengths. The lower limit for the slice length is given merely

by statistics: In order to get decent slice emittance values several hundred macro-particles are required per slice. If the slices are chosen very thin, the total number of particles to track can require very large CPU time.

An example for such a simulation is given in Fig. 3.17. A bunch is observed at a time where the head is just about to leave the experimental chamber. The projected emittance of this bunch is 0.24 mm mrad. The slice width is 2.5 ps corresponding to 0.5 mm; the weighting function is calculated according to Eq. (2.38) and averages according to Eq. (2.40). The slice emittance values are then plotted. As expected, near the edges of the bunch (strong charge modulation) the slice emittances are much larger than at the center of the bunch (roughly constant charge distribution). The largest slice emittance values are roughly 40% less than the projected emittance values. The minimum slice emittance value at the center of the bunch is only 25% of the projected emittance.

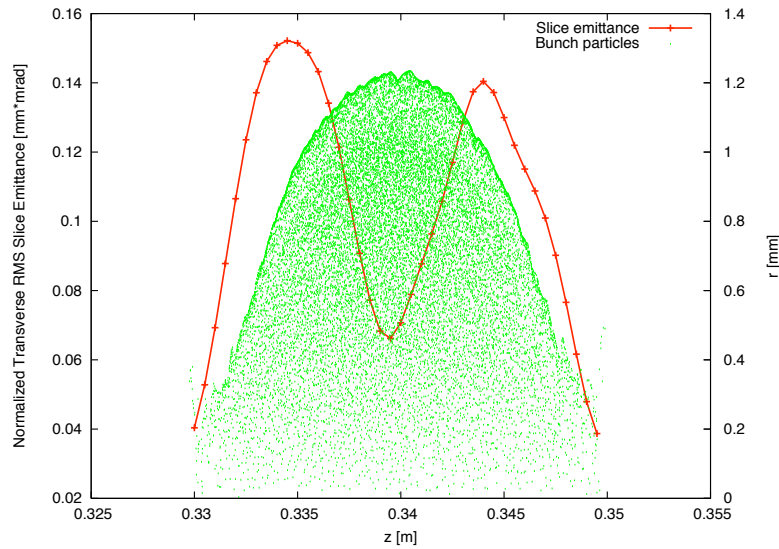


Figure 3.17: A plot showing r vs. z for the macro-particles in a bunch from a MAFIA data dump (green). The slice emittances are calculated as described in Section 2.2.4 and shown here in red. The projected emittance of this bunch is 0.24 mm mrad.

3.5 Tolerances

Final simulation efforts were directed towards specifying tolerances for the gun assembly. Due to the 100 kV DC HV a 20 cm long ceramic break has to be installed between the cathode and anode flanges. The entire cathode assembly is inserted into the vacuum chamber and reaches across the ceramic break; it has a total length of almost 400 mm. Therefore if the anode-ceramic or ceramic-cathode flanges are assembled with any residual tilt or if the FEA is not properly fastened to the cathode mount, the FEA will be displaced from the beam axis and/or be tilted with respect to the anode and solenoid magnet. Simulations were performed to investigate how sensitive the beam emittance is to such a misalignment.

For these simulations, the previously used MAFIA 2.5D code is inadequate since a displacement or tilt of the FEA with respect to the beam axis breaks the required cylindrical symmetry. It was therefore decided to use the code GPT [49]. The code allows particle tracking through predefined elements or electromagnetic fields generated by field solver codes. Field maps can be imported and rotated or scaled with respect to other optical elements defined in GPT. MAFIA's electrostatic and magnetostatic solvers were used to generate high resolution field maps of the accelerating electrostatic field and the solenoid magnetostatic field. The maps were imported into GPT where the diagnostic section of the test stand was modeled. Particles were tracked through rotated or displaced fields and the resulting emittances were compared to a setup free of misalignment.

The two misalignments are referred to as "tilt" (FEA rotated around the vertical axis) and "shift" (FEA displaced transversely from the beam path in the horizontal plane). Examples are given in Figs. 3.18 and 3.19 where the emittance at the center of the diagnostics sections is plotted as a function of the FEA misalignment.

For the tilt, the emittance shows a monotone increase with tilt angle; for 160 mrad the emittance has doubled. The shift misalignment shows very little

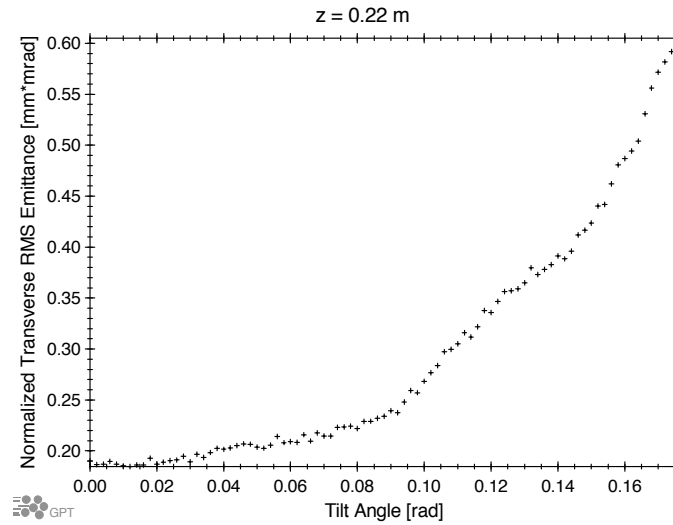


Figure 3.18: Emittance at the center of the diagnostics section as a function of cathode tilt with respect to the design beam axis. For 160 mrad tilt the emittance doubles. Tilts below 25 mrad increase emittance by less than 5%.

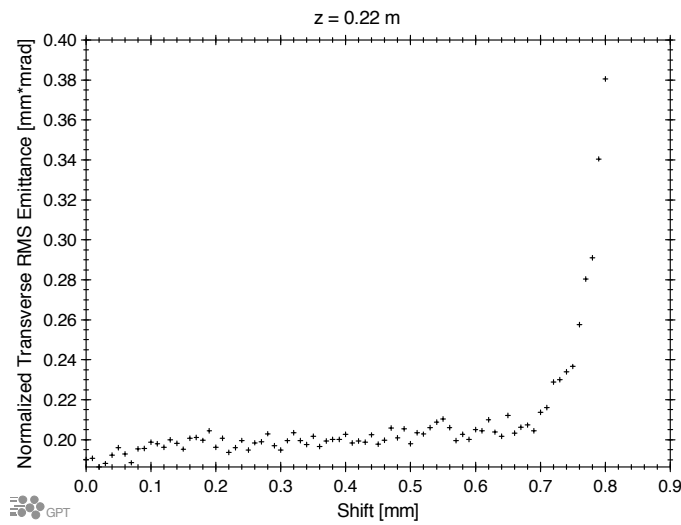


Figure 3.19: Emittance at the center of the diagnostics section as a function of horizontal cathode displacement with respect to the design beam axis. For shifts below 0.5 mm the dependence is very weak. A strong emittance increase is observed for shifts larger than 0.7 mm.

influence on the emittance up to a threshold of roughly 0.7 mm where the emittance increases dramatically due to particle loss. For a shift of 0.9 mm the emittance increases by a factor 5.

For the assembly of the test stand it is assumed that misalignments should not lead to more than 5% increase of emittance at the location of the diagnostics. According to these simulations, this is the case if misalignments are restricted to less than 0.6 mm shift and 25 mrad tilt.

These are fairly stringent requirements on the mechanical design. It was therefore decided to initiate the design of a 3D mover motor system to be installed between the anode structure and ceramic break. This system will allow transverse cathode position correction within ± 2 mm with a precision of $10 \mu\text{m}$. Perhaps more importantly it will also allow longitudinal shifts, thus changing the accelerating gap length and therefore the accelerating gradient. Longitudinally a 40 mm travel from the minimum gap distance of 2 mm will be made possible with a precision of $20 \mu\text{m}$.

Chapter 4

Test Stand Setup & Implementation

This chapter presents the experimental setup, gives technical specifications of all components and introduces the methods used for transverse bunch diagnostics. It also includes photos and schematics of several parts of the setup. Technical design drawings of the most important components of the test stand can be found in the appendix.

4.1 Overview

In order to compare different anode/cathode designs and emittance minimization schemes the test stand is required to have a modular design. In the final design the test stand consists of a permanent part with the HV power supply, hotdeck (containing the gate pulser), ceramic structure isolating the HV components from the grounded parts, 3D mover motors, ion pump, control system, and a “flexible” part containing the removable gun electrodes, solenoid magnet, drift section and diagnostics cube holding various diagnostic devices. A schematic of the test stand is given in Fig. 4.1. Figure 4.2 shows a 3D rendering of the test stand.

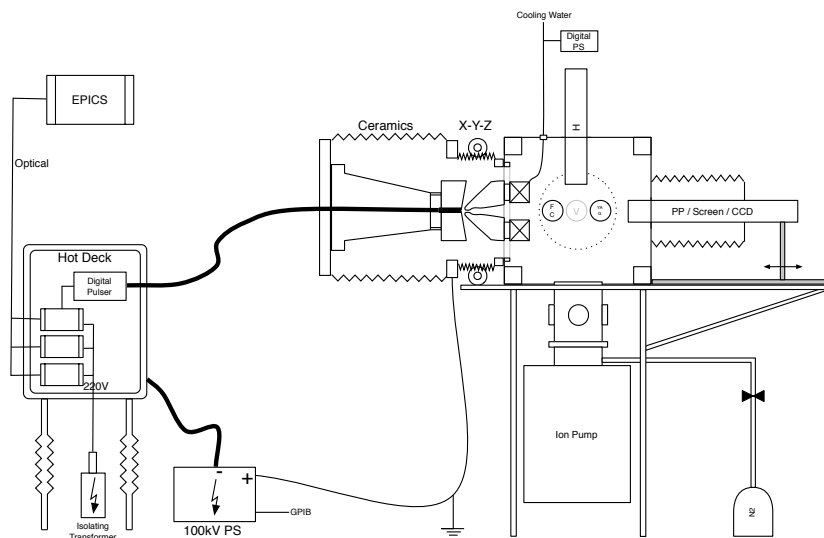


Figure 4.1: Schematic of the test stand.

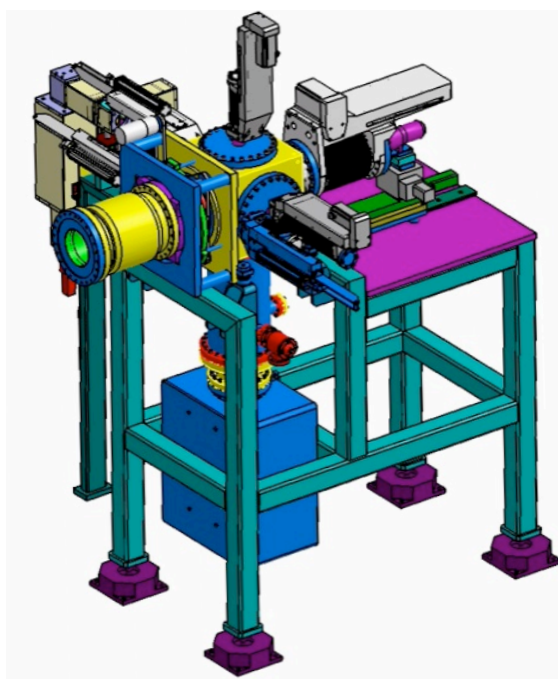


Figure 4.2: 3D rendering of the test stand.

4.2 General Infrastructure

The test stand has been installed in the SLS experimental hall. For radiation (and HV!) protection a 6 m x 4 m bunker with 50 cm thick concrete walls and roof has been assembled from PSI standard radiation shielding blocks. A chicane was built behind the bunker entrance. A lockable grid door is connected to an LAC (local access control) system that interrupts the HV power supply if the door is not locked or an emergency abort switch is activated. A dedicated cable channel was installed for signal, network and power cables as well as pressurized air (coming from PSI's central 7 bar pressurized air system). 230 V / 20 A power is available inside the bunker together with a common ground. A TCP/IP surveillance camera was installed in the bunker. Final operational permission as an "Analytical X-Ray Source for Scientific Purposes" was granted by the Swiss Federal Health Authorities on June 6, 2006 [50].

4.3 Beam Path

4.3.1 Gun Assembly

The gun is basically a diode structure where the cathode electrode is on negative HV potential with respect to the grounded anode. Figure 4.3 shows an inside view of the gun electrodes and solenoid structure.

As mentioned in Section 3.5, a 3D mover motor system has been designed to correct misalignment and vary the accelerating gap. It has recently been manufactured and calibrated in-house and will be installed in the near future. It will be placed between the ceramic break and the anode structure (see Fig. 4.1) where it will move the ceramic structure holding the entire cathode assembly in all three spatial degrees of freedom.

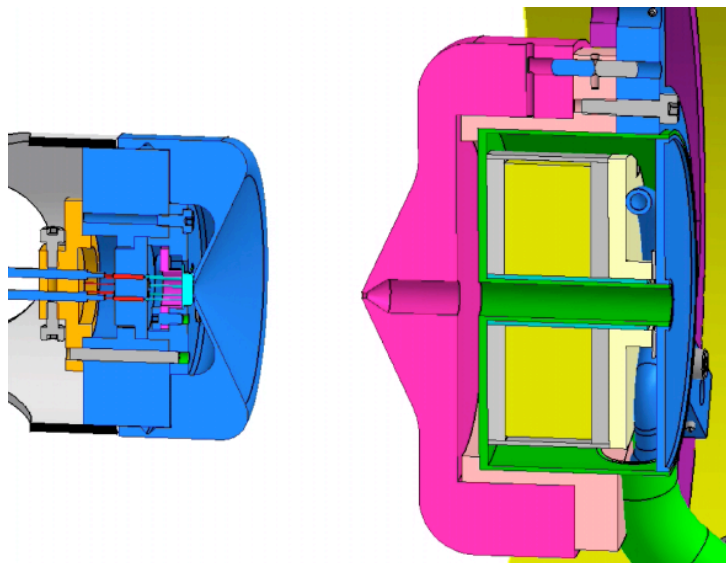


Figure 4.3: 3D rendering of the test stand diode and solenoid: cathode electrode (left, blue) with TO-5 mount (holding the FEA) installed, anode electrode with iris and recessed beam channel (pink). Enclosed in the u-shaped yoke (gray) behind the anode are the solenoid windings (yellow).

4.3.2 FEA and Mounting

The FEAs installed at the test stand are Spindt-type molybdenum FEAs from SRI as mentioned in Section 2.6.3. The silicon substrate of the FEA is attached to a TO-5 mount as shown in Fig. 4.4. There are eight leads at the bottom of the TO-5 header: one is for contact to the tips (attached directly to the TO-5 header), four are connected to the gate contact layer above the TO-5 header (glass insulation within the TO-5 header), and the remaining three are unused.

The FEAs are delivered in evacuated copper capsules that have to be opened with a sharp tube cutter. A protective lid is then removed from the TO-5 header. Ideally this is done in a clean room to prevent any contamination of the delicate FEA surface. At the test stand a laminar flow box is used instead and the FEA is always installed at the last possible moment to minimize exposure to ambient air.

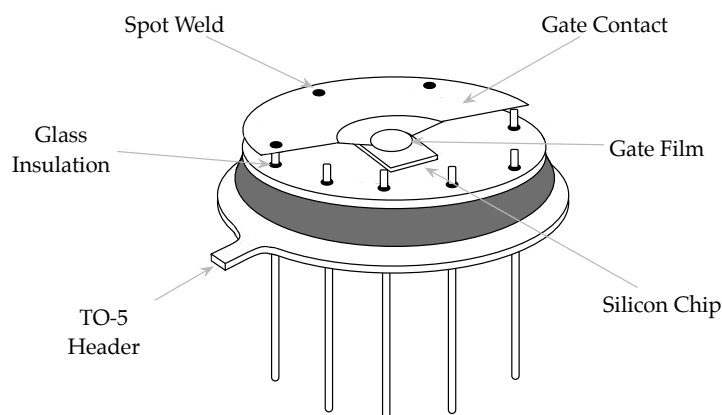


Figure 4.4: Schematic of a Spindt-type FEA on a TO-5 mount from SRI. The active emitting area at the center has a diameter of 1 mm. Image according to [42].

The three unused leads are clipped and the remaining five leads are inserted into a transistor holder at the end of the cathode cone. The transistor holder connects the leads of the TO-5 mount to a coaxial signal cable attached to the cathode vacuum feedthrough. In order to ensure that the FEA is properly positioned a Macor[®] holder piece is screwed onto the cathode cone tip thus clamping the TO-5 to its proper position. The Macor[®] piece centers the TO-5 mount, prevents the FEA from being tilted with respect to the design beam axis and ensures that the FEA is at the design longitudinal position.

4.3.3 Diode Structure: Cathode and Anode

The cathode and anode electrodes were both originally specified to be made from OFHC copper (oxygen-free, high conductivity copper), polished to an average surface roughness of $0.1 \mu\text{m}$. Inadvertently they were electroplated with $3 \mu\text{m}$ gold to prevent oxidation after polishing. This gold layer caused considerable problems in the commissioning phase (see Section 5.3.5). It was therefore decided to manufacture a new set of electrodes from pure 316L stainless steel with an average surface roughness of $0.2 \mu\text{m}$.

The cathode and anode electrodes have been manufactured according to the design presented in Section 3.1.2; a photo of the gold plated cathode electrode is shown in Fig. 4.5.

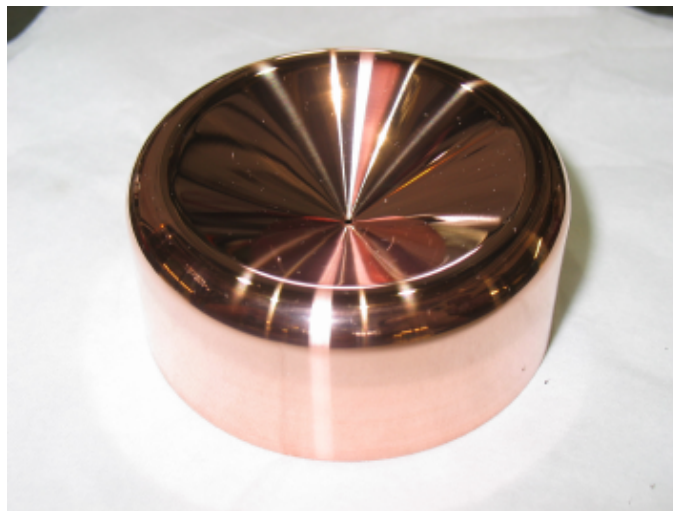


Figure 4.5: Gold plated cathode electrode. The active emitting area of the FEA is placed right below the 1.5 mm hole in the cathode electrode center.

The cathode electrode is fastened to the the end of the cathode cone in such a way that its iris is located directly above the FEA. Three positioning screws inside the cathode electrode allow exact longitudinal positioning. The cathode cone holds the FEA and electrode in place as well as the coaxial connection from the FEA to to the vacuum feedthrough on the cathode flange. The FEA gate layer, cathode electrode, the entire cathode side assembly and the shield of the FEA connection line are on the same potential. In the experiment this is the HV DC bias (-100 kV). The signal lead of the coaxial FEA connection is connected to the tip lead of the TO-5 mount. In the experiment it is pulsed with a negative voltage on top of the HV DC bias. The vacuum feedthrough connecting the coaxial FEA connection to the pulser consists of an SMA plug on a CF100 flange attached to the CF200 flange which closes the cathode side end of the vacuum chamber (see Fig. 4.8).

The anode electrode is fastened to a three-prong cross installed at the entrance of the diagnostics cube. Besides the anode, this cross also holds the solenoid magnet casing. Between the anode electrode and the cross a Macor[®] piece is installed to electrically insulate the anode. A signal line runs from the isolated anode electrode to the vacuum feedthrough (BNC connection) in the main pumping pipe below. The connection to the isolated anode can be used to apply a DC bias to the anode or to measure deposited charge on the anode (in case of beam scraping). The connection should never be left unterminated to prevent charge accumulation on the floating anode electrode. At the anode center the 1.5 mm iris allows the bunch to exit the accelerating gap. The bunch passes a recessed beam channel in the anode immediately before reaching the solenoid channel. Two photos of the cathode are shown in Fig. 4.6. The back view shows the cylindrical space reserved for the electrical isolation and solenoid magnet casing.



Figure 4.6: The gold plated anode electrode as seen from front (left) and back (right). The back side shows the insert for electrical isolation and solenoid magnet casing. The hole at the center is the anode beam channel downstream of the iris.

4.3.4 Solenoid Magnet

Immediately behind the anode the solenoid magnet casing is installed. It is a cylindrical piece manufactured from 1 mm thick 316L stainless steel. The center of the casing is the beam pipe; the casing slides into the cylindrical anode isolation and is fastened to the holder cross (see Fig. 4.7 and the left side photo in Fig. 5.25).

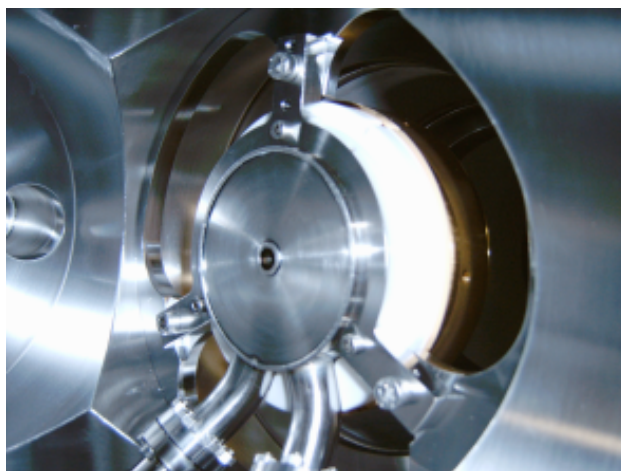


Figure 4.7: Photo of the solenoid magnet assembly installed in the diagnostics cube. The holder cross fastens the solenoid and anode assembly to the diagnostics cube. The hole at the center is the beam channel through the solenoid, the white structure surrounding the solenoid casing is the anode insulator, the anode is the gold plated structure seen at the back. The two pipes for cooling water, solenoid current and solenoid winding temperature signal are attached to the bottom of the solenoid casing. The access port for the Faraday cup (see Section 4.7.1) is seen on the far left.

The casing holds the magnet yoke with the magnet coil windings, a copper heat sink (attached to the yoke) and the cooling water pipes (attached to the heat sink). There are 1000 copper windings over a length of 20 mm from an inner radius of 6 mm to an outer radius of 32 mm as specified in Section 3.2. The windings are made with 0.63 mm copper wire isolated by a film of PVC and daubed in thermally conductive paste to improve transport of heat generated in the windings to the yoke.

The yoke is made from two 4 mm thick disks and a 1 mm thick cylinder slipped around the disks. The parts are manufactured from Armco magnet iron.

The cooling water runs in Teflon[®] tubes inserted into two stainless steel bellows that run from the solenoid casing to CF flanges in the main pumping pipe bellow the diagnostics cube. From there the Teflon[®] pipes are connected to the cooling water pump in the chiller. The chiller manufactured by TermoTek [51] can dissipate 1100 W at 10° C temperature difference from water to ambient air. The cooling water volume is roughly 3 liters. The pumping speed is 3 l/min at 3 bar.

The stainless steel bellows also hold the electrical connections to and from the solenoid windings as well as a signal lead to a thermocouple installed at the center of the solenoid windings. The solenoid windings are connected to an in-house manufactured digital power supply capable of delivering up to 10 A at 24 V (originally designed for the SLS corrector magnets [52]). The power supply is connected to the digital control system (see Section 4.6.1). The K-type thermocouple is connected to an ADC that is read out by the digital control system as well. At the maximum specified current of 3.6 A, ≈ 86 W of dissipated heat are expected; the chiller should be capable of dissipating this heat without any problems.

Calibration measurements of the solenoid magnet will be presented in Section 5.1.

4.3.5 Drift Section

Following the solenoid the beam enters a drift space of up to 444 mm. This drift is the *diagnostics section* of the test stand. The first part of the drift is within the “diagnostics cube” which is a 300 mm stainless steel cube with access ports on all sides. The rest of the drift is within a stainless steel beam pipe attached to the far end of the diagnostics cube. The phosphor screen

(see Section 4.7.2) which can be moved longitudinally through the cube and the beam pipe is the final beam stop.

4.4 High Voltage & FEA Pulsing

A DC HV bias has to be applied to the entire cathode assembly. Furthermore the FEA has to be pulsed on top of this bias voltage. Therefore the HV is not applied directly to the cathode but to a HV cabinet that holds the pulser; this cabinet is the so-called *hotdeck*. From the pulser a connection is then made to the cathode where the shield of the coaxial FEA connection allows the entire cathode assembly to be put on hotdeck potential and the signal lead of the connection delivers the emission pulse on top of the bias voltage to the FEA tips.

4.4.1 High Voltage Power Supply

The high voltage power supply from FUG [53] delivers up to 1 mA at 100 kV DC HV. It offers voltage regulation with a current limitation and steps down voltage as soon as this limitation is reached. It is installed in the 19" controls racks outside the bunker with a 20 m HV cable connecting the power supply output to the hotdeck. An IEEE 488 interface is available, but the HV power supply is controlled manually using the two knobs for set voltage and current limit as well as the display showing applied voltage with 0.1 kV and current flow with 1 μ A accuracy.

It was observed that the power supply was not capable of sustaining a stable voltage below 3 kV. Since only few tests are performed at such low DC voltage levels this was of no big concern.

When the power supply is switched off it discharges an unloaded output within 10 s according to specifications. As a safeguard the LAC has therefore

been designed in such a way that there is a 12 s delay between the power cut to the power supply and the door lock release.

4.4.2 Hotdeck

The hotdeck is essentially a 19" rack on electrically isolating stilts with an isolating transformer supplying 230 V AC power to the components in the rack regardless of their DC potential. The hotdeck manufactured by PPT [54] is specified for 100 kV. Its rack is connected to the HV power supply. The hotdeck is installed in a corner of the bunker at 30 cm distance from the bunker walls. In addition the concrete bunker walls in that corner have been covered with 2 mm sheet metal which is grounded. For safety reasons a 1 m long grounding stick is attached to the hotdeck at all times except when the bunker is locked with the LAC. Even in the event of a complete connection failure to the power supply, this stick allows safe discharging of the hotdeck. Photos of the hotdeck are shown in Fig. 4.8.



Figure 4.8: The hotdeck consisting of a 19" rack that holds the gate pulser and electronics for communication (in the rack) as well as the 230 V isolating transformer (between the rack and the base). The cathode flange with the SMA vacuum feedthrough, ceramic insulation and diagnostics cube are shown in the right picture.

4.4.3 Pulser

The pulser delivers short pulses to the tips of the FEA to trigger emission. The device manufactured by Avtech [55] deliver pulses from 0 to -320 V with pulse lengths between 5 ns and 100 ns. It can pulse at fixed internal frequencies up to 5 kHz or in triggered mode where an external trigger signal is applied. The pulser is installed in the hotdeck rack and draws power from the isolation transformer. It is connected to the cathode through the SMA vacuum feedthrough in the cathode flange. Since the output requires 50Ω termination, a terminator was added in parallel to the connection between the pulser and the FEA.

The pulser is controlled through an RS-232 interface. For external triggering a TTL input signal is expected. In addition to the actual output pulse it delivers a “sync out” TTL pulse which is synchronized to the main output. This signal can be used to trigger diagnostic devices.

It was verified with a 2 GHz - 20 GS/s oscilloscope that the pulser delivered the specified pulses at the output. For maximum pulse voltage the pulse rise time was below 2 ns and the fall time was below 4 ns; the pulse had a flat top. For pulse voltages between -100 V and 0 V the pulse shape deteriorates quickly as specified by the manufacturer: rise and fall times become large and the pulse does not show a flat top.

4.5 Vacuum System

UHV conditions are required to prevent contamination of the FEA and HV arcing. A set of vacuum pumps and vacuum diagnostics allow UHV conditions to be established and monitored; details are given in this section.

The entire test stand has stainless steel vacuum chambers connected through knife-edge flanges (Conflat) sealed with silver-plated copper gaskets. All components are either removable or specified to withstand baking at 150° C

for prolonged periods of time. For baking a heating tent with heat coils and fans is lifted over the test stand and closed with insulating blankets. In this way homogeneous heating of all components is achieved. Venting is performed with dry nitrogen.

Pumps, venting inlet and vacuum diagnostics are connected to the test stand through the “main pumping pipe” which is a 200 mm diameter pipe from the bottom port of the diagnostics cube to the ion getter pump installed under the cube. The pipe has five DN 40 access ports of which two are reserved for solenoid cooling water inlet/outlet and one holds the BNC vacuum feedthrough for the anode signal lead.

4.5.1 Vacuum Pumps

The main pump is a Varian diode 500 l/s ion getter pump [56] installed below the diagnostics cube and attached by the main pumping pipe. It is controlled through a dedicated power supply in the 19” controls rack outside the bunker. The power supply also displays applied voltage, current and pressure (derived from the current) values. The pump can be controlled through a digital interface, but at the test stand it is controlled manually via the front panel since only little interaction is required. The maximum voltage is 7 kV; as pressure drops it can automatically step down to 3 kV. The pressure range covered is from roughly 10^{-7} mbar to 10^{-10} mbar. If pressure increases and current values reach a predefined limitation a protection mechanism switches the pump off. The pump has a dedicated heating element capable of heating the pump up to 350° C during bakeout.

In order to cover the pressure range between ambient pressure and 10^{-7} mbar an additional pump stand is attached to the main pumping pipe through one of the two free DN 40 ports. It consists of a pre-pump and a turbo-molecular pump in series that can reach pressure levels as low as 10^{-8} mbar. The turbo-pump is controlled automatically according to the pre-pump speed. The pump stand also has a venting inlet port to attach the dry nitrogen supply

or a leak testing device. Once the pump stand has achieved approximately 10^{-7} mbar the ion getter pump is switched on. Within a short time pressure levels inside the main pumping pipe and the diagnostics cube are lower than those reached in front of the pump stand. At this point the connection between the pump stand and the main pumping pipe is closed with a corner valve to ensure further pressure reduction in the beam pipe.

4.5.2 Vacuum Diagnostics

Pressure Gauges

Two pressure gauges are installed at the test stand. One is attached to the last free DN 40 port on the main pumping pipe just below the diagnostics cube; it gives pressure readings close to the actual pressure in the beam pipe. The other is installed in front of the pump stand and can be used to monitor the initial pump down progress before the pump stand is valved off.

Both gauges are cold cathode gauges from Pfeiffer [57]. The measurement range extends from 10^{-2} mbar to $5 \cdot 10^{-11}$ mbar. The gauges are read out through the control system: the analog output is connected to an ADC of the digital control system which converts the voltage to a pressure reading.

Rest Gas Analyzer

An RGA (rest gas analyzer) “Prisma QMS” from Pfeiffer [57] is used to monitor the rest gas composition in the test stand. It is attached to the diagnostics cube top port so that it is close to the actual beam path. A heated filament ionizes rest gas molecules that then pass a quadrupole mass spectrometer giving molecule partial pressures in m/e units. The RGA is controlled through an in-house software solution running on a dedicated PC. The output is either a spectrum of rest gas molecule partial pressures at a given time or the time evolution of certain molecule partial pressures.

The RGA has proven to be a more sensitive tool to monitor overall pressure than the vacuum gauges; this is possibly due to the fact that it is installed very close to the diode gap. It also allows proper assessment of the contamination of the vacuum chamber after a vent, after installing new parts or after a HV arc. Specifically water (coming from venting under humid conditions and which can be removed through a bakeout) can be well distinguished from grease (from insufficient cleaning of new parts). Also hydrogen (outgassed by metals and the largest contributor to the base pressure) can be well distinguished from nitrogen (after venting and before completely pumping down) or ambient air (specific ratio between nitrogen, oxygen, and argon) indicating a leak. In the commissioning phase the RGA was also successfully used to distinguish HV arcs happening across the ceramic insulator on the outside from breakdown occurring in the diode area inside the beam pipe.

An example for RGA measurements is shown in Fig. 4.9 where RGA spectra before and after a pumpdown are shown. The main contributions to rest gas after the pumpdown are H^+ and H_2^+ that outgas from metals. The next major contributions are N_2^+ , H_2O^+ , and CO_2^+ from ambient air. A bakeout was performed to further reduce the base pressure. The result is shown in the third spectrum of Fig. 4.9.

Leak Testing

Finally, a leak test is performed to make sure the vacuum chamber is tightly sealed after venting and that thermal stress during a beakout has not led to breaches in the chamber. For this purpose small amounts of helium are sprayed around flanges, valves and bellows. A helium detector from Pfeiffer [57] is attached to an auxiliary outlet of the pump stand and monitors if the turbo-pump removes any helium from the vacuum chamber. This is a quick and simple way to detect leaks in the vacuum chamber and is performed after every vent and bakeout.

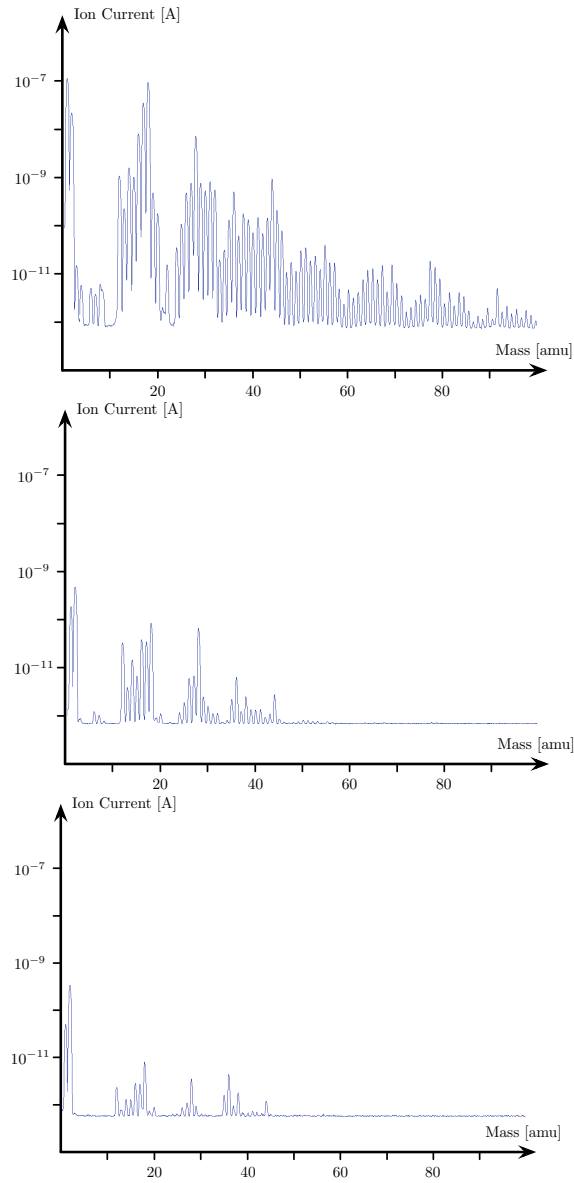


Figure 4.9: Examples of rest gas analyzer spectra. The first spectrum is after venting. The base pressure is 10^{-6} mbar. The second spectrum was taken after the pumpdown at a pressure of roughly 10^{-8} mbar. Next to hydrogen, the main contributions come from nitrogen, oxygen and water (ambient air). The third spectrum is after a bakeout. The pressure level is now $8 \cdot 10^{-10}$ mbar. Although hydrogen is still present, contributions from ambient air as well as water have been reduced by an order of magnitude.

4.6 Control System

At the test stand a control system was required to monitor all measurement parameters, acquire data, and control motors, pumps, and diagnostics equipment. Ideally the control system would allow local and remote control as well as real-time data acquisition and archival.



Figure 4.10: The test stand control system. Two 19" racks hold the controls hardware. The two VME crates can be seen in the bottom halves of the racks. The right rack is reserved for diagnostic controls hardware, the left rack holds network hardware, power supplies and vacuum controls.

4.6.1 Control System Hardware and Software

EPICS

It was decided to use EPICS [58] as a control system. Not only did it deliver the requested functionality, but since it was in use at the SLS a wide range of software and hardware as well as expertise was already available in-house. In

principle EPICS is a TCP/IP based networking protocol (“Channel Access”), an extensive set of I/O device drivers and a database that allows values to be read, set or calculated either directly through simple commands issued by the user on a remote terminal or automatically as predefined.

VME crates and the IOC

The interface between the experiment hardware and the control system is the IOC (Input/Output Controller) in the VME crates. The VME crates offer power and cooling to VME cards (such as the IOC) which perform various tasks. The IOC implements the Channel Access Server and the EPICS database; it processes or scans database records. The IOCs use PowerPC® processors running the real-time OS VxWorks. Communication with the IOC is either performed over a direct serial interface (IOC console) or through Channel Access from a network PC. The IOC configuration includes device drivers for other VME cards and database record descriptions (input, output or data manipulation).

VME Cards

At the test stand two VME crates and IOCs are in use: one for genuine controls (for example timing) and one for diagnostic related controls (for example CCD image readout). Apart from the IOCs the crates hold various other VME cards: ADCs (for example for the solenoid temperature readout), digital I/O (for example to control zoom optics and mirrors), event receiver card (for timing), motor driver card (to control the motor power supply box), SSI card (linear encoders for motor position read-back), digital power supply controller card (to control the solenoid magnet power supply) and frame grabber card (to read out and display CCD data).

Micro IOC

In addition to the interfaces offered by these VME cards, RS-232 serial communication interfaces are required. These interfaces are provided by the so-called Micro IOC which is basically a rack-mounted PC with several RS-232 ports running Linux, an EPICS server and Channel Access. The Micro IOC can send and receive RS-232 commands and data through Channel Access. At the test stand this is used to control the pulser in the hotdeck.

4.6.2 Fiber Optic Communication

At the test stand it is necessary to send commands and trigger signals to the pulser and receive data readout and sync out signals from the pulser. Since the pulser is in the hotdeck and on HV potential during the experiments while the control system is always grounded, a communication method had to be chosen that does not rely on electrically conducting materials. It was therefore decided to use fiber optic communication from and to the hotdeck.

Two kinds of optical communication have been implemented. In order to send and receive RS-232 commands a pair of RS-232 fiber optic interfaces from W&T [59] has been installed at the Micro IOC and at the pulser. The RS-232 commands are converted into optical signals, transferred over two (RX, TX) multimode optical fibers and converted back to RS-232 commands on the other side. In order to send the external trigger signal to the pulser and to receive the sync out pulse from the pulser an inexpensive interface has been built in-house making use of fiber optic BNC converters from VI Control Systems [60]. The +5 V TTL external trigger (50 – 500 ns) and the +3 V 200 ns TTL sync out signal are converted to optical pulses, sent over the same type of multimode optical fibers as the RS-232 communication and converted back to TTL signals on the other side. Rise and fall times of the converted signals are below 5 ns, the jitter of the delay between input and output is on the order of 10 ps.

All together, 4 optical fibers and 4 converter boxes take care of the entire communication between the pulser on HV potential and the control system. The system is inexpensive, easy to implement and reliable. Since the first assembly and throughout the commissioning and measurement phase, the fiber optic communication system has not failed once.

4.6.3 Timing System

A timing system is required to synchronize data acquisition with emission from the FEA. At SLS a global timing system exists that distributes among other signals a 3 Hz gun trigger signal. This 3 Hz signal is distributed through fiber optic cables all around the SLS experimental area. It was decided to use this signal as a master clock for the test stand. An event receiver card in the controls crate receives this timing signal and generates trigger signals for the pulser and the screen monitor cameras as well as the oscilloscope.

Depending on the user-defined setting, a 3 Hz, 1 Hz or single shot is triggered by the event receiver upon receiving the next 3 Hz master signal. The signal sent to the pulser is a +5 V TTL signal while the signal sent to the camera is a +1 V signal with a pulse length equal to the required camera shutter time. The same signal sent to the pulser can also be sent to the oscilloscope and used as a trigger for the Faraday cup readout although in practice it is more convenient to use the pulser sync out signal as an oscilloscope trigger. The timing card also allows separate delays to be set between the input and output signals.

During commissioning it was sometimes necessary to run the FEA at a high duty cycle. Instead of using the timing system, the internal clock of the pulser was used to pulse the FEA with up to 100 Hz. In this case the oscilloscope was triggered with the pulser sync out signal and the timing system was not used at all.

4.7 Diagnostics

The diagnostics module consists of a YAG screen, Faraday cup, slit/pinhole arrays, pepper-pot, phosphor screen, CCD cameras, and a set of motors and pneumatics capable of driving these devices into their proper positions. This section will first introduce the diagnostic hardware and then explain the two separate techniques used to reconstruct emittance and transverse phase space properties of the bunch.

4.7.1 Faraday Cup

A coaxial Faraday cup can be inserted into the beam from the side just after the solenoid magnet. The first DN 40 access port on the right side of the diagnostics cube holds the bellow and pneumatics to insert and extract the Faraday cup. It has a diameter of 20 mm and offers high bandwidth (> 4 GHz). The Faraday cup design has already been used successfully at the SLS linac for 90 keV electrons.

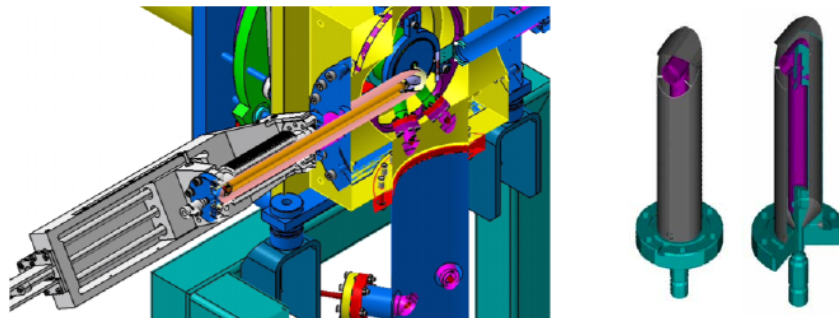


Figure 4.11: 3D rendering of the Faraday cup used at the test stand. The image on the left shows how the Faraday cup is inserted into the beam just after the solenoid. The image on the right shows the coaxial design of the Faraday cup.

Charge and time structure of the bunches emitted from the FEA are measured by reading out the FC signal on a high bandwidth oscilloscope; at the

test stand a LeCroy [61] WavePro[®] 7200 with 2 GHz and 20 GS/s is used. In order to protect the scope in case of HV arcs the internal termination is set to 1 M Ω and a 50 Ω terminator is added in parallel just before the scope. 1 V measured on the scope thus corresponds to 20 mA collected on the Faraday cup.

4.7.2 Screen Monitors and Camera Systems

The test stand has two separate screen monitor systems. The systems use the same CCD and frame grabber electronics, but the zoom optics and imaging medium are different. Both will be presented here.

YAG Screen Monitor

The YAG screen monitor consists of a YAG crystal, vacuum window, zoom optics and CDD camera. The 0.3 mm thick YAG crystal is installed at a 45° angle with respect to the beam axis; it has a diameter of 30 mm. The crystal is clamped to a holder driven in and out of the beam path in a bellow by a pneumatic system. A DN 40 flange with a vacuum window is installed at the end of the bellow. The beam is imaged on the YAG crystal surface and this image is observed through the vacuum window. A mirror deflects the image onto a vertically aligned lens system (see Fig. 4.12). Through proper positioning of two lenses the image is magnified and focused. Finally a Sony XC-55 CCD camera [62] images the YAG crystal and sends the CCD data to the frame grabber where the image is read out by the control system or displayed on a TV screen.

Since the crystal is oriented at a 45° with respect to the beam axis and the CCD camera observes the crystal at a 45° angle as well, the beam is imaged straight on and the round YAG crystal appears elliptic. For calibration purposes an additional mirror can be inserted between the vacuum window and the lens system. The lens system then images an object holder at the

exact same distance as the beam path. For calibration, a grid was clamped to the object holder revealing a calibration of 12.75 pixels/mm for maximum focusing. The resolution of the optical system is investigated in Section 5.2.



Figure 4.12: Photo of the YAG screen monitor optics during testing. The CCD is at the bottom of the vertically aligned lens system for zoom and focusing. The interface box connecting the CCD camera to the frame grabber and for connections to the lens motors is seen on the left.

Phosphor Screen Monitor

The phosphor screen monitor consists of a P43 phosphor coated movable vacuum window (30 mm diameter), movable zoom optics (Thales Optem[®] Telecentric Zoom 100 [63]) and CDD camera. The 6 – 8 μm thick P43 phosphor coating is optimized for 100 keV electrons; the substrate is aluminized to prevent the screen from accumulating a net charge when the beam is absorbed. The P43 coated vacuum window is attached to a holder that can be driven to different longitudinal positions along the beam path by a stepper motor. A total of 300 mm travel allows positioning of the P43 screen within the downstream half of the diagnostics cube or within a 150 mm drift behind the cube.

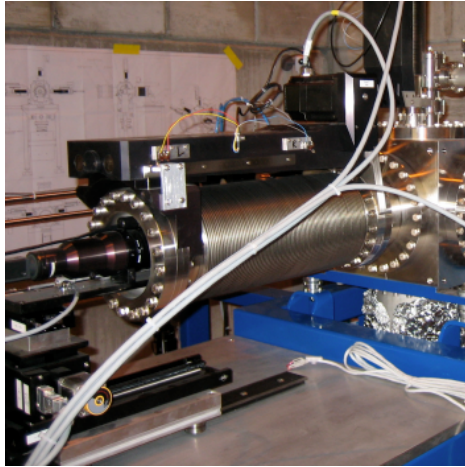


Figure 4.13: Photo of the phosphor screen monitor system. The P43 coated vacuum window is attached to a holder inside the bellows. The stepper motor moving the window is seen on top. The zoom optics and CCD camera are seen on the left. The optical components are installed on three stages with stepper motors for positioning with respect to the screen in all three dimensions.

Zoom optics and CCD camera are used to acquire the beam image on the phosphor screen. Since the screen can be moved to different longitudinal positions, the zoom and CCD can be moved longitudinally as well to give a well focused image at the zoom setting chosen. In addition the optical components can be moved transversely in order to choose the field of view on the phosphor screen. The positioning of the optical components is performed by three stepper motors and three stages on which the components have been mounted.

A grid can be attached to the vacuum window from the outside and used for calibration of the optical system since the displacement from the actual phosphor (given by the thickness of the window) is very small compared to the distance between screen and image plane; a calibration of 30.5 pixels/mm for the chosen focusing has been acquired. The resolution of the optical system is investigated in Section 5.2.

Screen Monitor Readout and Post-Processing

Both screen monitor CCD cameras are read out by a frame grabber VME card. The frame grabber card can be attached to a TV screen and the CCD images displayed in live TV mode. Of more interest for measurements is readout of the 8 bit intensity information of each CCD pixel. The control system makes this frame grabber data available as a 640×494 array of 8 bit values in an EPICS record. The IDL application CAM [64] reads this record and displays the intensity data as it would be displayed by a TV screen. In addition, it allows selection of a region of interest, does background subtraction, scaling, filtering, vertical and horizontal histograms of the image data, fits Gaussians to the histograms, returns standard deviations, amplitudes, etc. All CCD images presented in this thesis have been acquired through CAM.

4.7.3 Slit and Pinhole Inserts

For emittance and phase space reconstruction (see next sections) several masks are inserted into the beam path. In the test stand three different mask types are used: a single slit mask, a slit array mask and a pinhole array mask. Since the single slit and slit array are required twice (one horizontal and one vertical), two sets of masks are installed. The masks are made from laser eroded substrates of $100 \mu\text{m}$ tungsten. The slit width is $20 \mu\text{m}$ and the pitch is $170 \mu\text{m}$ as determined by simulations (see Section 3.3). For the pinhole array the hole diameter and pitch $50 \mu\text{m}$ and $320 \mu\text{m}$ also as determined by simulations.

Two aluminum holders carry three masks each. A stepper motor drives the holder into the beam path so the beam is obstructed by the chosen mask. The position of the holder is measured by a linear encoder with a resolution of $0.5 \mu\text{m}$. Currently these linear encoders are not yet installed. However, the position of the holder can be determined by counting motor steps as well.

One holder is inserted horizontally through the second DN 40 port on the left cube surface (opposite of the YAG insert). It holds a vertical single slit mask, a vertical slit array mask and pinhole array. The other holder is inserted vertically through a DN 40 port on the top cube surface; it holds a horizontal single slit, horizontal slit array and a second pinhole array. Both mask sets intercept the beam at the exact same longitudinal position as the YAG screen; this is important for the single slit emittance measurement as will be shown in the next section.

When the masks are properly inserted into the beam, most of the particles are stopped by the tungsten substrate. The remaining parts of the beam that pass the masks are called *beamlets*. The beamlets drift through the vacuum chamber until they hit the phosphor screen monitor and are imaged.

Since the masks are inserted at a fixed longitudinal position, transverse bunch properties can only be measured for this single location. To measure the evolution of transverse bunch properties from the solenoid exit through the drift section in the diagnostics cube, an additional measurement device has been built, the so-called *pepper-pot*. It consists of an additional pinhole mask fastened to the end of a 300 mm cylindrical holder which is attached to the inside of the phosphor coated vacuum window. The pinhole array is driven through the beam longitudinally (300 mm travel) while the beamlets are imaged on the phosphor screen in the same way as for the fixed pinhole arrays. The longitudinal sampling comes at the expense of a fixed 300 mm distance between pinhole mask and screen, i.e. the beamlet drift distance cannot be varied to optimize the beamlet image (maximize beamlet image size without introducing beamlet image overlap). A comparison of the two measurement modes is given in Fig. 4.14.

4.7.4 Single Slit Measurement Technique

If the phase space distribution of a bunch is elliptic in both transverse planes, the emittance can be measured with a single slit image assuming the beam

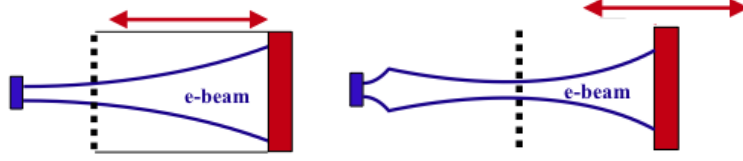


Figure 4.14: Measurement modes with pinhole array and pepper-pot. In the unfocused case (left) the pepper-pot and screen are at a fixed distance of 300 mm and are moved together through the beam. In the focused case (right) the pinhole array is inserted at a fixed location and the phosphor screen is moved to optimize the beamlet image.

size is known at the location of the slit mask. According to Eq. (2.17) the transverse RMS emittance is given by

$$\varepsilon_u = \sqrt{\langle u^2 \rangle \langle u'^2 \rangle - \langle uu' \rangle^2}. \quad (4.1)$$

For an elliptic phase space distribution there is a linear correlation between divergence and location which can be subtracted [65]

$$u' \longmapsto \tilde{u}' = u' - m u, \quad (4.2)$$

where $m = \langle uu' \rangle / \langle u^2 \rangle$ is the inclination of the phase space ellipse. The RMS emittance is then given by

$$\varepsilon_u = \sqrt{\langle u^2 \rangle \langle u'^2 \rangle - \langle uu' \rangle^2} \longmapsto \sqrt{\langle u^2 \rangle \langle \tilde{u}'^2 \rangle}. \quad (4.3)$$

This last equation demonstrates why knowledge of beam size and uncorrelated divergence spread at one location is sufficient to derive the emittance (for an elliptic phase space distribution). At the test stand the RMS beam size at the location of the single slit mask is measured with the YAG screen monitor. Once the beam size is known, the YAG is retraced, the single slit mask is inserted and the beamlet is imaged on the phosphor screen monitor. The uncorrelated divergence spread in the bunch is then related to the slit image RMS width by

$$\langle \tilde{u}'^2 \rangle = \frac{\sigma_u^2}{L^2}, \quad (4.4)$$

where L is the beamlet drift distance between the single slit mask and the phosphor screen and σ_u is the RMS slit image width. This approximation is valid for non space charge dominated beamlets¹ and if the slit width is small compared to the image width: $\sigma_u \gg d$. In order to verify the latter condition the uncorrelated divergence spread can be calculated with several slit images taken at different distances for the mask; the error due to the finite slit width is then easily estimated (see Section 6.3.2).

4.7.5 Slit Array & Pinhole Measurement Technique

The disadvantage of the single slit emittance measurement technique is that it requires knowledge of the beam size at the mask location, requires elliptic phase space distributions and renders only the emittance; the other Courant-Snyder parameters cannot be deduced because the correlation between location and divergence is unknown. To overcome these limitations the slit array measurement technique is introduced: A slit array is inserted into the beam and the beamlets emerging from the mask drift to the phosphor screen where they are imaged. Since the pitch of the slits on the mask is known, the correlated and uncorrelated divergence spreads can be deduced from the slit array image. And since the mask size is ideally chosen so that the beam only illuminates some slits, the beam size can be deduced from the same slit array image without any additional beam size measurement.

A very lucid description of this measurement technique is given in [66].² In a first step the centroids of the imaged beamlets are used to reconstruct the

¹This is usually the case since the beamlet has roughly the same dimension as the beam in one spatial coordinate, but the amount of charge within the beamlet is one or two orders of magnitude lower than in the entire bunch. For highly space charge dominated beams, slit, slit array, or pinhole array measurement techniques are the only applicable direct measurement methods: since the mask stops a large amount of the bunch charge the beamlets are emittance dominated even for highly space charge dominated beams.

²The referenced paper by Anderson et al. contains an error that was discovered while writing the reconstruction code for the emittance measurement analysis. Equation (2) in the paper mixes uncentered positions $\langle u_m^2 \rangle$ and centered divergences $(\bar{u}'_m)^2$. Both have to

divergence centroids for each beamlet m according to

$$\bar{u}'_m = \frac{\langle u_m - \bar{u}_m \rangle}{L} = \frac{\langle u_m - m w \rangle}{L} \quad m \in \mathbb{N}_0, \quad (4.5)$$

where w is the pitch of the slits on the slit array. The averages $\langle \rangle$ taken in this section are weighted averages for each beamlet m where the intensity variation within the beamlet image is used. Hence avoiding saturation on the CCD and proper background subtraction are crucial for good reconstruction (see Section 6.3.4).

The RMS divergence spread in each beamlet is then calculated with the RMS beamlet image width according to

$$\sigma'_m = \sqrt{\langle (u_m - \bar{u}_m)^2 \rangle / L^2 - (\bar{u}'_m)^2} = \sqrt{\langle (u_m - m w)^2 \rangle / L^2 - (\bar{u}'_m)^2}. \quad (4.6)$$

The previous Eqs. (4.5) and (4.6) require a non space charge dominated beam and assume that the slit width is small compared to the beamlet image width: $d \ll \sqrt{\langle (u_m - \bar{u}_m)^2 \rangle}$.

The slit positions $m w$ and divergence centroids \bar{u}'_m are not centered in phase space. This is achieved by two simple corrections

$$\bar{u}_m = m w \quad \mapsto \quad m w - \frac{\sum_{m=1}^N I_m m w}{\sum_{m=1}^N I_m}, \quad (4.7)$$

$$\bar{u}'_m = \frac{\langle u_m - m w \rangle}{L} \quad \mapsto \quad \frac{\langle u_m - m w \rangle}{L} - \frac{\sum_{m=1}^N I_m \bar{u}'_m}{\sum_{m=1}^N I_m}, \quad (4.8)$$

where I_m is the image intensity of beamlet m . From this centered phase space distribution data for each beamlet, the second order moments of the entire bunch distribution can be calculated

$$\langle u^2 \rangle = \frac{\sum_{m=1}^N I_m \bar{u}_m^2}{\sum_{m=1}^N I_m}, \quad (4.9)$$

be chosen either centered $\langle u_m - \bar{u}_m \rangle$ or uncentered $\langle u_m \rangle$. Equation (4.6) here uses centered values. The alternative definition using uncentered values $\sigma'_m = \sqrt{\langle u_m^2 \rangle / L^2 - \langle u_m / L \rangle^2}$ is equivalent.

$$\langle u'^2 \rangle = \frac{\sum_{m=1}^N I_m (\bar{u}_m'^2 + \sigma_m'^2)}{\sum_{m=1}^N I_m}, \quad (4.10)$$

$$\langle uu' \rangle = \frac{\sum_{m=1}^N I_m \bar{u}_m \bar{u}_m'}{\sum_{m=1}^N I_m}. \quad (4.11)$$

The emittance and Courant-Snyder parameters are now easily calculated from the second order moments of the bunch distribution

$$\varepsilon_u = \sqrt{\langle u^2 \rangle \langle u'^2 \rangle - \langle uu' \rangle^2}, \quad (4.12)$$

$$\begin{aligned} \beta_u &= \frac{\langle u^2 \rangle}{\varepsilon_u}, \\ \alpha_u &= -\frac{\langle uu' \rangle}{\varepsilon_u}, \\ \gamma_u &= \frac{\langle u'^2 \rangle}{\varepsilon_u} = \frac{1 + \alpha_u^2}{\beta_u}. \end{aligned} \quad (4.13)$$

At the test stand the post-processing code RECONSTRUCTION has been written in GNU Octave [67]; it takes the beamlet image data, subtracts background, and calculates all the properties derived in Eq. (4.5) – (4.11) for all beamlets. The emittance and Courant-Snyder parameters are calculated according to Eqs. (4.12) and (4.13). Finally, every pixel on the CCD is mapped to a cell in phase space by making use of the drift transfer matrix for the beamlets

$$\begin{pmatrix} u_0 \\ u'_0 \end{pmatrix} \longmapsto \begin{pmatrix} u_0 + L u'_0 \\ u'_0 \end{pmatrix} \quad (4.14)$$

stating that a square cell in the phase space plane is transformed to a parallelogram by a drift. This mapping is inverted and used to calculate a phase space density plot directly from the CCD image. An example of such an emittance measurement and the post-processing done with RECONSTRUCTION is given in Section 6.3.4.

The phase space reconstruction technique presented here gives emittance, Courant-Snyder parameters and phase space density information for one

plane in phase space per shot. In order to reconstruct the full 4D transverse phase space two slit array images are required: one with horizontal slits to reveal the vertical phase space plane and once with vertical slits to reveal the horizontal phase space. This could be accomplished with a single image if the two slit arrays were placed right behind each other. More practical is to use a pinhole array where many holes are distributed with a constant pitch in vertical and horizontal direction on a mask. Using such a pinhole array, a single beamlet image reveals the entire 4D transverse phase space distribution. Examples for pinhole measurements will be presented in Section 6.3.4.

Chapter 5

Commissioning of the Test Stand

This chapter reports on commissioning of the test stand. Prior to first operation, two important calibration measurements had to be performed:

- The solenoid strength had to be measured precisely to model the beam dynamics used for measurement analysis.
- The resolution of the optical systems used at the two screen monitor devices had to be determined because all transverse beam measurements rely on analysis of image data taken with these systems.

The first two sections will detail these calibration measurements and show that the systems fulfill the requirements of the test stand experiments. The final section is dedicated to the startup and first operation of the test stand. The startup strategy and initial operation experience will be reported.

5.1 Solenoid Magnet Calibration

This section is a summary of [68]. Since the solenoid magnet windings and yoke are welded into a UHV compatible steel casing (see Section 4.3.4), cali-

bration measurements had to be performed prior to welding and installation into the test stand. Any deviations from the original specifications could no longer be corrected once the magnet was installed in the casing. It was therefore decided to perform bench-tests and calibration just after fabrication and before complete assembly. This section describes these tests and demonstrates the magnet calibration.

5.1.1 Measurement Setup

The magnet calibration was performed at the SLS magnet testing lab. A longitudinal Hall probe from F. W. Bell [69] connected to a Gaussmeter was used for magnetic field measurements. The Hall probe was held in place by an aluminum cylinder which was attached to a 3D linear mover. The setup is shown in Fig. 5.1.

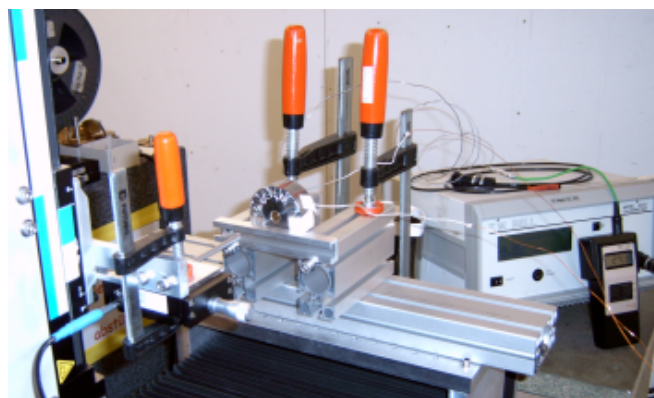


Figure 5.1: Measurement setup for calibration of the solenoid magnet. The Hall probe can be moved through the solenoid magnet by the 3D mover system. Temperature of the windings and Hall probe signal are read out and displayed directly.

The probe cylinder had a diameter of roughly 6 mm allowing it to be moved through the solenoid on and off axis. The solenoid was clamped to the base of the 3D linear mover; the probe cylinder was centered vertically and

horizontally within the solenoid's 10 mm aperture by eye and its horizontal inclination was adjusted with a water level.

The solenoid was powered by the exact same digital 24 V power supply to be installed at the test stand. The digital control interface allows the current to be set between 0 – 10 A; the power supply adjusts the voltage to keep the current constant. A 6.61Ω ohmic resistance at room temperature has been measured for the solenoid windings; assuming this temperature remains constant, the power supply should be capable of delivering the maximum specified current of 3.6 A. Due to Joule heating during operation, the ohmic resistance is expected to rise, thus reducing the maximum achievable current.

The coordinate system of the 3D linear mover is depicted in Fig. 5.2. Shifts in positive z direction are in the direction of beam motion. It was chosen to set $z = 0$ when the Hall probe cylinder's front surface (where the Hall probe is assumed) is 10 mm upstream of the entry yoke disk; the solenoid center is at $z = 24$ mm due to the 4 mm thickness of the yoke disk. The transverse coordinates x and y are zero on axis.

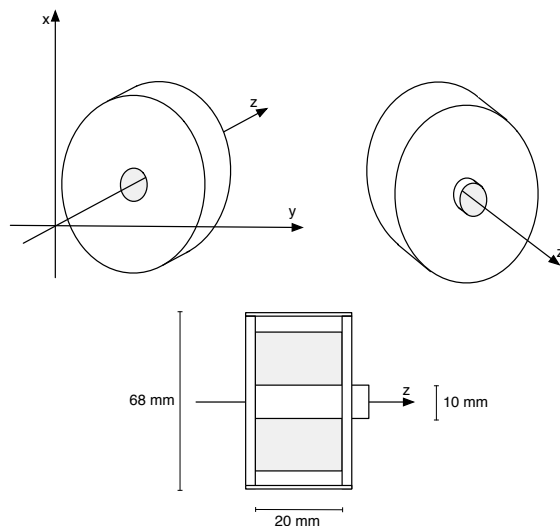


Figure 5.2: The coordinate system used for solenoid calibration measurements. Solenoid magnet dimensions are given.

5.1.2 Background Measurement

The Gaussmeter displays the longitudinal magnetic field B_z in units of Gauss. Throughout this section, the common SI unit Tesla shall be used instead. The Gaussmeter was calibrated in such a way that it showed 0.0 mT at the center of the solenoid while the power supply was on, but set to 0.0 A current. Once the Hall probe was moved outside of the solenoid, the Gaussmeter showed increasing field strength; this is due to the fact that the solenoid shields its inside from the earth magnetic field. The effect is shown in Fig. 5.3; the solenoid shields a background field on the order of ≈ 0.4 mT at its center.

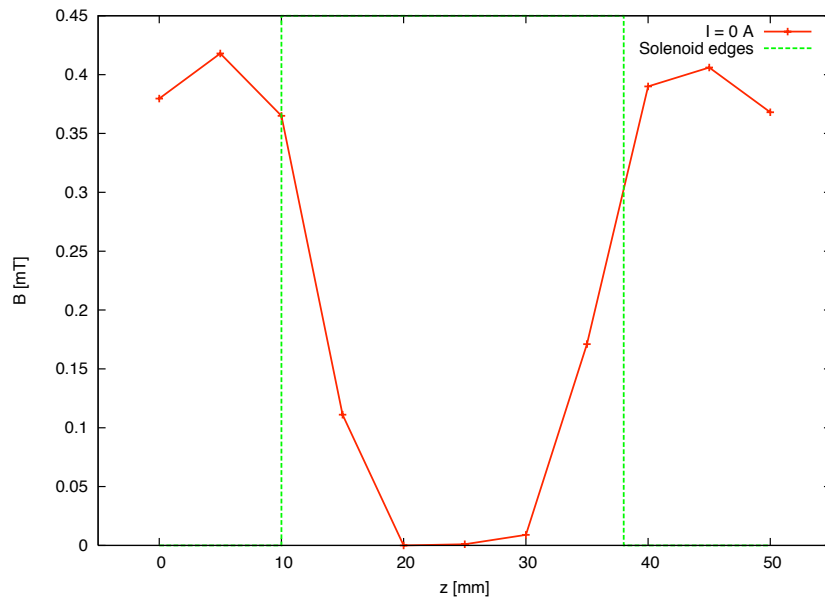


Figure 5.3: The background measurement showing how the solenoid (green dotted line indicates the solenoid edges) shields the earth magnetic field strength.

5.1.3 Field Calibration

In a first measurement, the relation between applied solenoid current and longitudinal magnetic field at the solenoid center was determined. The calibrated Hall probe was positioned on axis at $z = 24$ mm. For various current settings, the resulting longitudinal magnetic field was measured as shown in Fig. 5.4.

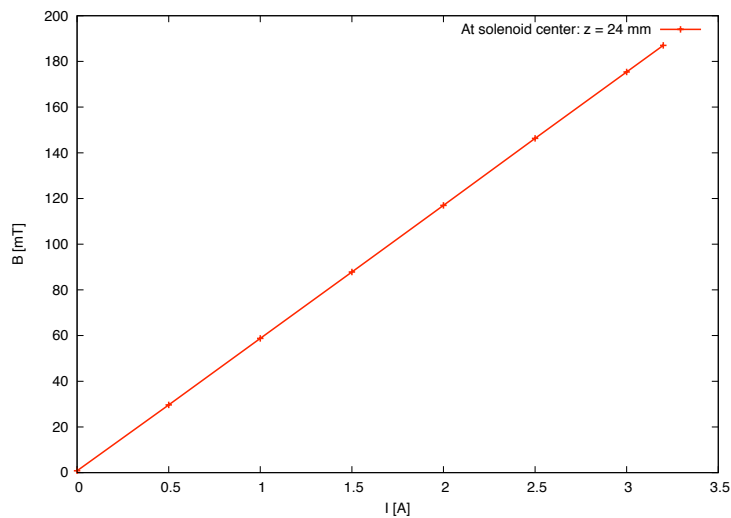


Figure 5.4: Solenoid calibration data: longitudinal magnetic field on axis as a function of solenoid current. The field measurement was performed at the axial center of the solenoid.

The solenoid current was increased from 0.0 A to 3.2 A where the power supply voltage limit of 24 V was reached. This setting reveals an ohmic resistance of 7.5Ω , which is slightly higher than the resistance originally measured at room temperature. The increase is due to the heating of the (uncooled) solenoid windings; at a current of 3.2 A, the temperature of the windings had reached 79°C .

The result shows a linear dependence between longitudinal magnetic field and applied current: Per Ampere of current, the longitudinal field at the

center of the solenoid increases by 58.2 mT. This linear dependence confirms that the solenoid material is well away from saturation. The required field strength of roughly 120 mT (to create a beam waist at the location of the YAG screen monitor, slit, and pinhole masks) is thus easily reached; tuning of the solenoid around this value should cause no problems. After reaching the maximum current, the current was reduced stepwise to zero and the resulting field was compared to the initially measured field. A difference of roughly 2 mT was measured which shows only slight hysteresis.

5.1.4 Longitudinal Field Scans

In the next measurement, the longitudinal magnetic field induced by the solenoid at different longitudinal positions on as well as off axis was determined for a current of 2.0 A. The scanning range was between $z = -50$ mm and $z = +90$ mm which corresponds to a location 60 mm before the solenoid entry yoke disk respectively 52 mm behind the exit yoke disk.

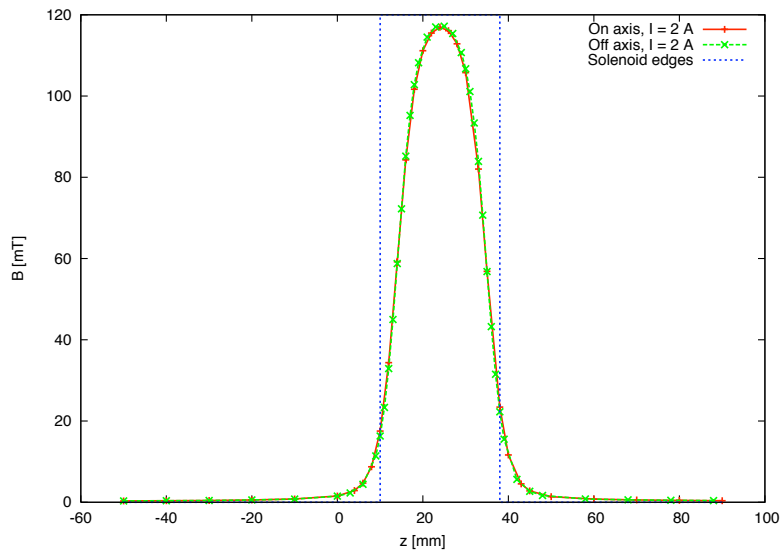


Figure 5.5: Longitudinal magnetic field scans on and off axis performed at a solenoid current setting of 2 A.

For the off-axis measurement the Hall probe was moved away from the axis by $\Delta x = +1$ mm and $\Delta y = +1$ mm, giving a radial offset of 1.4 mm. This is a large offset when considering the size of the anode iris $r_{\text{iris}} = 750 \mu\text{m}$. The measured field strengths for both scans are shown in Fig. 5.5. The difference between on and off axis scans are plotted in Fig. 5.6.

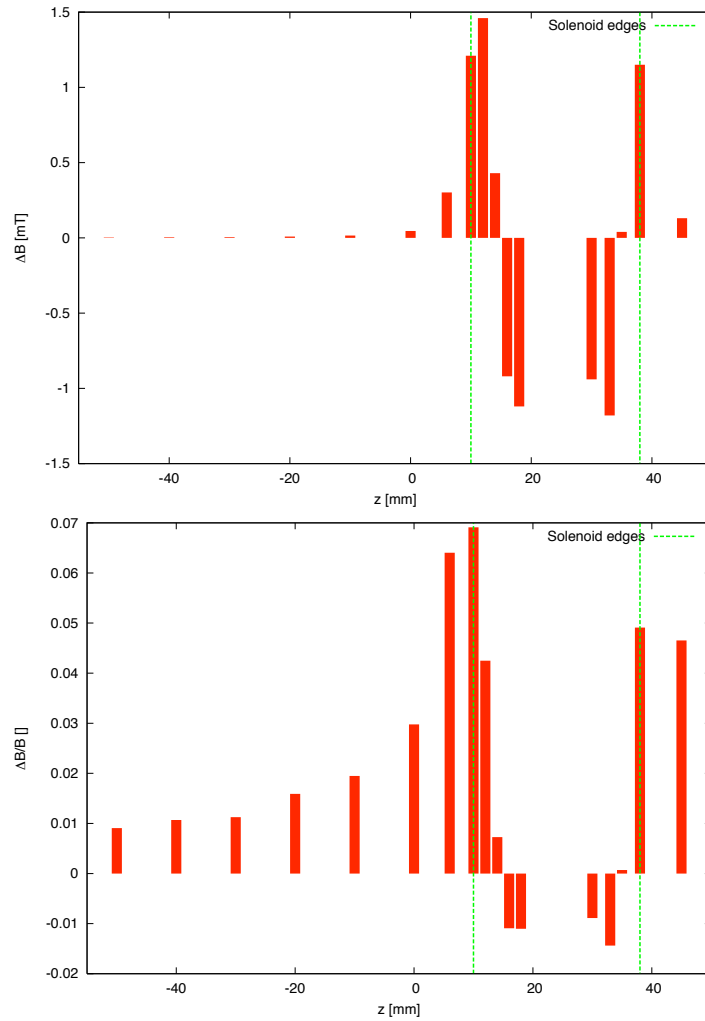


Figure 5.6: Absolute and relative difference between on and off axis longitudinal scans performed at 2 A solenoid current. The missing difference bars within the solenoid are due to a lack of measurements at common s positions, not due to vanishing difference.

At the beginning of the scan, the field strength on axis is higher than off axis; this difference increases in the fringe field (non-zero radial field components off axis). At the entry of the windings the sign of this difference changes and the field strength off axis remains larger within the volume enclosed by the solenoid windings. At the solenoid exit there is again a change of sign and the on axis field strength is larger than the off axis field strength throughout the fringe field. The maximum differences are found in the fringes and are on the order of roughly 1.5 mT or 7%. Far outside the solenoid the differences are about 1%; at the center of the solenoid 1% – 2% difference were measured.

5.1.5 Fringe Field Measurements

In a final experiment, the fringe field in front of the solenoid was scanned. The Hall probe was brought into position at $z = 9$ mm which is 1 mm in front of the entry yoke disk. The solenoid current was again set to 2.0 A. In x direction the scan passed from -7 mm to $+7$ mm in steps of $\Delta x = 1$ mm and in y direction from -7 mm to $+7$ mm in steps of $\Delta y = 1$ mm. Both measurement curves are plotted in Fig. 5.7.

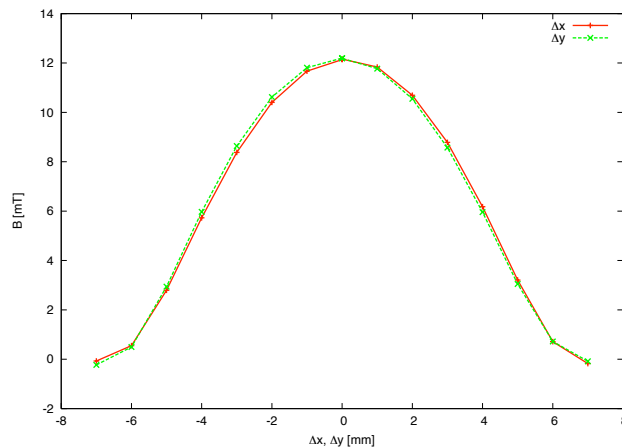


Figure 5.7: Longitudinal magnetic field measurement in the solenoid fringe field. The two curves show scans for varying Δx respectively Δy .

The longitudinal magnetic field vanishes at ± 7 mm. As the Hall probe is moved towards the solenoid axis, the field strength increases to 12 mT. For both scans the field strength shows symmetrical behavior on both sides. Qualitatively the field strengths are identical for x and y direction scans which indicates rotational symmetry of the solenoid. The minor difference between the two curves is a slight systematic shift of the Δy curve with respect to the Δx curve, which can be explained by a marginal misalignment of the Hall probe with respect to the solenoid, i.e. the Hall probe was not perfectly centered within the solenoid for both the x and the y plane.

From these measurements a set of conclusions for the operation of the solenoid in the gun test stand can be gathered: The only observable hysteresis effects are within 1 – 2 mT. The solenoid is operated well away from saturation within the entire tuning range of the power supply. The longitudinal magnetic field shows longitudinal symmetry, the longitudinal fringe field shows rotational symmetry. Misalignment tolerance is high since only slight differences were measured for on and off axis longitudinal fields. From the on axis longitudinal scans an integrated squared field of¹

$$\int \frac{B^2}{I^2} dz = 5.705 \cdot 10^{-5} \text{ T}^2 \text{ m A}^{-2} \quad (5.1)$$

is derived. With the peak field B_{\max} , the effective length of the solenoid magnet is then given by²

$$l_{\text{eff}} = \frac{\int B^2 dz}{B_{\max}^2} = 16.691 \text{ mm}. \quad (5.2)$$

¹The integral is normalized with the square of the solenoid current because the solenoid field depends linearly on the solenoid current.

²The quadratic field integral dependence of the effective length is different from the usual definitions for quadrupole magnets. This is due to the quadratic dependence of the solenoid focusing strength k on the solenoid field [see Eq. (6.3)].

5.2 Calibration of the Optical System & Point-Spread Function

All measurements that make use of the phosphor screen monitor at the test stand will ultimately depend on the resolution of the optical system used to image the phosphor screen. The aim of the measurements presented in this section is to investigate how well a measured image corresponds to the real light pattern. For this the so called *Point-Spread function* (PSF) is experimentally determined. This section is a summary of [70].

5.2.1 Measurement Setup

The experimental setup is schematically shown in Fig. 5.8. The goal is to determine the PSF for the zoom optics, the CCD camera and the frame grabber system *as a unit*. Usually, the PSF for an optical system is defined as the 2D intensity distribution in the image plane, produced by a point source in the source plane. In the notation used here, the PSF is the 2D *measured* light distribution, produced by a point source. Therefore, it includes all possible diluting contributions, not only optical aberrations and diffraction effects, but also for example CCD readout noise, CCD pixel resolution, frame grabber ADC noise, vibrations etc.

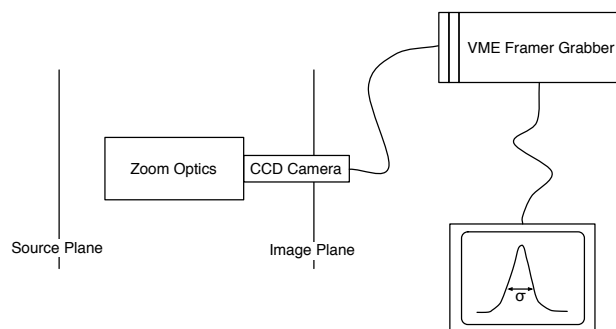


Figure 5.8: Schematic of the experimental setup to determine the PSF of the entire optical system (zoom optics, CCD camera, frame grabber).

While measuring the PSF it was attempted to optimize the whole setup, which is equivalent to minimizing the PSF. This includes for example carefully adjusting the CCD chip plane correctly to the image plane. Finally, all different adjustments then gave good “hands-on feeling” for what the most delicate issues are in order to reach optimal results.

5.2.2 Horizontal and Vertical Profile Measurements

First measurements were done with a $15\ \mu\text{m}$ pinhole array. Each pinhole is $15\ \mu\text{m}$ in diameter; the horizontal and vertical pitch is $0.7\ \text{mm}$ and $0.4\ \text{mm}$ respectively. The precision of these values is not quite clear, but roughly it should be 1% for the spacing and 5% – 10% for the actual diameter. The thickness of the pinhole array mask is $150\ \mu\text{m}$. This thickness is small enough in order not to cause any ambiguity problems defining the source plane. The source is arranged as depicted in Fig. 5.9. A halogen lamp is pointed towards a diffuser, which in turn illuminates the pinholes. In this way the pinholes are uniformly illuminated and the light emerging from each part of the pinhole is uniform in intensity over the entire area of the pinhole. Only the pinholes close to the optical axis are used for calibration and PSF measurements.

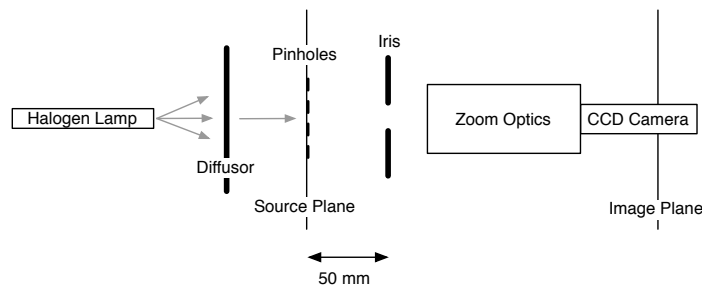


Figure 5.9: Schematic of the PSF measurement setup. Source and image plane are indicated.

All measurements were performed at the maximum setting of the zoom optics. With this setting the calibration factor was $(3.81 \pm 0.05)\ \mu\text{m}/\text{pixel}$ in

both directions. If always the same four pinholes were used, the uncertainty decreased to $\pm 0.01 \mu\text{m}/\text{pixel}$, but the measured value then depended on the quartet chosen. This gave the indication that the measurement system was more accurate than the mechanical distances between the holes. According to the vendor, the CCD camera has a pixel size (center to center) of $7.4 \mu\text{m}$ in both directions; this gives magnification factors of 1.94 in both directions in good agreement with manufacturer's specifications stating a magnification of 1.9 [63].

Figures 5.10 – 5.13 show horizontal and vertical profiles for one pixel row respectively column, going through the most intense pixel. All profiles are scaled up to roughly 255 units (8 bit ADC) at the peak. Therefore, to judge the true peak intensity in the 0 to 255 unit scale, the background level has to be observed. Figure 5.10 shows an image taken with a maximum very close to 255 units (increased halogen lamp setting) and a background of roughly 16 units. Figure 5.11 shows profiles for a lower peak intensity (decreased halogen lamp setting), resulting in a higher background level of approximately 25 units. This corresponds to a peak intensity of roughly $225 \times 16 / 25 = 163$ units. The RMS values of the Gaussian fits are almost identical for the two samples, indicating that the linearity of the CCD is satisfactory in this intensity interval. It is believed that the linearity is good in a much wider intensity range, but since it is not specified in the camera manual, it was decided to at least verify it in the region of interest. Going to peak intensity values lower than 100 is not preferable due to poor fit accuracy.

Figure 5.10 shows an optimized iris setting; signal amplitude was maximized (without getting into saturation) while maintaining the smallest spot size. For this optimum the iris opening in front of the zoom optics was set to accept a circular opening angle of $\approx 45 \text{ mrad}$ ($= r_{\text{iris}}/l_{\text{source-iris}}$).

Figures 5.12 and 5.13 show the resulting profiles when the opening angle is $\approx 65 \text{ mrad}$ and $\approx 25 \text{ mrad}$ respectively. For 65 mrad opening angle tails are clearly visible in the image profiles. It is believed that the zoom optics do not handle the peripheral light as well as the close-to-axis light likely due

to internal irises limiting the acceptance angle between 60 and 65 mrad; one gains in image quality by going down to at least 55 mrad. This confirms the specifications given by the manufacturer stating that the numerical aperture is 62 mrad at magnification 1.9 [63]. In the interval between 55 and 35 mrad the image quality stays almost constant, while going further down to 25 mrad the diffraction effect starts to dominate: an increase of $\sigma_{x,y}$ can be seen when comparing Fig. 5.13 to Fig. 5.10.

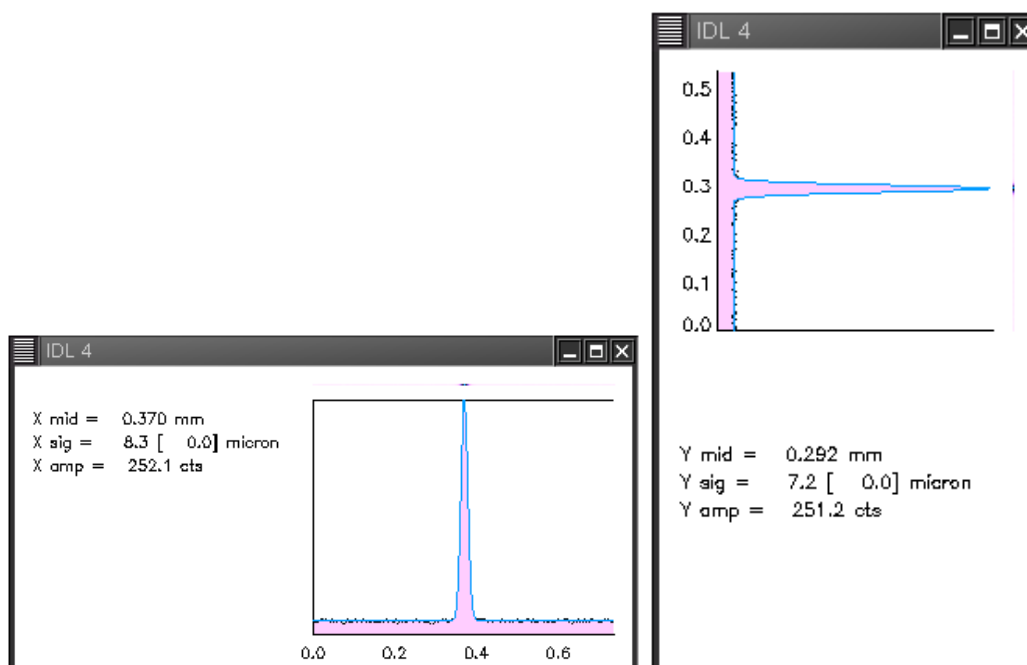


Figure 5.10: Horizontal and vertical profiles for a 15 μm pinhole with halogen lamp set to **high** intensity and iris set to accept ≈ 45 mrad.

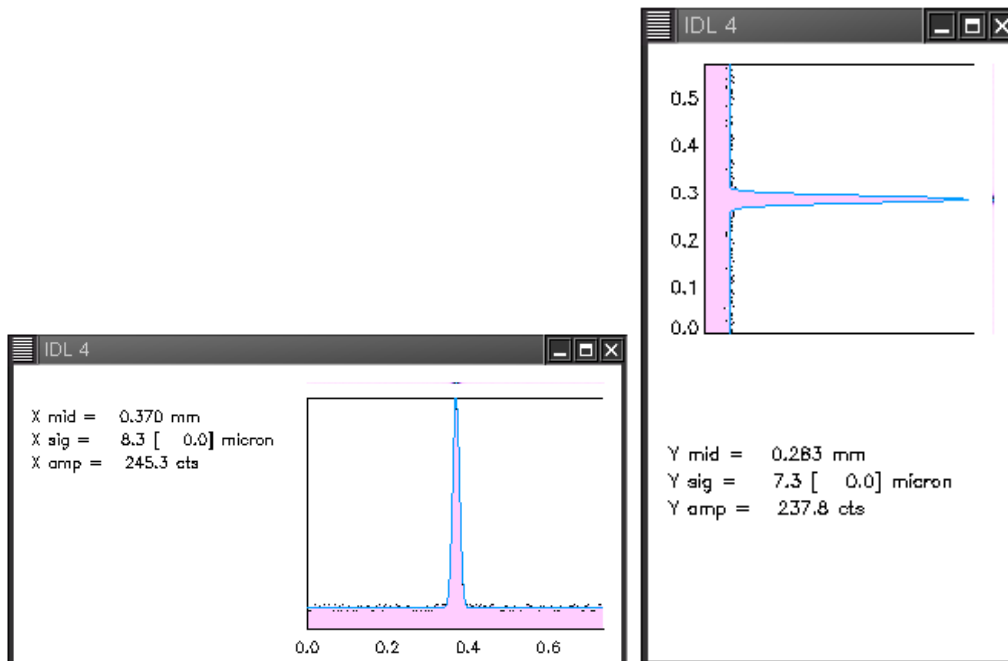


Figure 5.11: Horizontal and vertical profiles for a 15 μm pinhole with halogen lamp set to **reduced** intensity and iris set to accept ≈ 45 mrad.

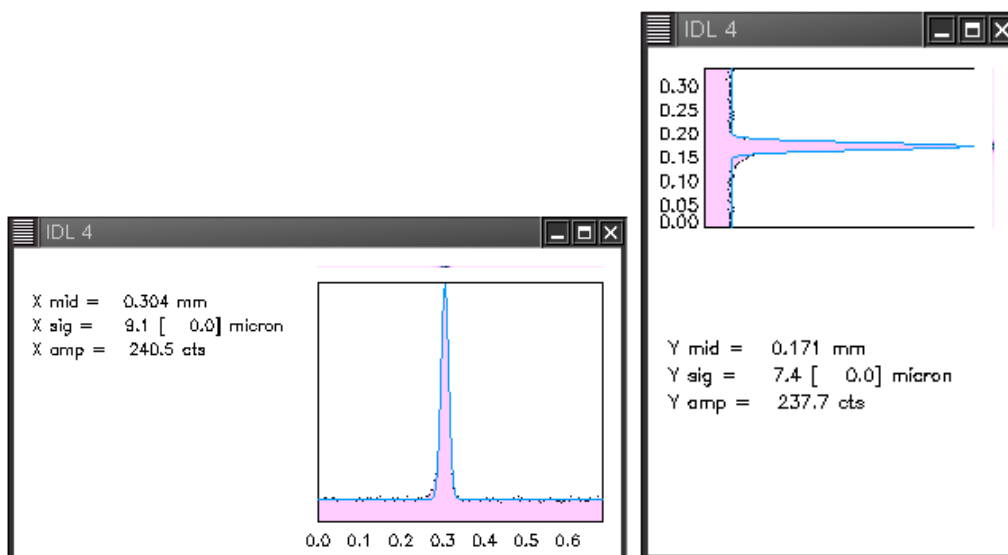


Figure 5.12: Horizontal and vertical profiles for a 15 μm pinhole with halogen lamp set to **reduced** intensity and iris fully open accepting ≈ 65 mrad. Tails presumably due to off-axis light are clearly visible.

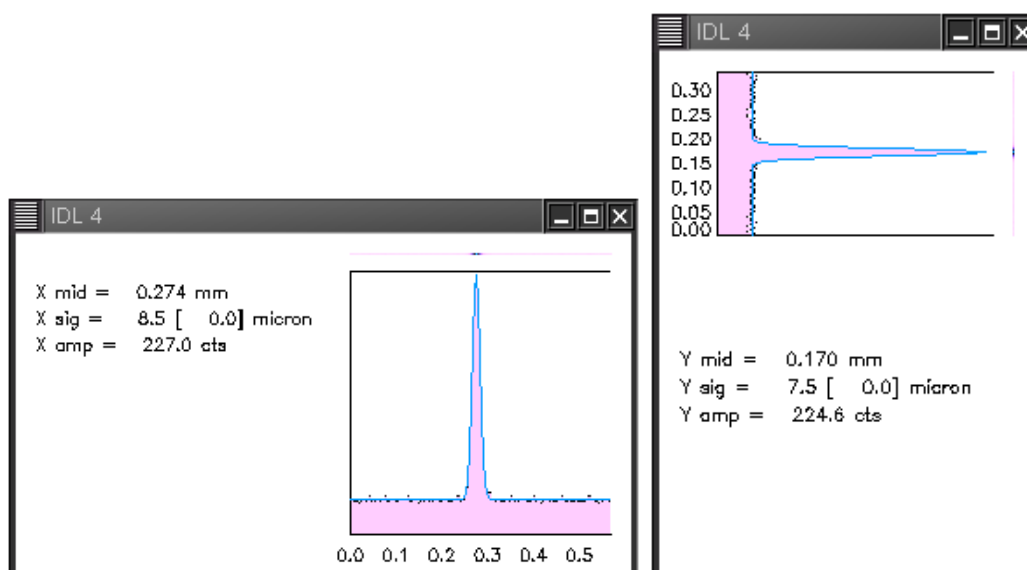


Figure 5.13: Horizontal and vertical profiles for a $15\ \mu\text{m}$ pinhole with halogen lamp set to **high** intensity and iris closed accepting $\approx 25\ \text{mrad}$.

Figure 5.14 shows the horizontal and vertical profiles for a $10\ \mu\text{m}$ pinhole, using a limiting aperture to block off-axis rays. The sigma values should be multiplied by the calibration factor 3.81, resulting in $\sigma_x = 5.7\ \mu\text{m}$ and $\sigma_y = 5.3\ \mu\text{m}$. For comparison, Fig. 5.15 shows the profiles without blocking the off-axis rays; again tails are clearly visible.

Figure 5.16 shows the horizontal and vertical profiles for a $5\ \mu\text{m}$ pinhole, using a limiting aperture to block off-axis rays. The resulting width is $\sigma_x = 3.8\ \mu\text{m}$ and $\sigma_y = 3.4\ \mu\text{m}$. For comparison, Fig. 5.17 shows the profiles without blocking the off-axis rays. Finally, an example for the 2D distribution of a pinhole image on the phosphor screen is given in Fig. 5.18.

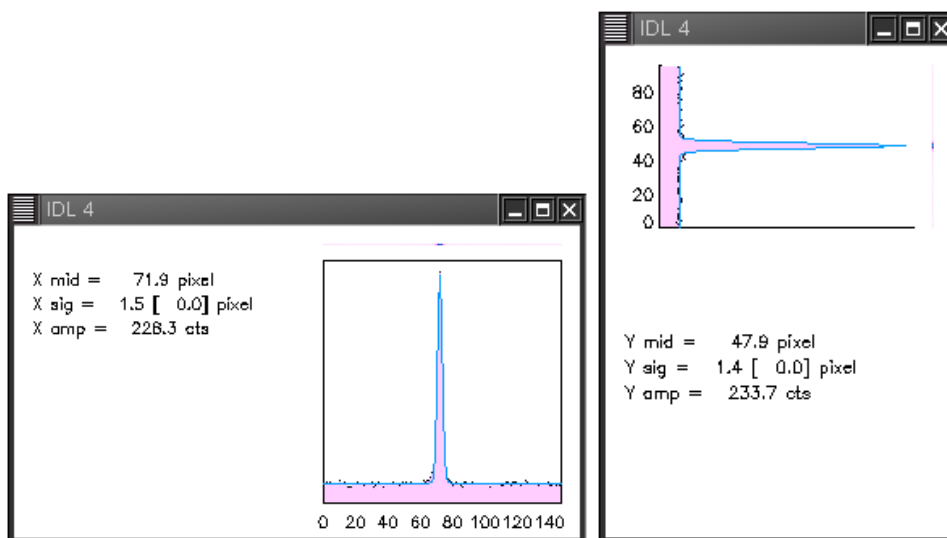


Figure 5.14: Horizontal and vertical profiles for a 10 μm pinhole with halogen lamp set to **reduced** intensity and iris set to accept ≈ 45 mrad. The $\sigma_{x,y}$ have to be multiplied by the calibration factor 3.81, resulting in $\sigma_x = 5.7 \mu\text{m}$ and $\sigma_y = 5.3 \mu\text{m}$.

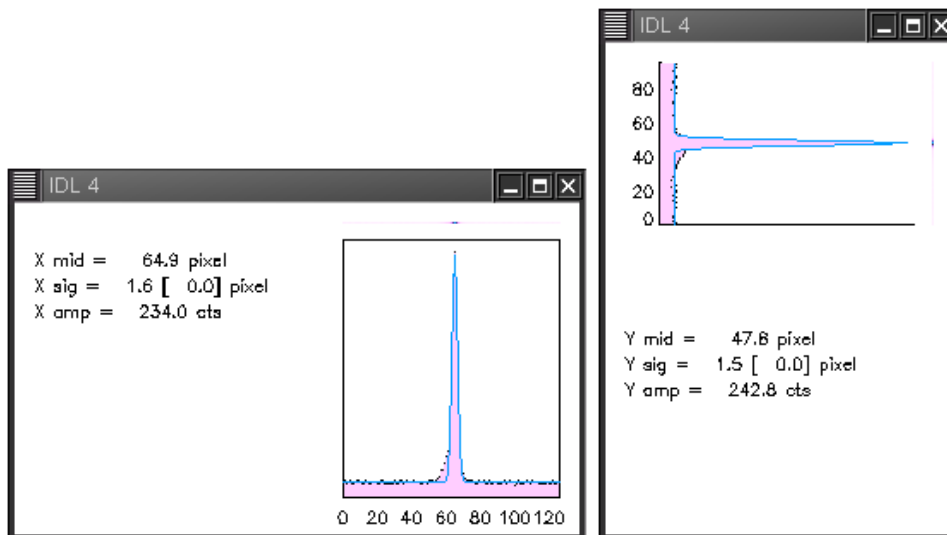


Figure 5.15: Horizontal and vertical profiles for a 10 μm pinhole with halogen lamp set to **reduced** intensity and iris fully open accepting ≈ 65 mrad. The $\sigma_{x,y}$ have to be multiplied by the calibration factor 3.81, resulting in $\sigma_x = 6.1 \mu\text{m}$ and $\sigma_y = 5.7 \mu\text{m}$. Tails due to off-axis light are clearly visible.

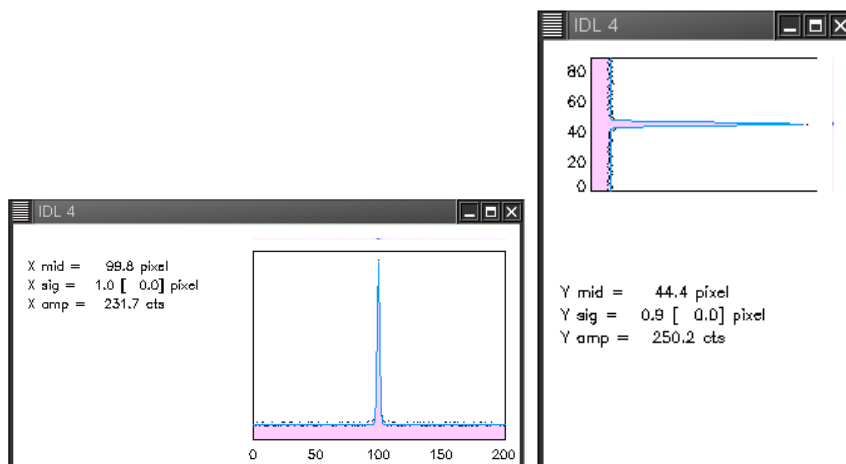


Figure 5.16: Horizontal and vertical profiles for a $5\ \mu\text{m}$ pinhole with halogen lamp set to **high** intensity and iris set to accept ≈ 45 mrad. The $\sigma_{x,y}$ have to be multiplied by the calibration factor 3.81, resulting in $\sigma_x = 3.8\ \mu\text{m}$ and $\sigma_y = 3.4\ \mu\text{m}$.

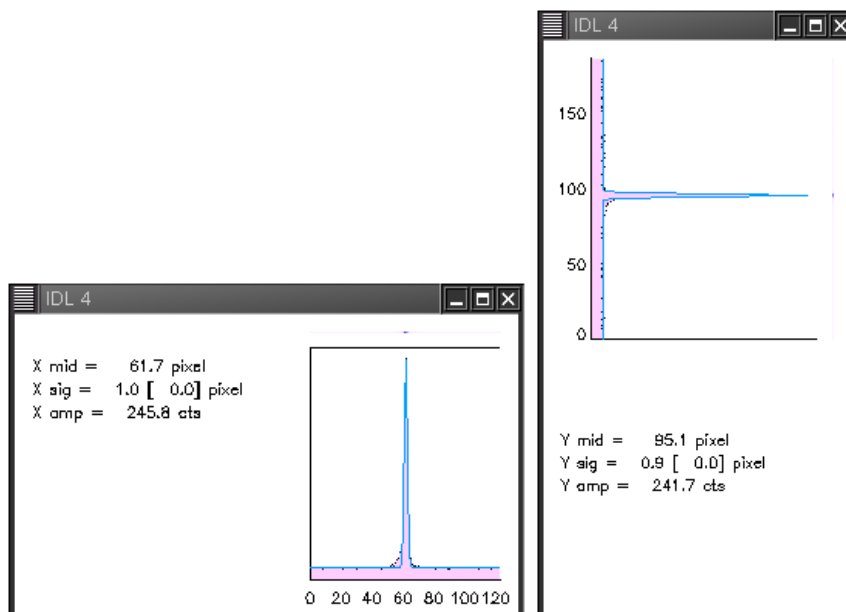


Figure 5.17: Horizontal and vertical profiles for a $5\ \mu\text{m}$ pinhole with halogen lamp set to **high** intensity and iris fully open accepting ≈ 65 mrad. The $\sigma_{x,y}$ have to be multiplied by the calibration factor 3.81, resulting in $\sigma_x = 3.8\ \mu\text{m}$ and $\sigma_y = 3.4\ \mu\text{m}$. Tails due to off-axis light are clearly visible.

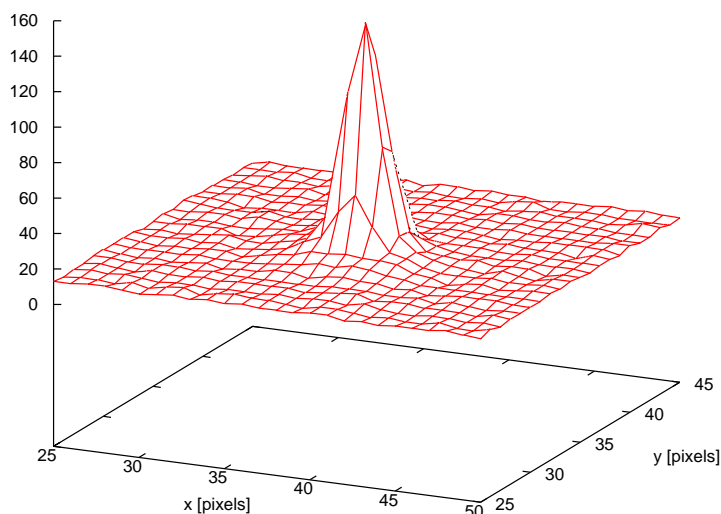


Figure 5.18: 2D intensity plot of a $5 \mu\text{m}$ pinhole with halogen lamp set to high intensity and iris set to accept $\approx 45 \text{ mrad}$. A background level of roughly 16 is observed. The results of the Gaussian fits for the entire hole image are $\sigma_x = 4.2 \mu\text{m}$ and $\sigma_y = 3.8 \mu\text{m}$.

5.2.3 Point-Spread Function

The measurements presented here were performed to determine the PSF of the system. Therefore, the relation between known pinhole diameter and measured image size has to be investigated. An image size threshold for small pinholes indicates the PSF of the optical system.

Judging by Fig. 5.19, the system seems to have the potential of a point-spread function with an RMS size lower than $3.4 - 3.8 \mu\text{m}$, since the dependence on pinhole size still behaves linearly all the way down to $5 \mu\text{m}$ pinhole diameter. The fit on this data indicates a PSF slightly below $3 \mu\text{m}$, but presently it can only be stated with certainty that the RMS PSF value is less than $3.4 - 3.8 \mu\text{m}$. If available one would have of course used a pinhole with considerably smaller diameter to see the actual PSF. Further one could consider

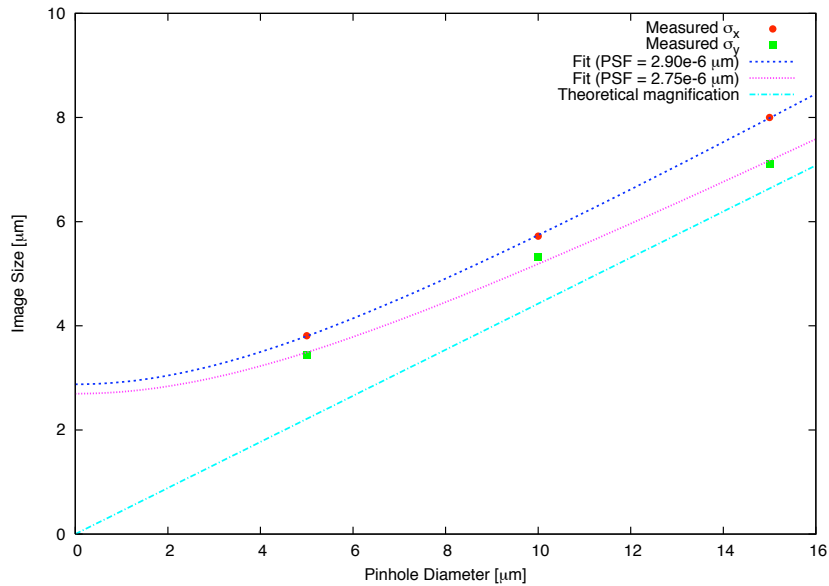


Figure 5.19: Measured image size vs. pinhole diameter. A rough fit is indicated giving a PSF of $2.9 \mu\text{m}$ respectively $2.75 \mu\text{m}$; both fit results have $\approx 10\%$ error.

using a bandpass filter around 540 nm in front of the pinhole, since the phosphor screen installed at the gun test stand is P43, which emits roughly 80% in a narrow band (12 nm FWHM) around 540 nm . With such a filter it is however expected that sufficient light intensity becomes a problem due to both a smaller pinhole and narrower bandwidth.

On the other hand one cannot expect a strong decrease in the PSF, since the diffraction pattern (Airy pattern) alone will give a limit $2.9 \mu\text{m}$ at 540 nm and 42 mrad opening angle.

Finally, a remaining issue is the unexpected behavior where results in vertical direction are systematically smaller than in horizontal direction. During the measurements it was attempted to exclude the possibility of a CCD deficiency (by rotating the camera by 90°) as well as the possibility of a pinhole deficiency (by rotating the pinhole by 90°). The results however did not change, and the question remains open.

5.3 Startup & First Operation

After the calibration measurements had been completed, the test stand and its subsystems were assembled and all connections to the control system made. After a pumpdown and successful leak test, a first bakeout of the entire test stand vacuum section was performed. At this point first operation became possible. The startup strategy was to use thermionic emission from a single tip emitter to clean the anode surface, commission the HV, insert a FEA and condition the FEA for further operation and performance analysis. The startup and first operation experience will be presented in this section. Finally examples of HV breakdown and subsequent FEA damage will be reported.

5.3.1 Assembly and Initial Pumpdown

Most of the test stand vacuum chamber and subsystem assembly proceeded as expected. Slight modifications to a few parts had to be made at PSI. It was discovered that the ceramic break length exceeded tolerances slightly. In-situ measurements of the accelerating gap length revealed that the gap was 1 – 3 mm longer than originally specified. Since this distance is crucial for the beam dynamics a correction of this error is necessary. It was decided that the correction would be applied by the 3D mover motor system (see Section 3.5) that was being designed at the time.

First tests after assembly showed that the weld seam between the YAG screen monitor bellow and the vacuum window was leaking. The weld seam was redone in house and the leak temporarily fixed. After subsequent bakeouts the seam failed again and it was decided to order and install a new bellow. The replacement has not had any leak issues.

After the first bakeout, a second leak was discovered in the SMA feedthrough of the cathode cone assembly. The feedthrough was part of a custom piece holding an SMA, BNC and multi-pin feedthrough welded onto a stainless

steel vacuum chamber closure. Further investigations revealed that the electron beam welding of the feedthroughs into this piece caused thermal stress which damaged the vacuum seal inside the SMA connection. It was decided to change the entire cathode cone design and move the feedthroughs to the cathode end flange where they would be installed on a standard DN 16 or DN 40 flange. This did not require any welding close to the delicate feedthroughs; however it came at the expense of having the possibility to use multiple different feedthrough types. Different feedthroughs were ordered and installed, but a change of feedthrough type now requires the chamber to be vented.

Once the leak problems had been solved and the cathode cone redesigned, manufactured and installed, a pumpdown and bakeout were successful: Pressure levels as low as $7 \cdot 10^{-10}$ mbar were reached in the vacuum chamber.

5.3.2 Single Tip Conditioning

Since the FEA is very sensitive to ion back-bombardment it was decided to use an alternative emission source and perform an electron bombardment of the anode surface to remove any surface impurities in the vicinity of the iris that would later be removed and ionized by the FEA electron beam.

It was decided to use a ZrC single-tip emitter as a thermionic electron source. The single-tip emitter is installed in a *Vogel-type* mount where the actual ZrC emitter is held in place by two molybdenum clamps. Both clamps are connected to leads on the back side of the mounting. If a current is applied to these leads, Joule-heating of the ZrC single-tip leads to DC thermionic emission. At the test stand the single-tip emitter was mounted to the end of the cathode cone (where otherwise the FEA holder would be) and the cathode electrode removed. The leads for the heating current were connected to a BNC feedthrough at the end of the cathode cone. The single-tip assembly before insertion is shown in Fig. 5.20.



Figure 5.20: Photo of the ZrC single-tip thermionic emitter used for electron bombardment of the anode. The ZrC tip can be seen at the top clamped between two molybdenum holders. The leads connect the molybdenum holders to the BNC feedthrough at the end of the cathode cone.

In a first setup, the cathode was put on a negative DC bias voltage and the anode was grounded. A lab power supply was used to supply a heating current on cathode potential. The current flowing from ground to the floating cathode (emission current) was measured as a function of the heating current. An example for such a measurement is shown in Fig. 5.21.

The setup was then changed by grounding the cathode and applying a positive voltage bias to the anode. The results for emission current measured on the cathode side and collected current measured on the anode were identical indicating that the anode was collecting the entire emitted current. The Faraday cup was inserted but no collected current was measured. Positively biasing the Faraday cup or applying solenoid current did not increase collected current to detectable levels. As expected, with such low electrostatic focusing only very few electrons pass the iris.

An increase of emitted current was observed after prolonged periods of emission at a certain heating current level: After a heating current was set, the collected current increased and approached an equilibrium value within sev-

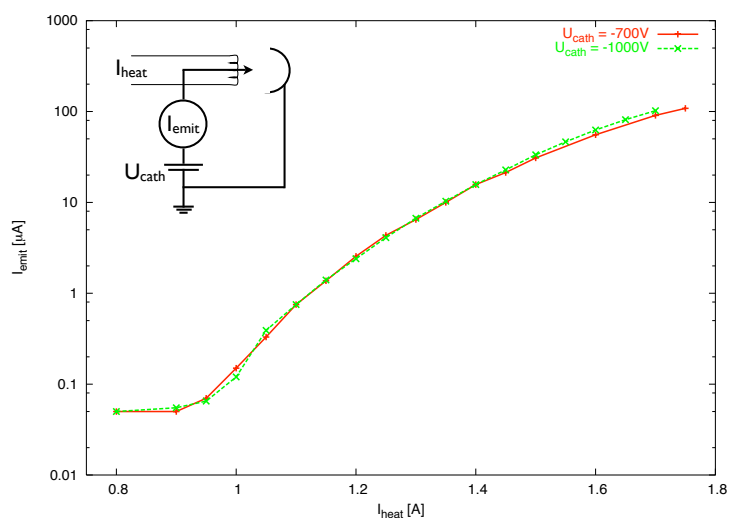


Figure 5.21: Thermionic emission current as a function of heating current. A bias voltage of -700 V or -1 kV was applied to the cathode; the anode was grounded. A schematic of the experimental setup is given.

eral hours. After 24 h no further increase of emission current was observed over a period of 2 weeks.

Once emission has reached the equilibrium level for a certain heating current setting, the heating current was stepped up to the next level and the conditioning process was observed again. This process was repeated for several different heating current levels as shown in Fig. 5.22. After the collected current level had stabilized for a certain heating current level, the collection was measured as a function of heating currents. The heating current was then set to the next higher level and the process repeated. A clear increase of emitted current due to conditioning of the single-tip emitter was observed.

After setting a higher heating current level the pressure inside the chamber increased and reached a maximum within a few hours. After this maximum a decay towards a lower equilibrium value could be observed indicating an actual conditioning of the gun. A decrease of this equilibrium value by going to higher heating current levels could not be observed indicating that a more intense bombardment did not increase conditioning.

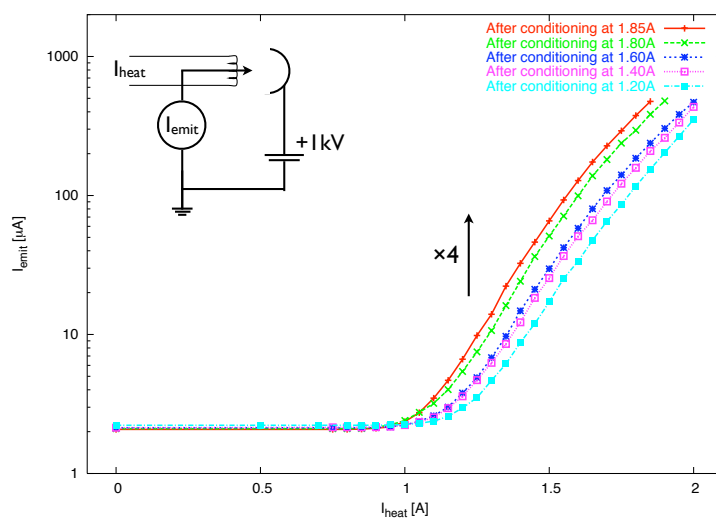


Figure 5.22: Increased thermionic emission due to conditioning: Thermionic emission current as a function of heating current. Each data set was taken after a certain heating current had been set and emission current stabilized for that setting. A bias voltage of +1 kV was applied to the anode; the cathode was grounded. An increase of emission current by a factor four was observed after conditioning. A schematic of the experimental setup is given.

By increasing the bias voltage the electrons are accelerated to higher energies which increases their penetration depth on the anode. However, going from -700 V to -1 kV bias voltage did not show any conditioning improvement. At this point it was therefore assumed maximum conditioning had been reached with this single-tip setup.

5.3.3 HV Commissioning

The HV power supply displays the amount of current fed to the output in order to maintain the set voltage. The displayed current is a time-averaged value with a precision of $\pm 0.5 \mu\text{A}$. During HV conditioning a constant non-zero current value was used to identify leak current.

In a first step, the HV power supply was attached to the bare hotdeck and the voltage was ramped from 0 V to -100 kV in steps of 5 kV. The maximum

HV level was reached and no leak currents were observed indicating that the cabling and isolation were sufficient. In a next step, the hotdeck was connected to the cathode flange through the signal cable from the pulser output to an SMA feedthrough on the cathode cone end flange. This setup allowed HV to be applied to the entire cathode assembly without pulsing the FEA.

The BNC feedthrough connection to the anode was connected to ground with a $1\text{ M}\Omega$ resistor and the voltage drop over the resistor measured in order to determine the level of current flowing to the anode (dark current, arcs). A simple voltmeter allowed measurement of anode currents as low as 1 nA . Subsequently, measurements were compared with a directly connected pico-ammeter and revealed that the voltmeter gave proper results.

During these first tests the cathode electrode and FEA were not installed which enlarged the diode gap by roughly 1 cm . The HV was stepped up in 1 kV increments. Above 50 kV leak current levels and the pressure level in the chamber increased. None of the leaked current was measured on the anode however. Further investigation revealed that parts of the cathode cone had rough weld seams that triggered parasitic field emission to the grounded ceramic break flange on the anode side. The weld seams of the cathode cone were smoothed out.

After reassembly, no leak currents from the cathode or to the anode were observed up to roughly 70 kV . Up to 80 kV an increase of leak current to the cathode to $10\text{ }\mu\text{A}$ was observed. At 97 kV the leak current to the cathode had reached $98\text{ }\mu\text{A}$. The leak currents were not detected on the anode indicating that they were flowing to ground. However, the pressure level in the chamber remained constant, indicating that the current leak was not inside the vacuum chamber.

Finally, the smell of ozone in the bunker hinted at corona discharge which was then observed with a CCD camera in the darkened bunker. The weld seams between the break flanges and the ceramic structure had sharp edges;

those on the cathode side lit up on the screen above 80 kV due to corona discharge. In a first attempt to prevent these discharges, the sharpest edges of the weld seams were sanded off. This reduced the amount of leaked current but leaks on the order of several μA were still measured. It was then decided to use aluminum tape to seal off the weld seams. This prevented the corona discharges and allowed the HV to be stepped up to 100 kV with no measurable leak currents.

At this point it was decided to install the cathode electrode and the first FEA. Without pulsing the FEA, voltages as high as 80 kV were achieved and maintained stably. Above 80 kV the pressure inside the chamber increased and showed spikes; leak currents to the anode appeared and increased with the HV. It is assumed that due to a slight misalignment of the cathode with respect to the anode (see Section 5.3.5), peak fields are higher than anticipated, thus triggering parasitic emission from the FEA to the anode. A definitive answer will be given once the 3D mover motor system has been installed and misalignment corrected.

It has also been observed that the maximum attainable HV without leak currents is reduced to roughly 35 kV when the FEA is removed but the cathode electrode remains installed. This is explained either by HV field extending into the cathode iris and triggering parasitic emission from the FEA holder or by parasitic emission from the cathode iris edge which is exposed when no FEA is installed behind.

5.3.4 Conditioning the FEA

Conditioning with Long Pulses and Low Voltage

FEA conditioning was performed according to the guidelines published by the manufacturer [42]. In a first step the FEA was pulsed with a low voltage pulser capable of producing pulses of 5 ms pulse length. Since this device could not be floated on HV potential, a positive accelerating voltage of 800 V

was applied to the anode; the Faraday cup was biased at +1 kV. The pulse repetition rate was chosen at 10 Hz. Higher duty cycles (either longer pulse lengths or higher pulse repetition rates) showed an increase of vacuum pressure in the chamber and were thus avoided during the early conditioning phase.

The current collected on the anode and Faraday cup was measured with an oscilloscope giving the voltage drop over a 1 M Ω resistor between the anode (respectively Faraday cup) and ground. At a gate voltage of 59 V first emission current of roughly 200 nA was detected on the anode. The emission was rather unstable, some gate pulses did not trigger emission at all, and emission current levels showed fluctuations of up to 100%. After a few minutes, emission started to stabilize while the emitted current increased (removal of surface contaminants, tip shaping). After 45 min the emission current had stabilized at 300 nA with a constant pulse shape: 2 ms rise time, approximately 3 ms flat top, 2.5 ms fall time. The gate voltage was then slightly increased and the conditioning process repeated. The conditioning process of the first SRI cathode installed at the test stand is shown in Fig. 5.23: the increase of emission current at constant gate voltages with time is clearly seen. An increase of current collected on the anode by an order of magnitude was observed during one night of conditioning with $U_{\text{gate}} = 64.5$ V, $\tau = 5$ ms, 10 Hz. After conditioning, the gate voltage was reduced and emission current measured again: increased collected current values indicated a sustainable effect of conditioning on the emission characteristics of the FEA.

After a full night of conditioning the first Faraday cup collected current was measured at 0.8 μ A. A ratio of 30 between the anode and Faraday cup collected current indicates a strongly unfocused beam which is explained by the low accelerating voltage. It was however possible to increase Faraday cup collection by 100% by applying 0.2 A of solenoid current corresponding to 11.6 mT of longitudinal magnetic field. This indicates that a potential difference of 200 V between anode and Faraday cup is insufficient to collect all electrons that pass the anode iris. Due to the Faraday cup BNC connection higher bias voltages could however not be applied.

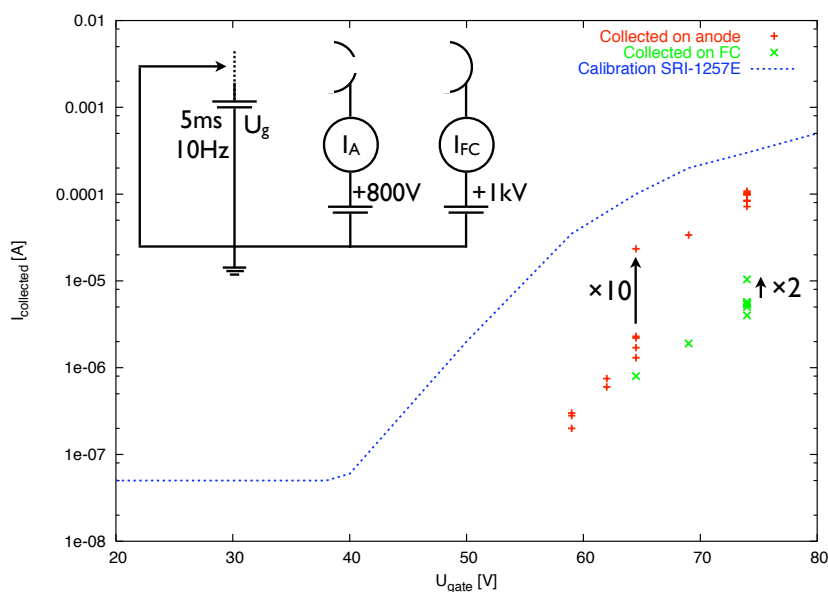


Figure 5.23: FEA conditioning with long pulses: Collected current as a function of gate voltage. A bias voltage of +800 V is applied to the cathode, +1 kV is applied to the Faraday cup. The manufacturer’s calibration is included for comparison. A schematic of the experimental setup is given.

Furthermore it was observed that regardless of the conditioning time, the manufacturer’s calibration values could not be reproduced as indicated in Fig. 5.23. The manufacturer did not specify the pulse length used for calibration and it is assumed that this difference can be explained by the use of shorter pulse lengths here where rise and fall times are comparable to the flat top portion of the pulse.

Conditioning with Short Pulses and High Voltage

For gate voltages above 74 V an increase in pressure and sustained unstable emission was observed. It was decided to switch the conditioning setup to use the test stand pulser and HV supply which would allow lower duty cycle and higher accelerating voltage. The test stand pulser was set to its maximum pulse length of 100 ns with a repetition rate of 10 Hz. The cathode was

put on a HV bias of -4.5 kV.³ For the very short pulse lengths applied by the test stand pulser, the anode signal could no longer be used due to the impedance of the unshielded signal cable between the BNC feedthrough and the anode structure: When trying to measure anode signals with the fast oscilloscope, only a ring was measured for the duration of the pulse length with a frequency of 23.5 MHz corresponding to the roughly 13 m signal cable length (this ring can be seen in Fig. 6.5). At the increased accelerating voltage the beam focusing was increased and a much larger portion of the beam passes the anode iris and reaches the Faraday cup. Therefore only the Faraday cup collection signal is used to determine absolute current values.

In a first measurement, the current collected on the Faraday cup was determined as a function of the gate voltage. The detection limit is roughly $20 \mu\text{A}$ given by the scope resolution of 1 mV and the 50Ω termination. Faraday cup current was first detected above 100 V gate voltage and quickly increased to 0.8 mA at 172 V. At this level emission became very unstable; it was decided to set the gate voltage at 160 V and observe if conditioning and stabilization of the emission could be observed. After a full night of conditioning at 160 V the emission current had stabilized and a second calibration was performed. Although emission current had not significantly increased, it was now possible to increase the gate voltage up to 220 V without encountering unstable emission. The conditioning process was repeated at 220 V revealing stable emission for all gate voltages up to 220 V and an increased emission level compared to earlier runs; this is shown in Fig. 5.24.

For gate voltages between 170 V and 220 V no increase of emission current was observed. This is explained by the space charge limitation at the cathode for the low accelerating voltage applied. At low accelerating voltage the emitted charge screens the FEA from the external electric field thus reducing the effective emission (Child's law). This leads to an equilibrium emission current level is only substantially increased by increasing the external accelerating voltage [71].

³There was no scientific reason for this voltage, but before operation clearance from radiation safety had been granted, 5 kV was the maximum allowed accelerating voltage.

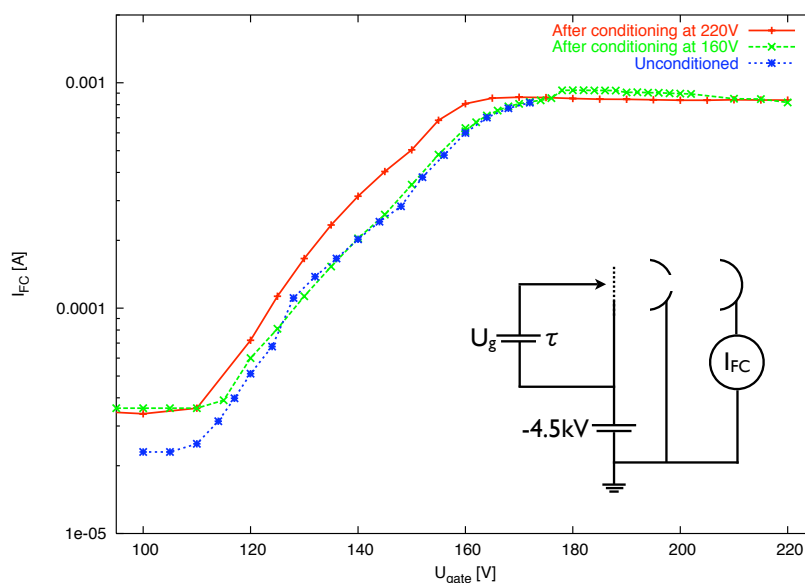


Figure 5.24: FEA conditioning with short pulses: Current collected on the Faraday cup as a function of gate voltage. A bias voltage of -4.5 kV was applied to the cathode. The pulser pulsed the gate with 100 ns pulses at 10 Hz. A schematic of the experimental setup is given.

In a later phase it was discovered that the resulting emission characteristics of an FEA depended entirely on the conditioning performed with short pulses regardless of the long pulse conditioning process. Obviously the conditioning performed with very low duty cycle but at increased accelerating voltage was a more efficient conditioning process.

5.3.5 Breakdown and FEA Destruction

In order to further increase the emission from the FEA the final commissioning step was to increase the accelerating HV. The combined effect of large accelerating voltage and high gate voltages led to several HV breakdowns. HV arcs can damage and destroy FEAs; two examples are given here.

Ion Back-Bombardment at High Accelerating Voltage

During operation of the first FEA (SRI-1257E) the accelerating HV was increased up to 50 kV. At this level, the emission saturated at roughly 30 mA current for gate voltages above 230 V. In an attempt to further increase the emitted current, the HV was gradually increased. At a HV setting of 82 kV a severe arc caused an immediate pressure increase by two orders of magnitude; from there on a leak current (collected on the anode) appeared for HV settings above 25 kV. No emission from the FEA could be detected regardless of the applied gate voltage. The ohmic resistance measured between the tips and the gate layer was 48 k Ω indicating that the FEA had been bridged and therefore destroyed.

The chamber was vented for inspection and replacement of the FEA. Surprisingly the damage was visible by eye: The anode gold plating had chipped off around the iris and the FEA showed signs of ion back-bombardment (Fig. 5.25).

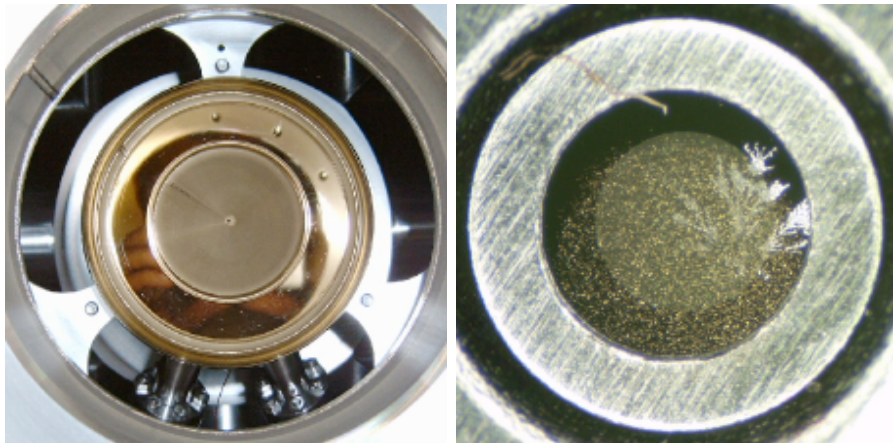


Figure 5.25: Photos of FEA and anode iris damage. The left image shows how the gold plating surrounding the anode iris chipped off. The image on the right side shows gold sputters on the FEA: The gold removed around the iris was ionized and back-bombarded onto the FEA. The cracks in the gate layer (white) were caused by thermal stress due to the HV arc at 82 kV.

As seen with an SEM, the arc experienced at 82 kV damaged the FEA severely leaving behind a hole in the gate layer and a crater in the substrate. At the edges of this crater parasitic field emission caused the high levels of leak current observed. The damage by the arc also bridged the FEA leading to the finite resistance between tips and gate layer. An example of FEA damage due to a HV arc is given in Fig. 5.26.

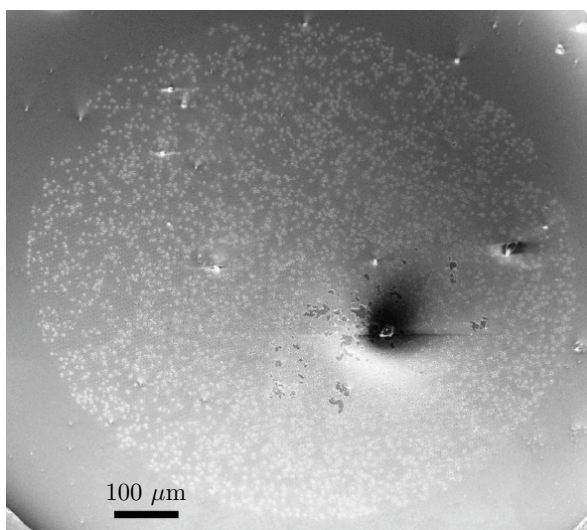


Figure 5.26: SEM picture of an FEA (SRI-1257D) destroyed by HV breakdown. At the location of the arc the gate layer and tip substrate was removed leaving behind a crater. Beside the arc damage which destroyed the FEA many exploded tips can be seen. Roughly 10% of the tips explode during normal operation. As a consequence a slightly increased gate voltage is required to reach a certain emission current.

The damage to the anode iris reveals that parts of the beam had been scraped by the anode iris. Obviously the energy deposited by scraped beam particles was sufficient to damage the surface due to the interface between the copper anode structure and the gold plating. The gold removed from the anode iris was ionized and back-bombarded onto the cathode; the gold sputters are clearly visible in Fig. 5.25. In addition cracks in the gate layer due to thermal stress can be seen; this is a consequence of the HV arc.

It is interesting to note that the anode iris damage and the gold sputters on the cathode clearly show an asymmetry. It is believed that this asymmetry indicates a transverse misalignment of the cathode with respect to the anode on the order of 0.5 mm. After installation of the 3D mover motor system, it will become possible to correct such a misalignment.

As a consequence of this incident both gold plated electrodes were removed and replaced by electrodes made from pure 316L stainless steel. A new FEA was inserted, the chamber pumped down and a bakeout performed.

Instabilities at High Gate Voltage Leading to Breakdown

The second FEA (SRI-1257D) was conditioned with long pulses at low voltage and with short pulses at high voltage. At 4.5 kV the FEA was conditioned up to a gate voltage of 265 V. Above 265 V strong instabilities of the emitted current were observed together with sudden bursts in the collection signal. The pressure in the chamber remained fairly constant below 250 V, but showed instabilities and a strong increase above 250 V. Finally at 290 V a HV arc was triggered and the chamber pressure increased by two orders of magnitude. This is shown in Fig. 5.27.

An explanation for the emission bursts and pressure rise is emission from tips to gate layer. This caused a local vacuum degradation which then triggered HV breakdown. The arc damaged the FEA and introduced a finite tip-gate resistance of $\approx 100 \text{ k}\Omega$, but a small amount of emission could still be triggered from the FEA at gate voltages in excess of 200 V. At 295 V the second breakdown occurred. A final breakdown was triggered at 260 V which completely destroyed the FEA.

The reason for emission from the tips to the gate layer is uncertain although surface contamination is a likely cause. It was decided for the operation of future FEAs to stop gate voltage increase when emission bursts were observed in order to prevent vacuum degradation leading to HV breakdown and thus to FEA damage.

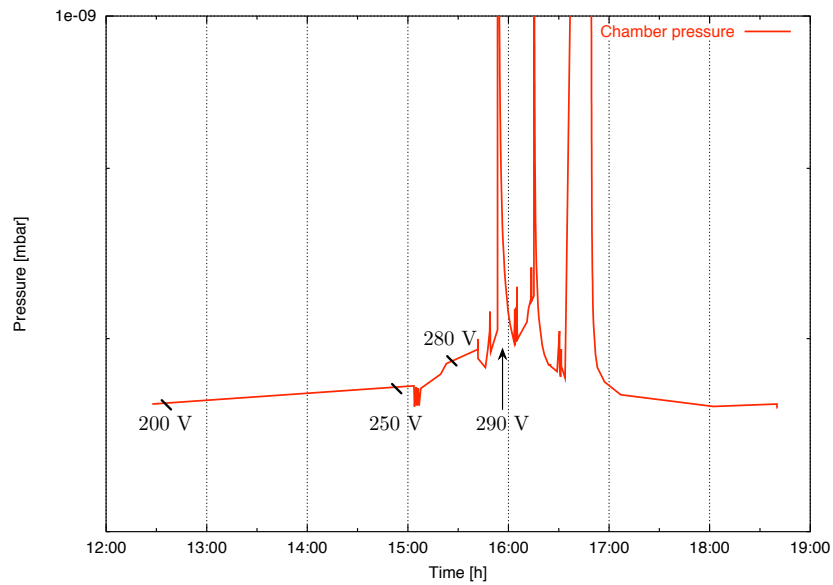


Figure 5.27: Destruction of FEA SRI-1257D: The pressure in the vacuum chamber is plotted as a function of time. For gate voltages below 250 V vacuum pressure remained stable at $7.6 \cdot 10^{-10}$ mbar. Above 250 V the pressure increased due to emission from tips to gate layer. The local vacuum degradation triggered the HV breakdown observed at 290 V. Two subsequent breakdown events are also shown.

Chapter 6

Experimental Results

Once an FEA has been successfully installed, good UHV conditions are achieved and stable HV is applied, measurements of the FEA can be performed. This chapter presents these measurements.

- The first section describes FEA performance calibration and investigates longitudinal phase space properties of emitted bunches.
- The second section investigates the transverse beam profile and the influence of solenoid focusing or bunch charge variation.
- The following section presents emittance measurements and reconstruction of the transverse phase space distribution of bunches emitted by the FEA and accelerated in the test stand. Influence of bunch charge and HV (breakdown) on emittance are investigated.
- Finally, details of the emission process are deduced from emittance measurements and a comparison between measured transverse bunch properties and simulations is given.

6.1 FEA Performance Calibration

Investigation of the longitudinal phase space distribution of bunches emitted from an FEA is limited to measurements of the charge-time structure at the test stand. The energy is given by the accelerating voltage, but the energy spread within the bunch cannot be measured. Energy spread measurements would require a spectrometer-like setup. It has been considered to put the Faraday cup on negative HV and to measure the consequent collection reduction to approximate the energy distribution in the bunch, but due to the design of the Faraday cup this is not feasible.

The longitudinal measurements make use of fast measurement of the Faraday cup collected current and derive bunch charge by integrating the current-time distribution. The 2 GHz - 20 GS/s oscilloscope is used to analyze the Faraday cup signal. An example is given in Fig. 6.1.

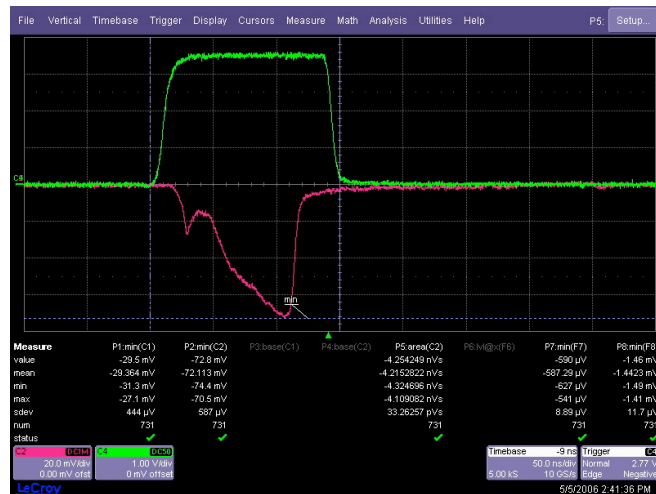


Figure 6.1: The current collected on the Faraday cup as seen with the fast oscilloscope for SRI-1257B. The 100 ns gate pulse (green line) triggers the scope. The red line shows the current collected on the Faraday cup. Integration of this current reveals the bunch charge. In this example an accelerating voltage of 40 kV and a gate voltage of 195 V were chosen. The measured peak current is 1.46 mA and the charge within the bunch is 85 pC.

The long rise time of the FEA emitted current pulse is due to the RC constant of the FEA (see Section 6.1.3). The overshoot of the emitted current in the rising flank is likely caused by a voltage overshoot at the FEA. When the entire electric circuit was modeled it was noticed that a bulk resistance of the silicon substrate below $\approx 100 \Omega$ can lead to an overshoot of the voltage between the tips and the gate layer.

In the measurements presented in this section, the accelerating voltage was limited to 40 kV to reduce the risk of HV breakdown triggered by emission from tips to gate (see Section 5.3.5). This has implications for the beam dynamics and will be discussed when analyzing transverse measurements. For longitudinal measurements it is important to note that emission from the cathode is governed primarily by the gate voltage while the external accelerating voltage determines the space charge limit at the cathode (see Section 6.1.2).

6.1.1 Gate Voltage Influence

The main influence on emission current and bunch charge is the gate voltage setting. Each FEA is calibrated to reveal current and charge dependence on gate voltage for a certain accelerating HV. An example for the calibration of SRI-1257B is given in Fig. 6.2; the external accelerating HV is set at 40 kV, the pulser delivers 100 ns pulses to the FEA at 100 Hz. For the charge and current data the scope resolution threshold is subtracted and the standard deviation of several hundred shots defines the measurement error.

The strong dependence of emission current on gate voltage as predicted by the Fowler-Nordheim law (2.72) is shown. Gate voltages were not increased beyond 195 V due to strong emission fluctuations to protect the FEA. Saturation of cathode emission was not observed at these gate voltages.

For identical accelerating voltage, the calibration is reproducible within a few percent for each FEA over prolonged periods of time. Exceptions are deterioration of performance due to damage through HV arcs. However, the

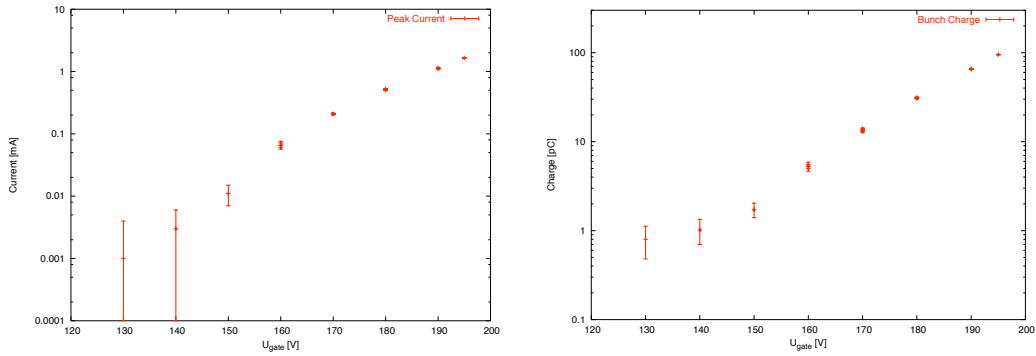


Figure 6.2: Calibration of emitted peak current and bunch charge for SRI-1257B at 40 kV accelerating voltage. For the calibration the pulser was set to deliver 100 ns pulses to the FEA at 100 Hz.

calibration varies from one FEA to another even if the FEAs are from within the same manufacturing batch. This is shown in Fig. 6.3.

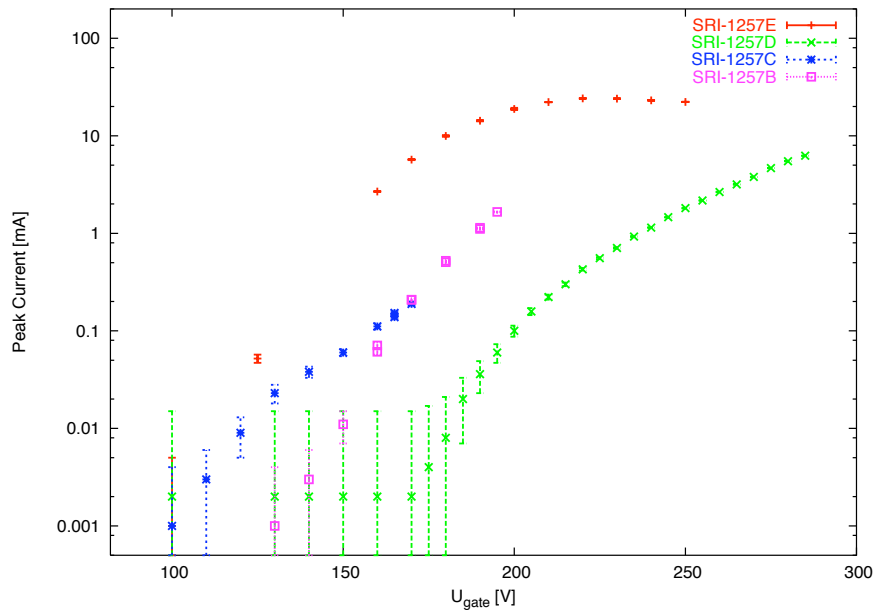


Figure 6.3: Calibration of different FEAs from the same manufacturing batch. The peak current was measured as a function of gate voltage at 40 kV accelerating voltage with 100 ns pulses at 10 Hz.

All FEAs shown here are from the same SRI-1257 batch. While 1257E could be driven into full saturation, the rest of the batch remained below saturation. Strong instabilities above 170 V gate voltage prevented running 1257C to 1 mA.

6.1.2 HV Influence

The applied external accelerating HV has a strong influence on the beam dynamics in the gun; it defines the electrostatic focusing of the diode and limits the maximum extractable charge due to space charge screening of the emitter. Figure 6.4 is an example of the FEA performance variation due to different accelerating HV. While emission at low gate voltages remains similar, the current level for which saturation occurs changes by as much as a factor 5. The most significant difference in saturation level is found below 40 kV.

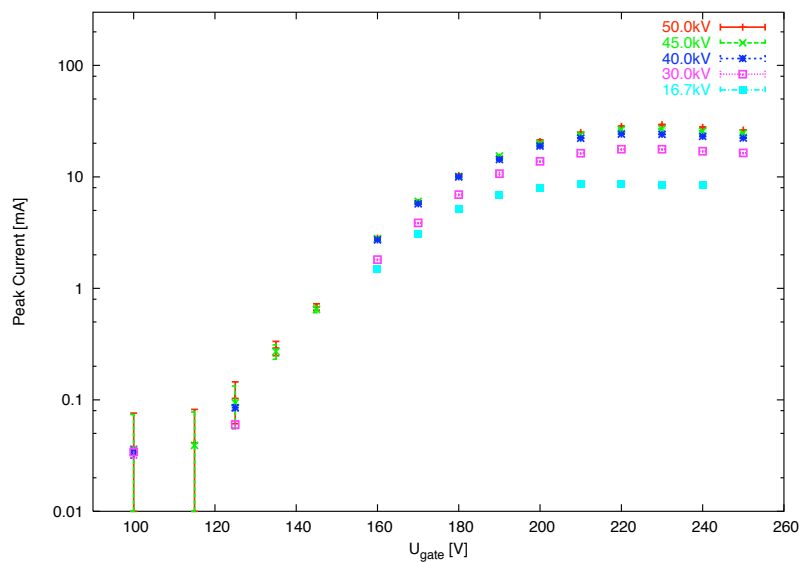


Figure 6.4: FEA calibration for SRI-1257E compared for different external accelerating HV. The main difference is the current level at which emission saturates.

At very low external accelerating voltage the lack of electrostatic focusing leads to scraping of the unfocused beam on the anode iris. This is clearly seen in Fig. 6.5 where oscilloscope images for 5 kV and 50 kV collection are displayed; the applied gate voltage was 200 V in both cases. At 50 kV the anode signal shows a ring caused by the lack of shielding on the signal line (see Section 5.3.4); integration of this ring reveals no collected current. At 5 kV the ring on the anode signal is still visible, but it clearly follows the pulse shape seen on the Faraday cup signal. The integration of the anode signal reveals roughly 1 mA of peak current collected on the anode due to beam scraping at the anode iris.

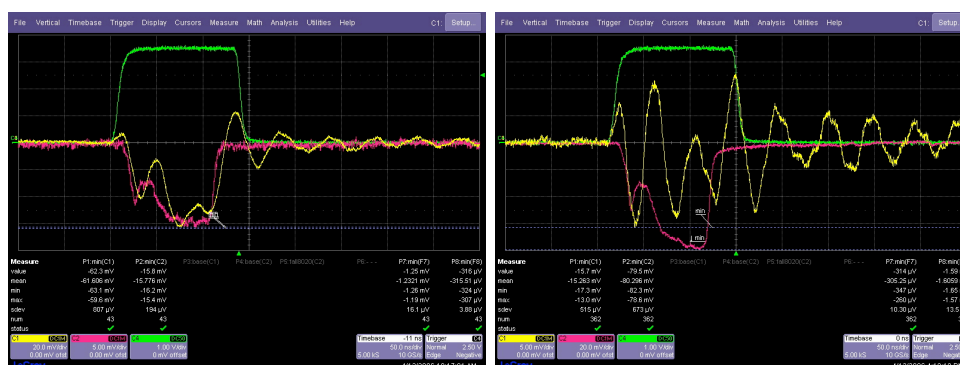


Figure 6.5: Current collected on the anode (yellow line) and Faraday cup (red line) for 5 kV accelerating voltage (left) and 50 kV accelerating voltage (right) with SRI-1257C. The gate voltage was 200 V in both cases. The integrated anode signal reveals beam scraping on the anode iris at low accelerating voltage. The 100 ns gate pulse is indicated (green line).

Another demonstration of the effect is given in Fig 6.6 where the FEA calibration is shown for 4.5 kV and 40 kV together with the integrated anode current signal. For 40 kV the Faraday cup collection is enhanced while the amount of current scraped by the anode is reduced. The sum of Faraday cup collected current and anode collected current remains constant indicating that the reduced Faraday cup signal at low accelerating voltage is caused by beam scraping at the anode iris.

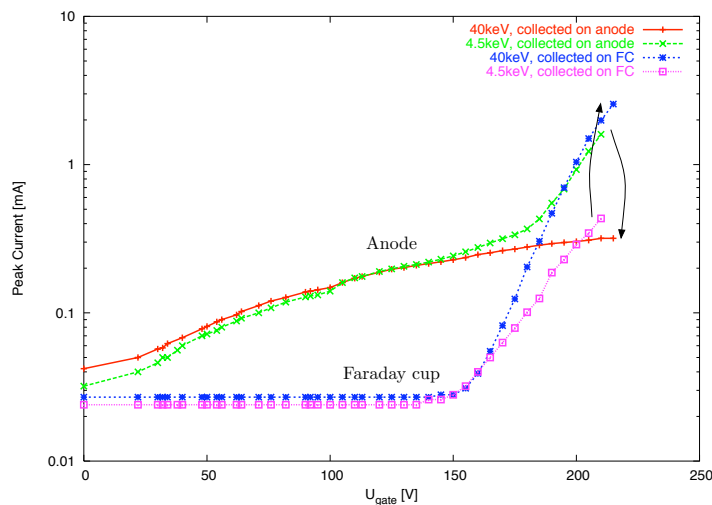


Figure 6.6: Current collected on the anode and Faraday cup for 4.5 kV and 40 kV accelerating voltage with SRI-1257C. When the accelerating voltage is increased the electrostatic focusing of the gun increases and beam scraping is reduced: the (integrated) anode signal decreases and the Faraday cup signal increases. The sum of both signals remains constant indicating that the increase of the Faraday cup signal is due to reduced beam scraping rather than increased emission.

In order to draw maximum current from the FEA it is desirable to maximize the accelerating HV. On the other hand HV breakdown and potentially harmful arcing is more likely to happen at high voltages. At 40 kV accelerating voltage, stable FEA operation was possible for all FEAs at gate voltages below the tip to gate emission threshold. At 50 kV and 60 kV arcs could be avoided by pulsing the FEA at reduced gate voltages. It was observed that a single tip to gate emission event was sufficient to deteriorate the local vacuum enough to trigger breakdown. Above 60 kV arcs can occur even while the FEA is not pulsed. It is assumed that the transverse misalignment between cathode and anode (see Section 5.3.5) further aggravates this problem preventing stable HV operation at the design parameter of 100 kV. Exchange of a destroyed FEA requires venting of the chamber, cathode cone disassembly, FEA exchange, reassembly, pumpdown and bakeout which all together causes a 5 – 10 day delay. It was therefore decided to perform FEA measure-

ments at 40 kV under stable conditions until installation of the 3D mover motor system and correction of the misalignment would allow increased HV operation.

6.1.3 Pulse Length Influence

In a final set of longitudinal measurements the influence of pulse length on emission was investigated. Previously, only assumptions for the RC constant of the FEA were available; the idea of the measurements was to deduce the constant from the emission current characteristics. Figure 6.7 shows a measurement of the current collected on the Faraday cup as a function of the pulse length applied by the pulser to the FEA gate. The measurement data suggests that above 20 ns the emitted peak current is independent of the applied gate pulse length.

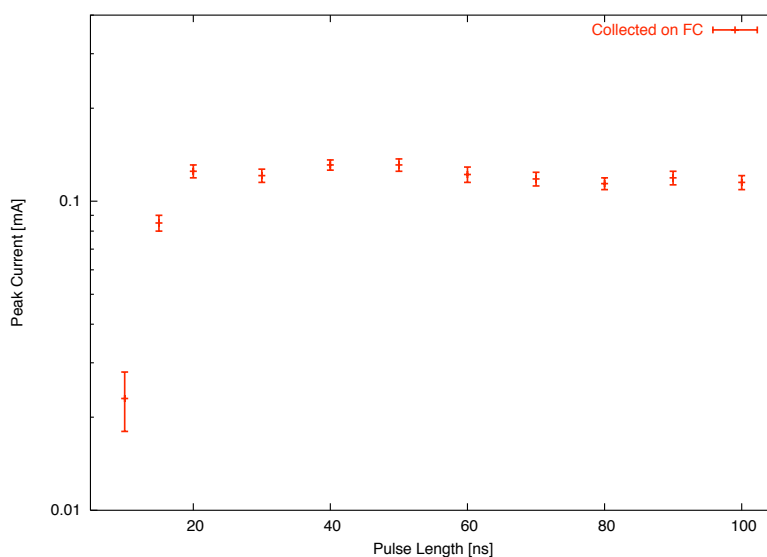


Figure 6.7: Peak current collected on the Faraday cup as a function of applied pulse length. The accelerating voltage was 40 kV, the applied gate voltage was 170 V. The data was taken with SRI-1257C. Above 20 ns the emission shows no dependence on pulse length.

The minimum required pulse length to reach maximum peak current depends strongly on the applied gate voltage as demonstrated in the measurements shown in Fig. 6.8. The higher the applied gate voltage, the less pulse length is required to reach the maximum peak current.

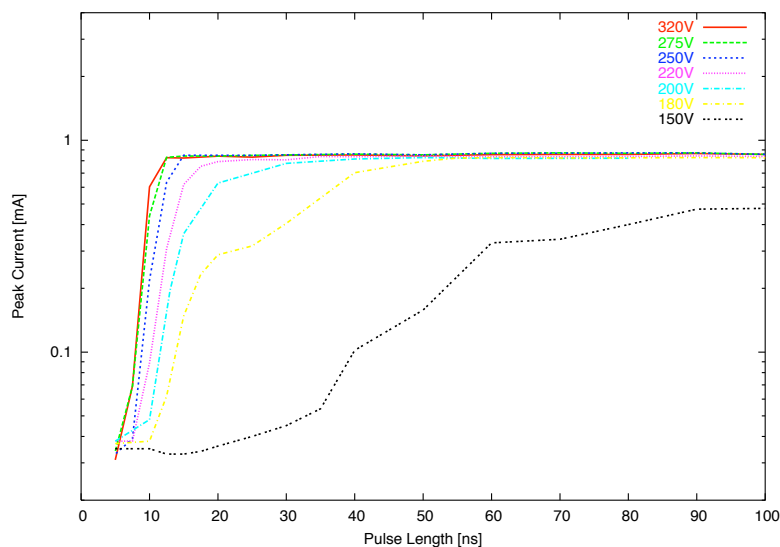


Figure 6.8: Peak current collected on the Faraday cup for different gate voltages. The accelerating voltage was 4.5 kV; the data was taken with SRI-1257E. At high gate voltages only a short pulse length is required to reach maximum peak current; at low gate voltages, a longer pulse length is required.

Further investigation showed that this behavior can be explained by the pulser characteristics. Close to the maximum pulser voltage of 320 V the pulse shape is nearly square with a short rise time and only slightly longer fall time. At voltages below 250 V the pulse shape quickly deteriorates and the rise times become very large.

The influence of the gate pulse rise time on the rise time of the collected current pulse is clearly visible in Fig. 6.9. The plot shows the minimum required pulse length to collect the maximum peak current as a function of the applied gate voltage. Below 230 V there is a linear relation indicating that

the gate pulse rise time determines the maximum emitted current. Above 230 V a nearly constant relation indicates that emission is determined by the RC constant of the FEA rather than the pulse characteristics of the gate pulser.

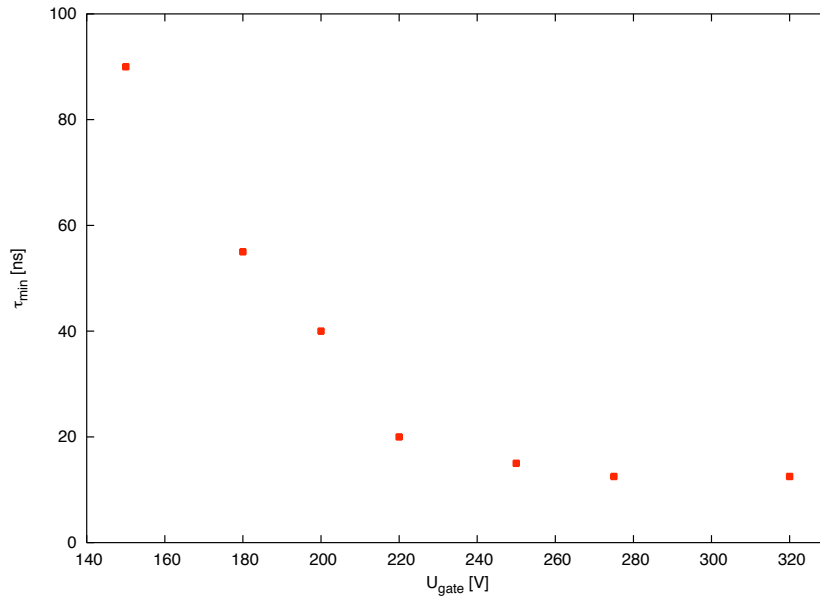


Figure 6.9: Minimum required pulse length to collect the maximum peak current. The data was acquired with SRI-1257E at 4.5 kV accelerating voltage. Below 230 V gate voltage emission is determined by the long rise time of the gate pulse. Above 230 V emission is determined by the RC constant of the FEA and therefore rise time is independent of the gate voltage.

For gate voltages above 230 V an minimum rise time of ≈ 10 ns is determined. If this time is attributed to the RC constant of the FEA, the bulk resistance of the substrate can be deduced. Assuming a capacitance between the tip substrate and the gate layer of 150 pF (see Section 2.6.3), this renders a bulk resistance of roughly 67 Ω . Such a bulk resistance is consistent with the voltage overshoot assumed responsible for the current spike in the rising flank of the emission pulse as proposed in Section 6.1.

For most measurements large bunch charge and high peak current is of greatest interest. Therefore, for most of the measurements the maximum pulse length of 100 ns was chosen. The pulser is capable of applying this pulse length without considerable rise and fall time contributions at all relevant gate voltages.

6.2 Investigation of Transverse Beam Profile

The transverse beam profile for different longitudinal positions z was measured with the phosphor screen monitor. The screen can be moved to positions between 237 mm¹ and 517 mm from the cathode surface. The zoom optics and CCD camera are moved independently but accordingly to keep the phosphor screen focused. The application CAM is then used to image the beam spot on the phosphor screen and to apply a Gaussian fit (although the radial particle distribution is parabolic at emission, the measured beam spot was usually best approximated by a Gaussian) to the beam profile returning σ_x and σ_y . An example is given in Fig. 6.10.

Due to the low bunch charge emitted by the SRI FEAs, the SNR of the phosphor screen monitor image is low. Even with strong solenoid focusing, a single shot can hardly be distinguished from the background. In the example shown in Fig. 6.10, 10 shots were integrated leading to a the background level of 11 and a maximum intensity of 187 (8 bit resolution).

Without solenoid focusing the beam envelope cannot be properly resolved due to bad SNR and large beam size. The screen monitor optics field of view width is 494 pixels or 16.2 mm. For a proper Gaussian fit of the profile, at least $5\sigma_{x,y}$ have to be imaged. This corresponds to a maximum $\sigma_{x,y}$ of roughly 3.2 mm that can be measured with the phosphor screen monitor.

¹The 237 mm position can only be reached if the slit mask inserts have been retracted. With masks inserted the minimum position of the phosphor screen is 257 mm.

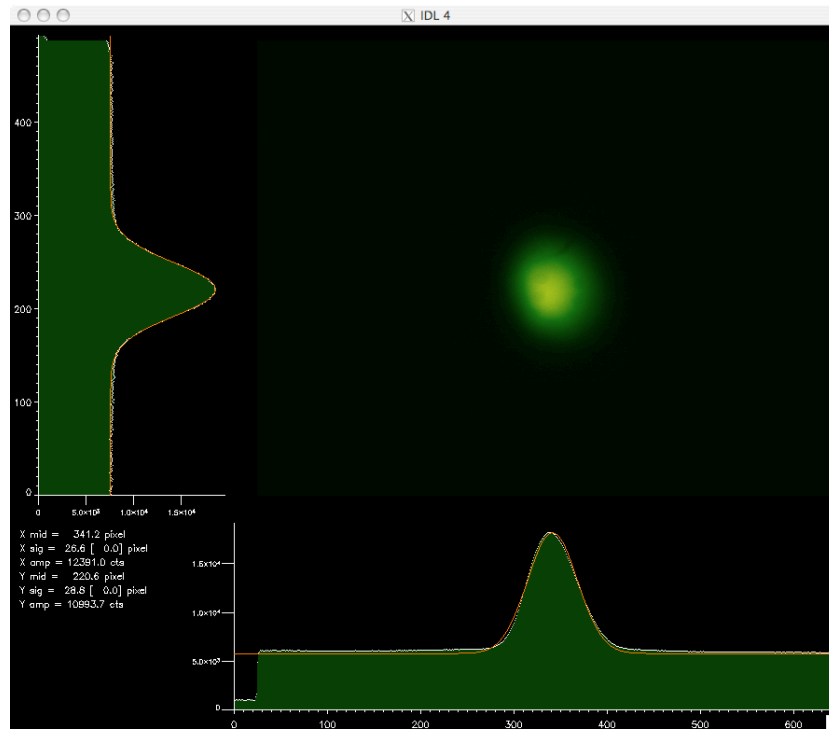


Figure 6.10: Transverse beam profile measured with the phosphor screen monitor for a 40 keV bunch with 1 mA peak current and 57 pC bunch charge from SRI-1257B. The image integrates over ten 100 ns shots. The phosphor screen was positioned 342 mm away from the cathode surface. The applied solenoid field was 51 mT. The measured beam size is $\sigma_x = 0.87$ mm, $\sigma_y = 0.94$ mm.

For large beam spots non-uniformities in the transverse beam profile can be observed. Unfortunately, due to the required solenoid focusing they cannot be directly mapped to emission characteristics of the FEA surface (point-to-point imaging of the source with the solenoid is not possible with the current FEA performance). It has been observed that “hot spots” appear after HV arcs; their location and intensity remain stable until the next HV arc occurrence. An example for non-uniformities of the transverse beam distribution is given in Fig. 6.11.

The beam size evolution in the diagnostics section was measured with the phosphor screen monitor as shown in Fig. 6.12. For constant energy, bunch

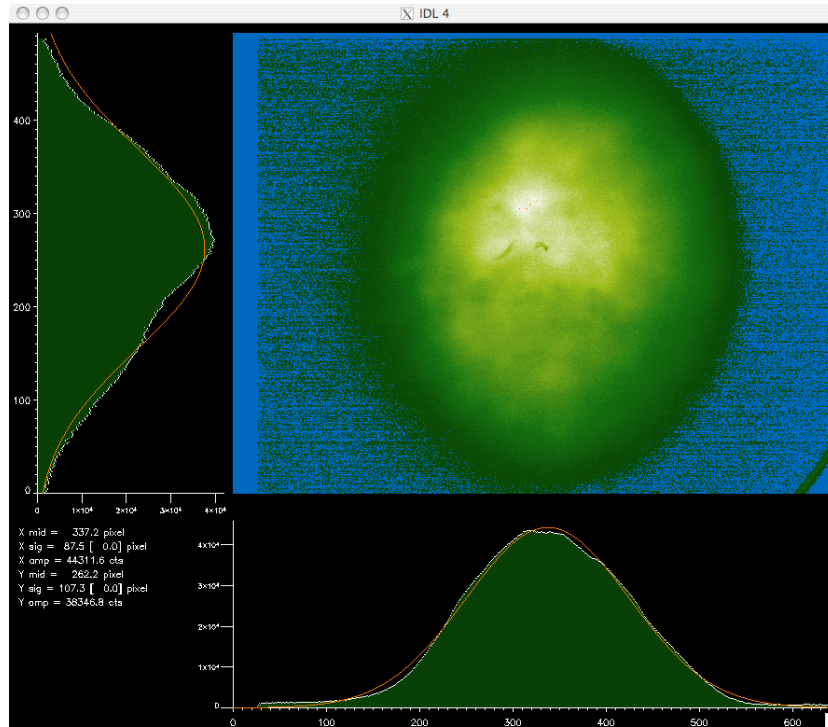


Figure 6.11: Example of non-uniformities in the beam profile of an unfocused beam. The image shows the integration of 10 shots of 40 keV bunches from SRI-1257B with a peak current of 1.1 mA and a bunch charge of 64 pC. Non-uniformities and hot spots are clearly seen. Blue pixels indicate intensities below the background level.

charge and solenoid current, the screen was moved through the drift and the beam size measured as shown above. The images integrated over 20 shots. The fluctuations of $\sigma_{x,y}$ give the measurement error.

The beam size in x and y is nearly equal; a difference is only measured at the end of the drift where the beam size is largest. The evolution of $\sigma_{x,y}^2$ shows a quadratic increase as is expected in a drift section downstream of a beam waist. The actual waist location cannot be measured because the minimum screen position is 237 mm. An attempt to determine the waist location and size from a quadratic fit of the data failed due to the large fitting error. A more detailed investigation of the beam waist following the solenoid will be given in Section 6.2.2.

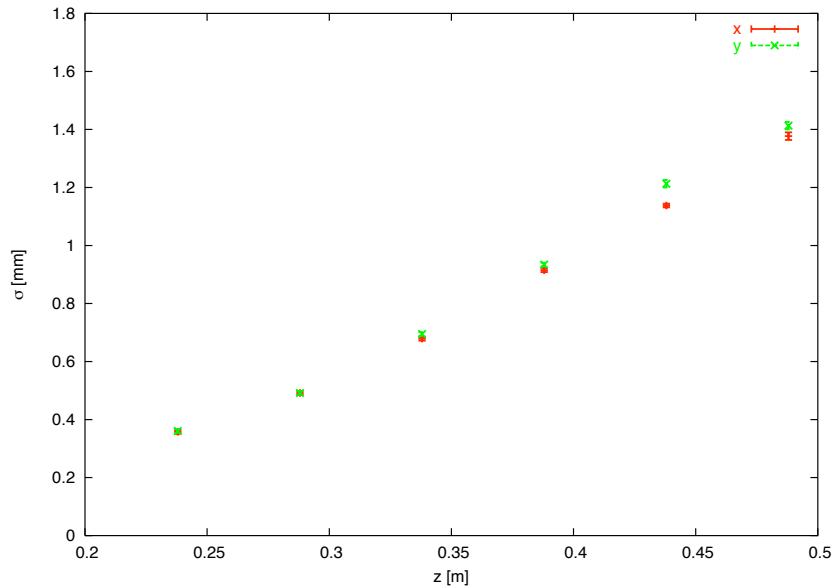


Figure 6.12: Beam size evolution in the diagnostics section. The measured 40 keV bunch from SRI-1257C had a peak current of 338 μA . The solenoid field applied was 51 mT. The data was taken from profile images integrated over 20 shots.

6.2.1 Transverse Beam Size as a Function of Bunch Charge

The influence of bunch charge on the beam size was investigated. A measurement with no solenoid focusing was not feasible because the completely unfocused beam spot could not be measured. Figure 6.13 shows the results of beam size measurements in the transverse horizontal direction for several solenoid settings.

For the weakest focusing strength, it appears the beam size increases slowly with the charge inserted into the bunch. This dependence is however not recognized for stronger focusing strengths (at low solenoid focusing strength the beam size is largest and hence the measurement errors become largest). The bunch charges achievable with the SRI FEAs are so low that the bunch is emittance dominated. Unlike a space charge dominated bunch where the

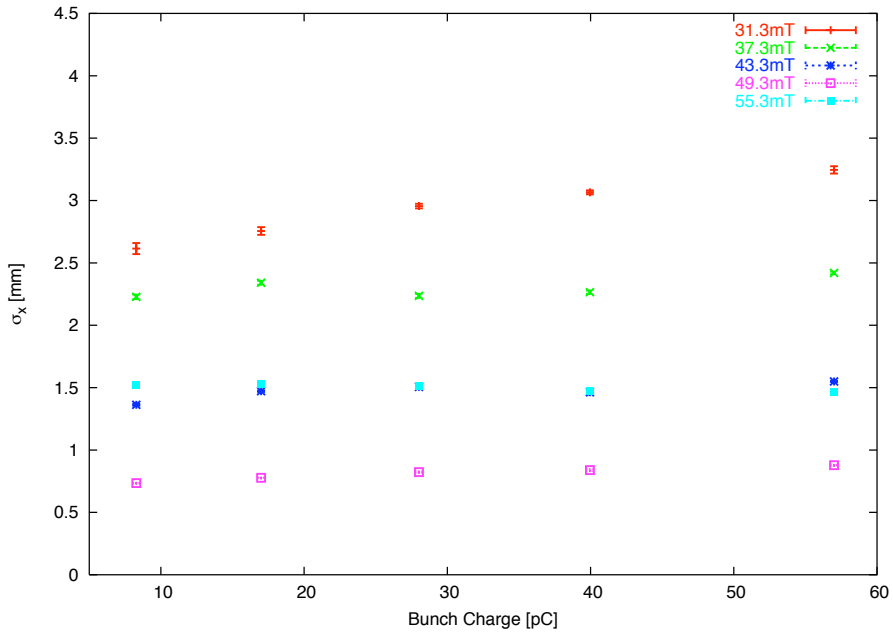


Figure 6.13: Beam size σ_x as a function of bunch charge for several solenoid focusing strengths. The beam energy was 40 keV. A pulse length of 100 ns was chosen. The beam size was measured with profile images integrating over 10 shots from SRI-1257B. The profiles were taken 342 mm downstream of the cathode.

beam size has a square root dependence on bunch charge [20, 72], the bunch charge shows no significant influence on the beam size. As a consequence, for most measurements performed at the test stand with SRI cathodes and solenoid focusing, the beam size at a location z is a function of the solenoid focusing strength alone.

Figure 6.13 shows how the beam size decreases with increased solenoid focusing. Interestingly the final solenoid setting of 55.3 mT leads to larger beam sizes than a setting of 49.3 mT. Obviously there lies a setting below 55.3 mT that minimizes beam size. This shall be investigated in the next section.

6.2.2 Transverse Beam Size as a Function of Solenoid Field

The solenoid focuses the beam as expected; in addition to focusing a slight beam steering is observed. This can be caused by a residual dipole component possibly due to misalignment. The steering is however on the order of the effect of the earth magnetic field and can therefore be corrected with the Helmholtz coils designed to compensate beam steering due to the earth magnetic field. Since the steering is a very small effect (less than 1 mm movement on the phosphor screen), compensation is however not required. Additionally, the polarity of the solenoid was inverted revealing no change in beam profile. This indicates that the solenoid magnetic field has only negligible higher order moments [73].

An example for solenoid focusing and its influence on the beam profile is given in Fig. 6.14. The effect of the solenoid on the beam is very strong: A mere 10 mT increase in solenoid magnetic field decreases the beam size by 0.8 mm or 28%.

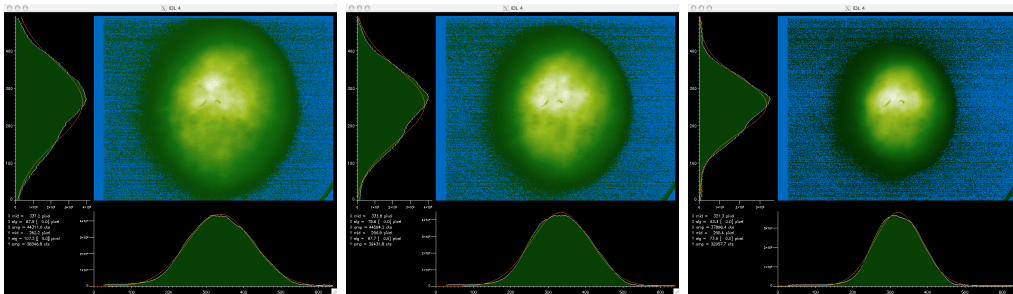


Figure 6.14: An example for solenoid focusing of a 40 keV bunch with 64 pC bunch charge emitted from SRI-1257B. The phosphor screen was positioned 257 mm downstream of the cathode; the image averages over 10 shots. The beam size reduces from $\sigma_x = 2.87$ mm (for $B_z = 25.8$ mT) to 2.61 mm (for $B_z = 29.3$ mT) and 2.08 mm (for $B_z = 35.2$ mT).

Figure 6.15 shows beam size evolution through the diagnostics section for different solenoid focusing strengths. Unfortunately no solenoid setting was found to demonstrate a beam waist in the diagnostic section.

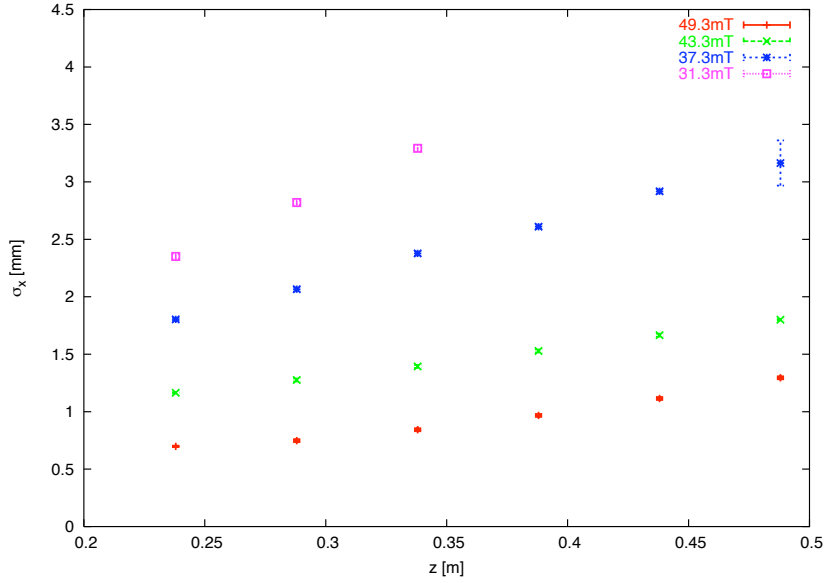


Figure 6.15: Beam size evolution in the diagnostics section measured for several solenoid focusing strengths. The phosphor screen monitor imaged 40 keV bunches with 59 pC bunch charge emitted from SRI-1257B. 10 shots were integrated for imaging. No solenoid setting was found that creates a beam waist in the area accessible by the phosphor screen.

Obviously the waist position is located upstream of the area accessible by the phosphor screen. Intuitively one would decrease the solenoid focusing strength in order to move the waist position further downstream. As is easily shown, this is however not always possible: From the transformation properties of the Courant-Snyder parameters

$$\begin{pmatrix} \beta \\ \alpha \\ \gamma \end{pmatrix} = \begin{pmatrix} \mathcal{M}_{11}^2 & -2\mathcal{M}_{11}\mathcal{M}_{12} & \mathcal{M}_{12}^2 \\ -\mathcal{M}_{11}\mathcal{M}_{21} & \mathcal{M}_{11}\mathcal{M}_{22} + \mathcal{M}_{21}\mathcal{M}_{12} & -\mathcal{M}_{12}\mathcal{M}_{22} \\ \mathcal{M}_{21}^2 & -2\mathcal{M}_{21}\mathcal{M}_{22} & \mathcal{M}_{22}^2 \end{pmatrix} \begin{pmatrix} \beta_0 \\ \alpha_0 \\ \gamma_0 \end{pmatrix} \quad (6.1)$$

and applying a drift matrix with length L_w from the lens to the waist position, the waist position L_w downstream of a focusing magnet is derived

$$\begin{aligned} \alpha_w = \alpha - L_w \gamma &\stackrel{!}{=} 0 \\ L_w &= \frac{\alpha}{\gamma} = \frac{\frac{\beta_0}{f} + \alpha_0}{\frac{\beta_0}{f^2} + \frac{2\alpha_0}{f} + \gamma_0}, \end{aligned} \quad (6.2)$$

where the subscript 0 denotes Courant-Snyder parameter values before the focusing magnet. With the magnet calibration given in Section 5.1, the focusing strength can be expressed by the solenoid field [7]

$$f = \frac{1}{k l_{\text{eff}}} \quad \text{and} \quad k = \left(\frac{B_{\text{max}}}{2 p/e} \right)^2. \quad (6.3)$$

The distance from the solenoid center to the waist position can then be calculated for all solenoid settings. This is shown in Fig. 6.16 where typical values at the solenoid entry yoke of $\beta_0 = 0.194$ m and $\alpha_0 = -3.93$ (see Table 6.5) have been applied (see Section 6.3.1).

As indicated, there is no solenoid focusing setting that will generate a focus in the diagnostics section. The maximum waist position L_w^{max}

$$\frac{\partial L_w}{\partial f} \stackrel{!}{=} 0 \quad \longrightarrow \quad L_w^{\text{max}} = \frac{\beta_0}{2} \quad (6.4)$$

is 151.5 mm downstream of the cathode which is not accessible by the phosphor screen. An explanation for the difference between the beam evolution observed here and the beam evolution expected from simulations will be given in Section 6.4.

6.2.3 Beam Size Measurement Comparison

Since all beam profile measurements (and hence beam size and Courant-Snyder parameters) rely on the phosphor screen monitor it is crucial to investigate systematic error contributions to the phosphor screen monitor measurements. For this purpose, the beam size evolution in the diagnostics

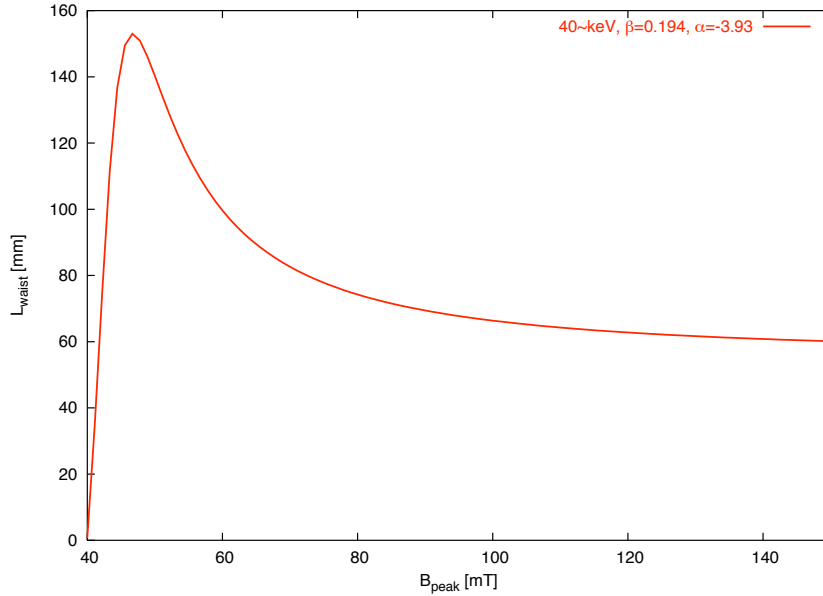


Figure 6.16: Waist position downstream of the cathode as a function of solenoid magnetic field. The plot shown here was derived for 40 keV electron bunches with typical values at the solenoid entry yoke of $\beta_0 = 0.194$ m and $\alpha_0 = -3.93$ (see Table 6.5).

section was measured and the data fitted to reveal the beam size at the position of the YAG screen. The beam profile was then measured with the YAG screen and the values compared.

The measurement of the beam size with the phosphor screen monitor is shown in Fig. 6.17. The beam used for this measurement was generated with SRI-1257B giving 40 keV bunches with 40.4 pC bunch charge and 642 μ A peak current. The applied solenoid magnetic field was 53.6 mT. Beam size in y was slightly larger than in x . σ^2 increases quadratically with s as expected downstream of a beam waist.² A quadratic fit was applied to both data sets and the waist position and beam size at 218 mm downstream of the cathode (position of the YAG screen monitor) derived. This is shown in Table 6.1.

²The quadratic growth of $\sigma^2 = \varepsilon\beta$ downstream of a waist is derived from Eq. (6.1) assuming constant emittance. This is the case here because the beam emitted by the SRI cathodes is emittance dominated.

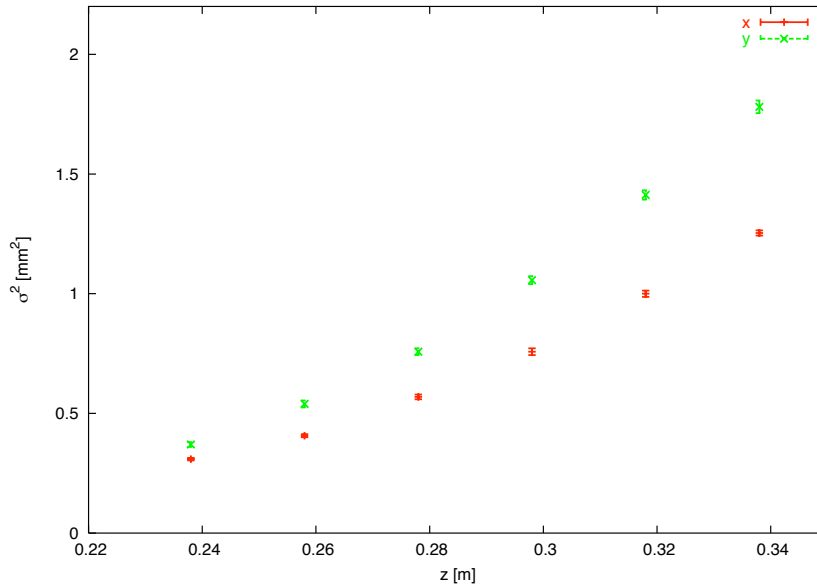


Figure 6.17: Beam size evolution in the diagnostics section. SRI-1257B emitted 40 keV bunches with 40.4 pC bunch charge and 642 μ A peak current. The applied solenoid field was 53.6 mT. Ten shots were integrated to improve imaging.

The errors on the fit parameters are rather large (7% –14%) and lead to a large uncertainty for the beam size calculation. Nevertheless the derived beam size at the location of the YAG screen monitor ($z = 219$ mm) is compatible with beam size measured with the YAG screen. The large errors on the YAG screen are due to a bad SNR; the YAG screen is less sensitive than the P43 phosphor screen. In addition, deviations of the beam profile from a perfectly Gaussian distribution give additional error contributions.

Within the precision of the measurement both methods deliver compatible results which indicates no systematic errors have been disregarded. The only systematic contribution common to both methods would originate from the CCD camera or the frame grabber. That contribution has been measured to be on the order of a few μ m (see Section 5.2) which is well below the error of both measurements shown here.

Table 6.1: Evaluation of the beam size data given in Fig. 6.17. A quadratic fit is applied to the beam size data to derive waist position and beam size at the YAG screen position. This is then compared with YAG screen monitor measurements of beam size. Both methods give compatible beam size results.

σ_x^2 evolution fit parameters		
	c_2	51.89 ± 3.86
	c_1	-20.34 ± 2.19
	c_0	2.21 ± 0.31
σ_y^2 evolution fit parameters		
	c_2	72.44 ± 4.92
	c_1	-27.44 ± 2.75
	c_0	2.79 ± 0.38
Derived waist positions		
	$z_{w,x}$ [mm]	196 ± 26
	$z_{w,y}$ [mm]	189 ± 23
Derived beam size at $z = 219$ mm		
	σ_x [mm]	0.494
	σ_y [mm]	0.505
Measured beam size at $z = 219$ mm (YAG)		
	σ_x [mm]	0.514 \pm 0.059
	σ_y [mm]	0.416 \pm 0.141

6.3 Emittance Measurements

This section presents emittance and transverse phase space distribution measurements. The first part introduces different emittance measurement methods and gives the acquired results. The second part deals with emittance changes due to bunch charge variation or HV. Finally, it is demonstrated how emittance measurements can be used to investigate characteristics of the emission process of SRI cathodes.

6.3.1 Solenoid Scan

Apart from the two emittance measurement techniques introduced in Section 4.7, the solenoid magnet can be used as a quasi-independent method to measure beam emittance and Courant-Snyder parameters.³ In a *solenoid scan* the downstream beam size is measured as a function of the solenoid strength and the Courant-Snyder parameters are derived from this focusing property. There are different modeling approximations for the solenoid magnet: It can be treated as a thin or thick lens. If treated as a thick lens it can be approximated by a hard edge magnet or with smooth edges using slices as calibrated (see Fig. 5.5). These different methods will be introduced here.

Thin Lens Treatment

In thin lens approximation solenoid focusing (focusing strength k , effective length l_{eff}) and a subsequent drift of length L can be expressed by the simple transfer matrix

$$\mathcal{M} = \mathcal{M}_d \mathcal{M}_{\text{sol}} = \begin{pmatrix} 1 - L k l_{\text{eff}} & L \\ -k l_{\text{eff}} & 1 \end{pmatrix}. \quad (6.5)$$

³The method is independent apart from the fact that the same phosphor screen monitor is used for beam imaging. However, the systematic contributions of the phosphor screen monitor system are so small that they do not give a significant contribution.

The transformation of the Courant-Snyder parameters (6.1) from the solenoid center $[\beta, \alpha, \gamma]_s$ to the end of the drift section $[\beta, \alpha, \gamma]$ gives a quadratic function in k for σ^2

$$\begin{aligned} \sigma^2 &= \varepsilon\beta = \mathcal{M}_{11}^2\varepsilon\beta_s - 2\mathcal{M}_{11}\mathcal{M}_{12}\varepsilon\alpha_s + \mathcal{M}_{12}^2\varepsilon\gamma_s \\ &\vdots \\ &= k^2 \underbrace{(L^2 l_{\text{eff}}^2 \varepsilon\beta_s)}_{c_2} + k \underbrace{(2L^2 l_{\text{eff}} \varepsilon\alpha_s - 2L l_{\text{eff}} \varepsilon\beta_s)}_{c_1} + \underbrace{(\varepsilon\beta_s - 2L\varepsilon\alpha_s + L^2\varepsilon\gamma_s)}_{c_0}. \end{aligned}$$

If $\sigma_{x,y}$ data is taken as a function of solenoid focusing strength k , the solenoid scan gives emittance and Courant-Snyder parameters for both transverse directions. Beside focusing, a solenoid magnet rotates the beam in the transverse plane. In order to use the previously introduced solenoid scan approach this rotation has to be taken into account. In the measurements performed at the gun test stand this was not required since the beam was approximately round and showed only a slight aspect ratio. The correction due to solenoid rotation is negligible in this case.⁴

The fit parameters c_i are then used to derive the emittance and Courant-Snyder parameters according to

$$\begin{aligned} \varepsilon &= \frac{\sqrt{c_0 c_2 - c_1^2/4}}{L^2 l_{\text{eff}}}, \\ \beta_s &= \frac{1}{\varepsilon} \frac{c_2}{L^2 l_{\text{eff}}}, \\ \alpha_s &= \frac{1}{\varepsilon} \left(\frac{c_1}{2L^2 l_{\text{eff}}} + \frac{c_2}{L^3 l_{\text{eff}}^2} \right), \\ \gamma_s &= \frac{1}{\varepsilon} \left(\frac{c_0}{L^2} + \frac{c_1}{2L^3 l_{\text{eff}}} + \frac{c_2}{L^4 l_{\text{eff}}^2} \right). \end{aligned} \quad (6.6)$$

An example for such a solenoid scan is given in Fig. 6.18. The phosphor screen monitor was positioned 257 mm downstream of the cathode giving a drift distance of $L = 202$ mm. The beam size was measured as a function

⁴For the solenoid strengths applied ($k = 500 - 1800 \text{ m}^{-2}$) the solenoid rotation angle $\phi = \sqrt{k} l_{\text{eff}}$ changes by no more than 19° .

of solenoid current. The plot shown in the example gives the square of the beam size σ^2 as a function of the focusing strength k . The quadratic fit approximates the data well. The only significant differences are seen for large beam sizes in y direction where measurement is difficult (SNR, beam profile cut off) and the acquired beam size values have large errors.

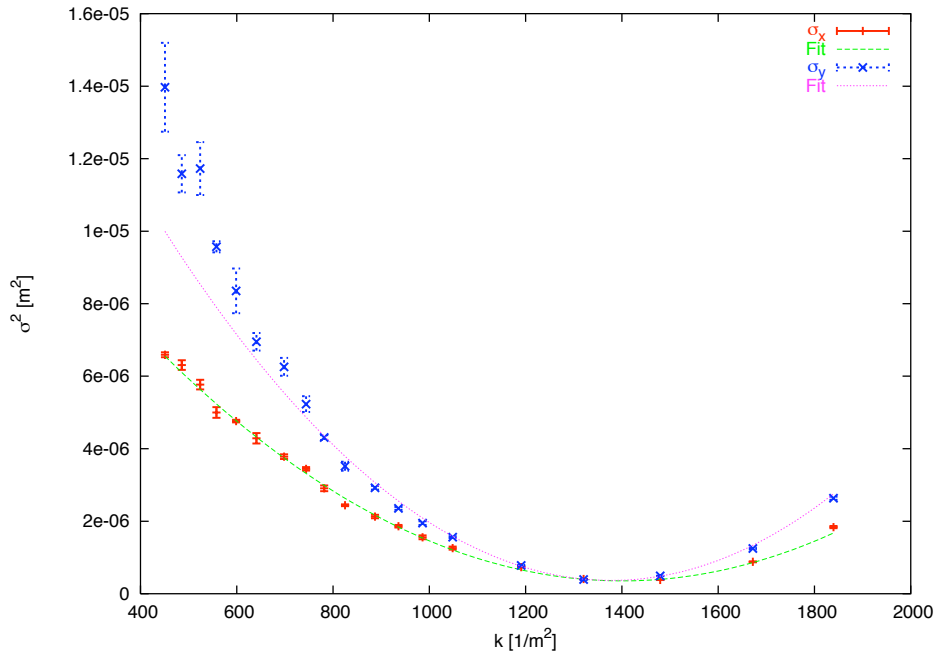


Figure 6.18: Solenoid scan and fit: Beam size measured as a function of solenoid focusing strength. The data shows beam sizes of 40 keV bunches emitted from SRI-1257B with 39 pC bunch charge. The phosphor screen monitor was positioned 257 mm downstream of the cathode (202 mm from the solenoid center). Five shots were integrated to improve beam imaging.

The code SOLSCAN was written in GNU Octave; it performs the quadratic fit on the measurement data and returns the emittance and Courant-Snyder parameters. In addition, the beta function and beam size at the waist preced-

ing the solenoid as well as the distance to this waist are calculated according to Eq. (6.1)

$$\begin{aligned}\beta_w &= \frac{1}{\gamma_s}, \\ \sigma_w &= \sqrt{\frac{\varepsilon}{\gamma_s}}, \\ \Delta s &= -\frac{\alpha_s}{\gamma_s}.\end{aligned}\tag{6.7}$$

Finally, SOLSCAN also calculates the beam size and beta function at the location of the phosphor screen for no solenoid focusing according to

$$\begin{aligned}\sigma &= \sqrt{c_0}, \\ \beta &= \frac{c_0}{\varepsilon}, \\ \alpha &= -\frac{1}{\varepsilon} \left(\frac{c_0}{L} + \frac{c_1}{2L^2 l_{\text{eff}}} \right).\end{aligned}\tag{6.8}$$

Table 6.2 summarizes the values returned by SOLSCAN for the measurement shown in Fig. 6.18. Error propagation (error of solenoid and phosphor screen position, magnet strength uncertainty, error covariances) is calculated analytically.

Thick Lens Treatment

The previously discussed thin lens approach is a good approximation if the effective lens length is small compared to the focal length

$$l_{\text{eff}} \ll f_{\text{sol}} = \frac{1}{k l_{\text{eff}}}.\tag{6.9}$$

Due to the comparably large effective length of the test stand solenoid, this approximation is inadequate for the strong focusing strengths required to measure both sides of the parabola. Therefore, the thin lens approximation is not suitable for evaluation of solenoid scan data at the test stand. Instead

Table 6.2: Summary of SOLSCAN fit and derived results for the solenoid scan data shown in Fig. 6.18. The error covariances have been omitted in this table but have been used for the error calculation.

	x	y
Fit parameters		
c_2	$6.87\text{e-}12 \pm 1.29\text{e-}13$	$1.12\text{e-}11 \pm 3.66\text{e-}13$
c_1	$-1.92\text{e-}8 \pm 3.24\text{e-}10$	$-3.09\text{e-}8 \pm 9.58\text{e-}10$
c_0	$1.38\text{e-}5 \pm 2.06\text{e-}7$	$2.16\text{e-}5 \pm 6.26\text{e-}7$
At solenoid center		
ε [mm mrad]	2.26 ± 0.10	2.94 ± 0.16
β_s [m]	0.260 ± 0.021	0.327 ± 0.030
α_s	-4.88 ± 0.36	-6.00 ± 0.52
At waist before solenoid		
β_w [mm]	10.5 ± 1.7	8.8 ± 1.7
σ_w [mm]	0.154 ± 0.026	0.161 ± 0.032
Δs [mm]	51.2 ± 5.5	53.0 ± 6.5
At phosphor screen		
σ [mm]	3.72 ± 0.03	4.65 ± 0.07
β [m]	6.12 ± 0.28	7.37 ± 0.45
α	-24.1 ± 1.2	-28.8 ± 1.9

the solenoid magnet has to be treated as a thick lens and the transfer matrix calculated according to

$$\mathcal{M} = \mathcal{M}_d \mathcal{M}_{\text{sol}} = \begin{pmatrix} \cos \phi - L\sqrt{k} \sin \phi & \frac{1}{\sqrt{k}} \sin \phi + L \cos \phi \\ -\sqrt{k} \sin \phi & \cos \phi \end{pmatrix}, \quad (6.10)$$

where $\phi = \frac{1}{2} \frac{e}{p} \int B ds$ is the solenoid rotation angle, $k = (\frac{1}{2} \frac{e}{p} B_{\text{max}})^2$ is the focusing strength, and L is the drift length. The beam size can then be

expressed by the solenoid strength and the Courant-Snyder parameters

$$\sigma = \sqrt{\varepsilon \left(\beta_s^2 \mathcal{M}_{11}^2 - 2\alpha_s \mathcal{M}_{11} \mathcal{M}_{12} + \frac{1 + \alpha_s^2}{\beta_s} \mathcal{M}_{12}^2 \right)}. \quad (6.11)$$

The disadvantage of this approach is that the Courant-Snyder parameters are no longer derived from the beam size data with a simple quadratic fit. Instead the Levenberg-Marquardt fitting method [74] is used: σ is measured as a function of solenoid current (in the matrix coefficients \mathcal{M}_{ij}) and the fit returns the emittance ε and the Courant-Snyder parameters including errors at the solenoid entry yoke β_s, α_s .

The Levenberg-Marquardt fitting routine was already available in EMM [75], an IDL program originally written to evaluate quadrupole scan data taken at the SLS linac. The new code EML was derived from EMM and modified for solenoid scans at the test stand. In addition to performing the Levenberg-Marquardt fit and returning emittance and Courant-Snyder parameters, EML returns the parameters given in Eqs. (6.7) and (6.8) just like SOLSCAN.

Furthermore, EML can perform the fit for a hard edge solenoid magnet model directly applying the matrix given in Eq. (6.10) or according to the solenoid calibration data where the solenoid matrix is calculated with solenoid slice matrices according to calibration data (see Fig. 5.5). The advantage of this method is that it does not assume a hard edge magnet with a rectangular longitudinal field distribution. Instead it uses the solenoid calibration data to model the solenoid as exactly as possible with the available calibration data.

Figure 6.19 shows the same measurement data as in Fig. 6.18, this time however analyzed with EML for a hard edge model of the test stand solenoid. Figure 6.20 shows EML analysis for the same data set but using a smooth edge model for the solenoid magnet derived from the magnet calibration data.

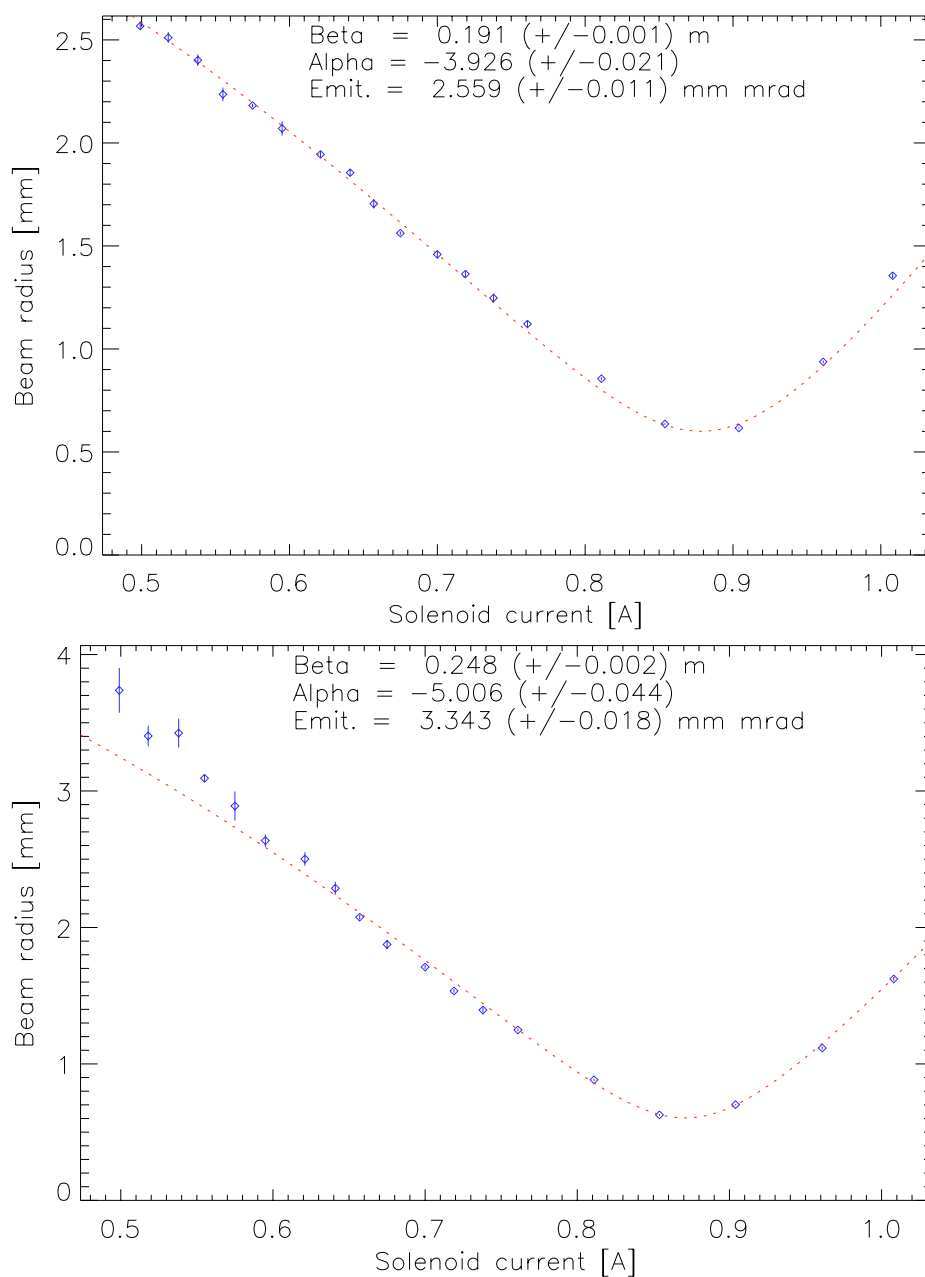


Figure 6.19: Solenoid scan and analysis performed with EML for the same data set as shown in Fig. 6.18. The upper plot shows data for x , the lower plot for y . EML used a thick lens hard edge solenoid model.

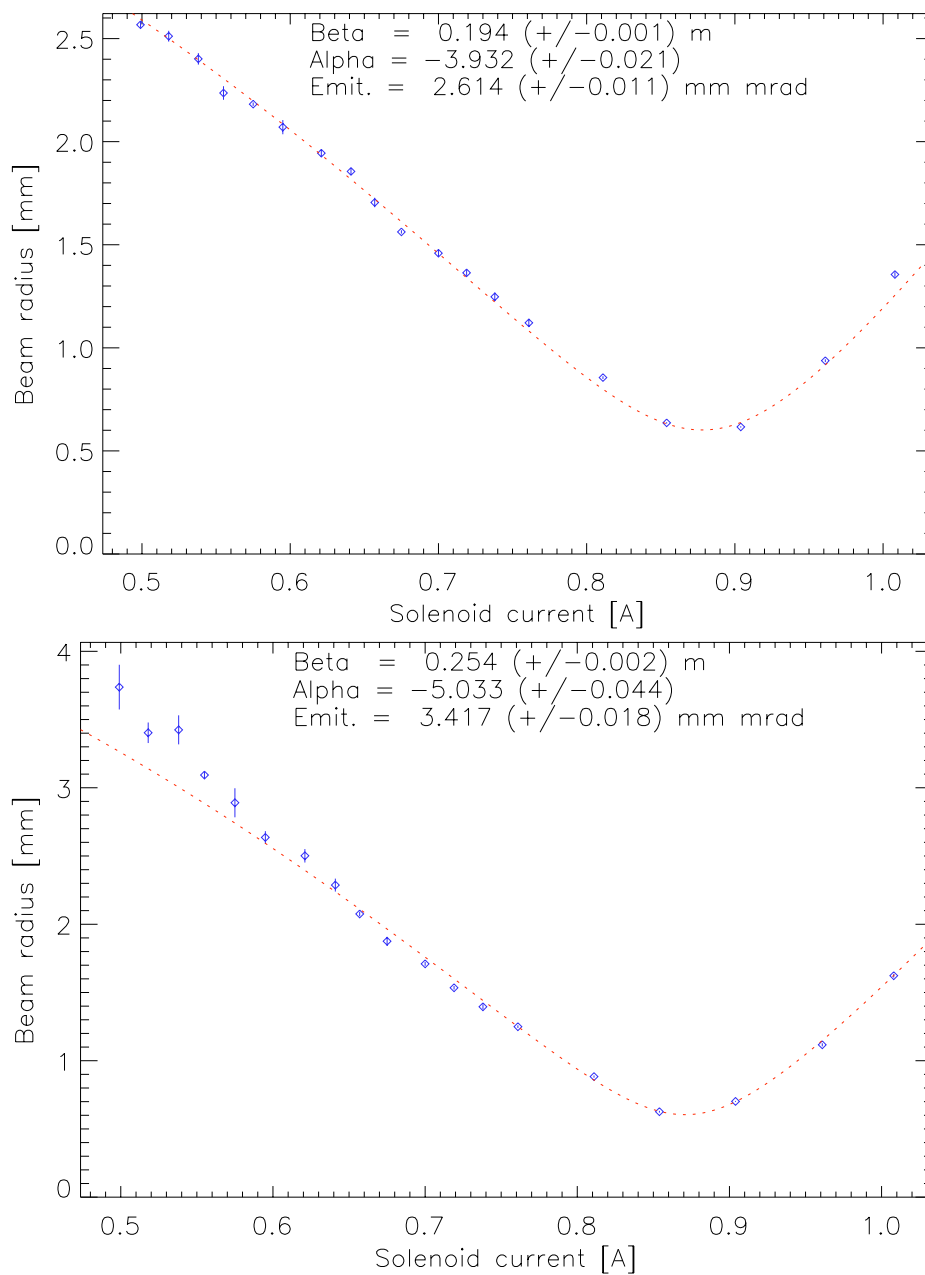


Figure 6.20: Solenoid scan and analysis performed with EML for the same data set as shown in Fig. 6.18. The upper plot shows data for x , the lower plot for y . EML used a thick lens smooth edge solenoid model.

Table 6.3 shows a comparison of the results acquired in the thin lens, thick lens hard edge and thick lens smooth edge model and gives differences. Thick lens treatment of the solenoid returns larger emittance values than in the thin lens approximation. In fact, the smooth edge solenoid model gives largest emittance values. The intuitive picture is that in the smooth edge model, focusing starts in the fringes reducing the bunch size in the solenoid and thus the focusing in the remaining part of the solenoid is weaker than in the thin lens approximation. The hard edge model is already a good approximation of the actual solenoid magnet.

Table 6.3: Summary of fit results for the solenoid scan data shown in Fig. 6.18. The emittance is given in units [mm mrad] and the beta function in [m]. The difference between the thin lens approximation values and the thick lens smooth edge model values are given in the last row.

	ε_x	ε_y	β_x	β_y	α_x	α_y
Thin lens approximation	2.26	2.94	0.164	0.209	-3.83	-4.76
Thick lens, hard edge	2.56	3.34	0.191	0.248	-3.93	-5.01
Thick lens, smooth edge	2.61	3.42	0.194	0.254	-3.93	-5.03
Δ	+15%	+16%	+18%	+22%	-3%	-6%

The disadvantage of using the thick lens model is that analytical error propagation as used in SOLSCAN is not possible with the Levenberg-Marquardt method.⁵ Instead the contribution of errors has to be calculated for each case and the total error then specified as the sum of squares. The error

⁵The Levenberg-Marquardt method takes into account that measurement data carries errors and hence it returns errors for the derived emittance and Courant-Snyder parameters. However, additional parameters used for the derivation carry uncertainties (positioning, solenoid strength, and optics calibration) as well. These errors cannot be propagated analytically.

contributions are: positioning error of the phosphor screen and optics calibration error. An evaluation for the contribution of each uncertainty has been performed; the results are shown in Table 6.4.

Table 6.4: Error contributions in the thick lens smooth edge model calculated with EML for the evaluation given in Fig. 6.20. The error contributions are independent and thus added quadratically to derive the total error. The largest error contribution is the uncertainty of the pixel size which gives a beam size error and hence an emittance error.

	$\Delta\varepsilon/\varepsilon$	$\Delta\beta/\beta$	$\Delta\alpha/\alpha$
Specified fit error	$\pm 0.5\%$	$\pm 0.7\%$	$\pm 0.7\%$
Positioning uncertainty			
$\Delta L = \pm 1$ mm	$\pm 1.0\%$	$\pm 0.0\%$	$\pm 0.1\%$
Optics calibration uncertainty			
$\Delta p/p = \pm 3.3\%$	$\pm 6.6\%$	$\pm 0.0\%$	$\pm 0.0\%$
Total error	$\pm 6.7\%$	$\pm 0.7\%$	$\pm 0.7\%$

This leads to a final set of Courant-Snyder parameters at the solenoid entry yoke shown in Table 6.5. Similar to the evaluations performed in Eq. (6.7) the waist parameters are calculated with EML as well. The solenoid scan method allows reconstruction of the 1-sigma phase space ellipse with the Courant-Snyder parameters (as demonstrated in Fig. 2.1). A 1-sigma phase space ellipse for the data measured in this example is given in Fig. 6.21.

As seen in Table 6.5, the waist location given by EML in the smooth edge model is roughly 47 mm away from the solenoid entry yoke. This would put the waist location 3 mm upstream of the cathode. The thin lens approximation puts the waist at ≈ 3 mm downstream of the cathode (see Table 6.3); the thin lens hard edge model puts the waist at ≈ 2 mm upstream of the cathode. However, the linear beam optics used to calculate this waist position do not take into account the acceleration of the beam in the diode gap and therefore values upstream of the anode iris should be taken with caution.

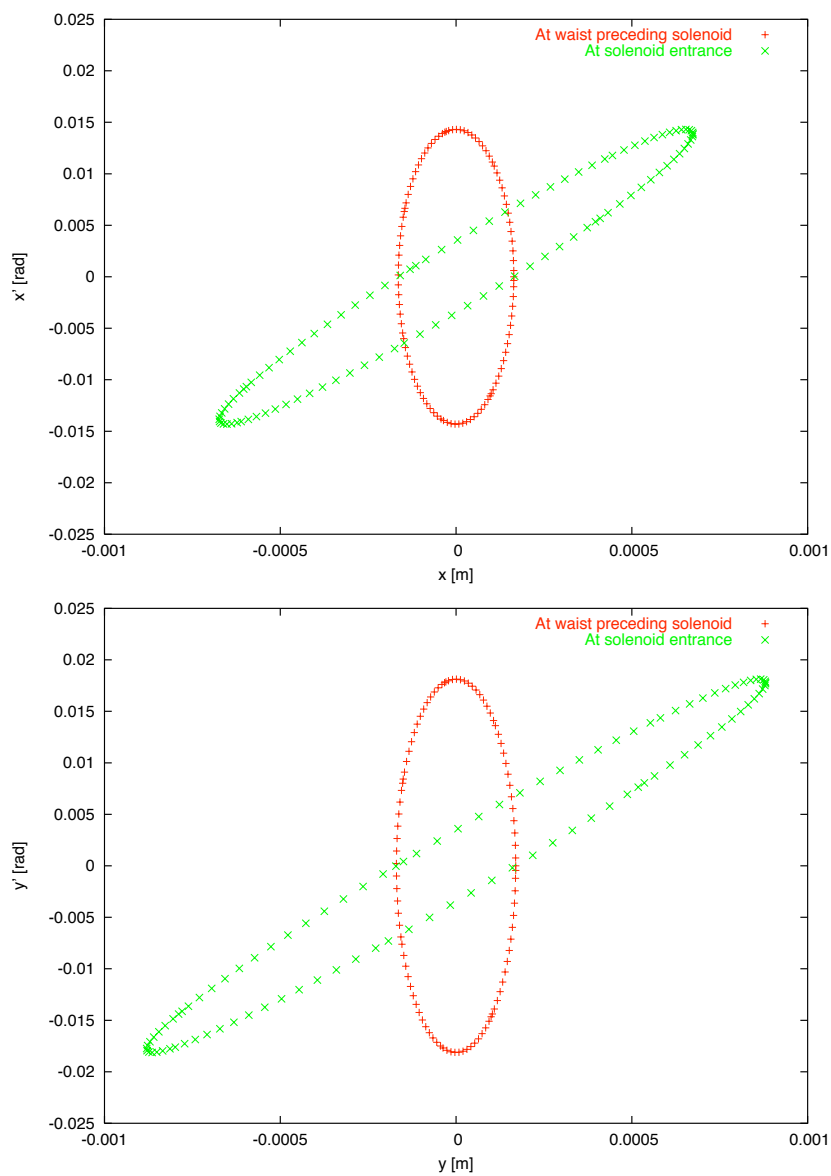


Figure 6.21: Approximated 1-sigma phase space ellipses for the data analyzed with EML. The upper plot shows data for x , the lower plot shows data for y . The upright ellipse is at the waist location upstream of the solenoid, the tilted ellipse is at the solenoid entry yoke.

Table 6.5: Results derived with EML for the solenoid scan data shown in Fig. 6.18. The Courant-Snyder parameters at the solenoid entry yoke as well as the parameters at the waist preceding the solenoid are given.

	x	y
ε [mm mrad]	2.614 ± 0.175	3.417 ± 0.229
β_s [m]	0.194 ± 0.001	0.254 ± 0.002
α_s []	-3.932 ± 0.028	-5.033 ± 0.036
σ_s [mm]	0.712 ± 0.024	0.931 ± 0.031
β_w [mm]	11.79 ± 0.18	9.65 ± 0.15
σ_w [mm]	0.176 ± 0.006	0.182 ± 0.006
Δs [mm]	46.31 ± 0.42	48.55 ± 0.45

6.3.2 Measurements with the Single Slit

The solenoid scan requires many shots to properly resolve the beam focusing and return exact fit values. The single slit emittance measurement method is used to measure the beam emittance in principally one shot. In addition, the single slit emittance measurement can be used as an quasi-independent measurement method to verify solenoid scan results. An example for this measurement method is given in Fig. 6.22.

Prior to inserting the single slit into the beam, the beam size at the location of the slit is measured by inserting the YAG screen. In a second step the single slit is driven into the beam path and the phosphor screen monitor is used to measure the size of the slit image. Together with the drift distance between the slit and the phosphor screen, this image size gives the uncorrelated beam divergence according to Eq. (4.4). Table 6.6 gives measurement data and derived results.

The emittance derived from the single slit measurement is in agreement with the result given by the solenoid scan. However, a possible additional source

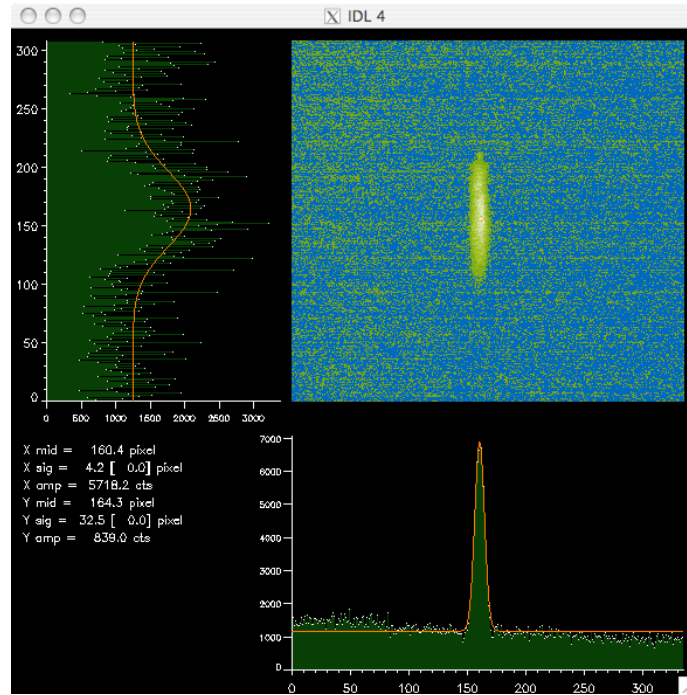


Figure 6.22: Example of a single slit emittance measurement. At 40 keV SRI-1257B emitted 40 pC bunches with 100 ns bunch length. The phosphor screen was positioned 39 mm downstream of the slit array; 25 shots were integrated to achieve a sufficient SNR. The applied solenoid field was 47.3 mT. The beam size at the slit location was 0.68 mm.

of error is the finite slit width which gives a contribution to the image width even for a zero divergence beam.

An attempt to reduce this error contribution is to increase the spacing between slit mask and phosphor screen. With the current FEAs this is somewhat problematic because with the increased image width the already bad SNR⁶ further reduces. An example for this procedure is given in Table 6.7 where the final divergence is derived from the asymptotic beamlet image width.

⁶Even for a well focused beam, the single slit stops roughly 95% of the beam. For the weak current of the SRI FEA bunches, imaging the remaining 5% charge in the beamlet is challenging. Single slit measurements performed at the test stand therefore integrated over 25 shots to increase the SNR.

Table 6.6: Single slit emittance measurement results and analysis for the data shown in Fig. 6.22. The derived emittance is in agreement with the emittance obtained with the solenoid scan (see Table 6.5).

Beam size at YAG location		
σ_x [pixel]		8.7 ± 0.5
σ_x [mm]		0.682 ± 0.039
Slit image size on P43		
σ_x [pixel]		4.2 ± 0.2
σ_x [mm]		0.138 ± 0.007
Drift from slit to P43		
L [mm]		39.0 ± 1.0
Derived beam divergence		
σ'_x [mrad]		3.54 ± 0.20
Derived beam emittance		
ε_x [mm mrad]		2.41 ± 0.19

Table 6.7: Measurement of the beamlet image width σ_x for different drift distances to the phosphor screen L . 25 shots of a 40 keV 40pC bunch are integrated. A solenoid field of 53.6 mT was used to minimize the beam size on the slit mask. The error of the derived divergence due to the finite slit width is given.

L [mm]	σ_x [mm]	σ'_x [mrad]	ε_x [mm mrad]	Δ
39	0.577 ± 0.004	14.80 ± 0.10	8.18 ± 0.06	+2.8%
49	0.718 ± 0.012	14.65 ± 0.25	8.10 ± 0.14	+1.8%
59	0.859 ± 0.012	14.56 ± 0.20	8.05 ± 0.11	+1.1%
69	0.996 ± 0.008	14.43 ± 0.12	7.98 ± 0.07	+0.2%
79	1.137 ± 0.016	14.39 ± 0.20	7.96 ± 0.11	-

The results show almost 3% error. This is however considerably more than what is expected from the finite slit width. It is assumed that this discrepancy is a consequence of the poor image size measurement for large drift distances.

The emittance values derived in Table 6.7 are much larger than all previous measurements. The reason for these large emittance values lies in damage of the FEA caused by an arc during HV breakdown. This will be discussed in Section 6.3.6.

6.3.3 Measurements with the Slit Array

The disadvantage of the single slit measurement method is that it requires knowledge of the beam size at the location of the slits. The slit array measurement method does not require this knowledge since counting the number of illuminated slits gives the beam size if the slit pitch is known. An example is shown in Fig. 6.23.

The measurement shows that the beamlet images overlap due to large divergences; this prevents proper analysis. The divergences can be reduced if the beam is defocused. This however implies that the beam spot on the slit mask increases and thus the SNR of the slit images become worse. At the test stand it was not possible to find a setting which gave sufficient SNR while preventing beamlet image overlap.

This behavior is explained by deriving the maximum emittance that can be resolved with a slit array. Similar to the Rayleigh criterion for diffraction, there is a criterion for emittance measurement with a slit array [18]. If beamlet image maxima are to be separated by 3 standard deviations of the beamlet distribution, the maximum resolvable emittance is

$$\varepsilon_{\max} = \sigma_x \sigma'_x = \frac{\sigma_x w}{3 L}, \quad (6.12)$$

where w is the pitch of the array and L is the drift length between slit array and screen. For a beam size of roughly $\sigma_x = 0.7$ mm (further increasing the

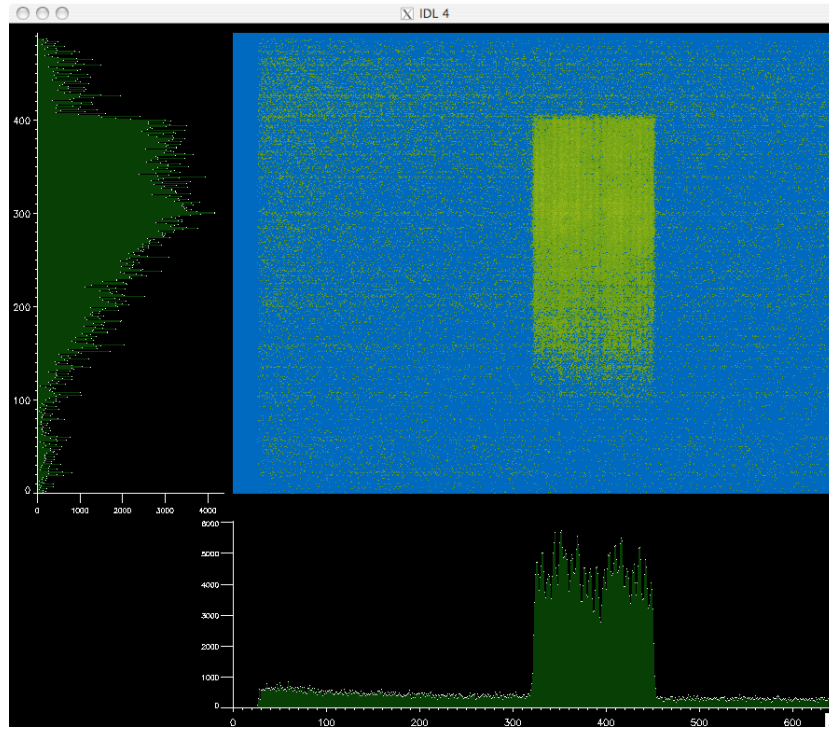


Figure 6.23: Slit array measurement example for a 40 keV bunch with a bunch charge of 56 pC. The solenoid setting was 25.7 mT; the phosphor screen was positioned 39 mm downstream of the slit array. All 20 slits are illuminated by the beam. The beam divergence is however so large that the beamlet images overlap and their width cannot be properly measured.

beam size is not possible due to the SNR) this gives a maximum resolvable emittance of $\varepsilon_{\max} = 1$ mm mrad for the minimum drift length of 39 mm.

The slit array is therefore not adequate for measuring a bunch with an emittance of roughly 2.4 mm mrad. To properly resolve such an emittance, the slit array pitch would have to be increased from 170 μm to about 400 μm . The reason for the specification of the slit array lies in the early assumption that the emittance of an FEA beam would be on the order of 0.1 mm mrad rather than 1 mm mrad. The lack of a focusing layer on the SRI FEAs increases source divergence and thus source emittance. This will be further discussed in Section 7.

6.3.4 Measurements with the Pinhole Array

The slit array delivers emittance and Courant-Snyder parameters for a phase plane in one shot. The values for the other phase plane are acquired in a second shot with a perpendicular array. Both sets of information can be acquired in a single shot with a pinhole array. Fortunately the pinhole array used at the test stand has a larger pitch of $320 \mu\text{m}$ increasing the maximum resolvable emittance to $\varepsilon_{\text{max}} \approx 2 \text{ mm mrad}$. If some image overlap is tolerated the pinhole array should be suitable to measure emittance at the gun test stand. An example of a pinhole array measurement is given in Fig. 6.24.

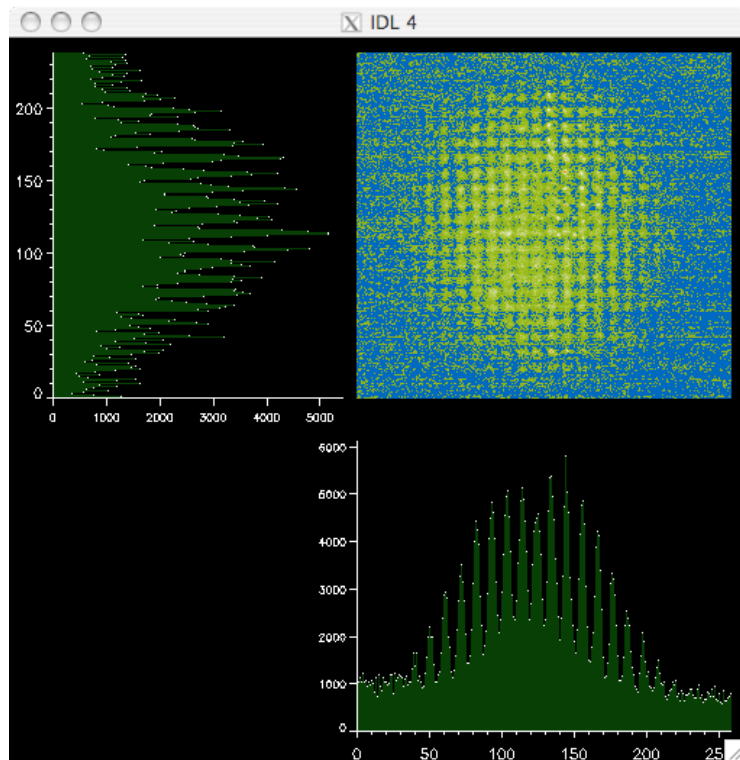


Figure 6.24: Pinhole array emittance measurement example. The phosphor screen was positioned 39 mm downstream of the slit array; 25 shots of 39 pC bunches from SRI-1257B were integrated. A region of interest has been selected to reduce background. The applied 40.8 mT solenoid field was an optimum setting for minimum overlap and maximum SNR.

In the example a slight overlap of beamlet images is observed. Nevertheless the image is sufficient for phase space reconstruction. The GNU Octave application RECONSTRUCTION makes a histogram of the data, removes background and bins the data. For each bin, (a horizontal or vertical slice of the bunch) the correlated divergence and centroid position are calculated according to Eqs. (4.5) and (4.6) and the resulting values are centered in phase space. This is shown in Figs. 6.25 and 6.26.

From the slice reconstruction, the second order moments of the bunch distribution are calculated which gives emittance and Courant-Snyder parameters at the location of the pinhole mask. The results of the pinhole measurement data shown here are given in Table 6.8.

Table 6.8: Pinhole emittance measurement results for the measurement data displayed in Fig. 6.24. The emittance and Courant-Snyder parameters are calculated for the location of the pinhole array. The errors are derived from a parameter variation (see below).

	x	y
ε [mm mrad]	2.846 ± 0.262	3.461 ± 0.318
β [m]	0.592 ± 0.027	0.654 ± 0.030
α []	-1.17 ± 0.61	-1.10 ± 0.58
σ [mm]	1.298 ± 0.067	1.505 ± 0.077

As with the Levenberg-Marquardt fit performed for the solenoid scan analysis, errors cannot be analytically propagated in this reconstruction and thus an error estimate has to be done by variation of input parameters and observation of the influence on the result. This procedure is shown in Table 6.9.

The results are compatible with the results given by the solenoid scan and the single slit measurement methods. However, the emittance results appear systematically too high. This can be explained by the remaining beamlet overlap: The overlapping images lead to a perceived broadening of the

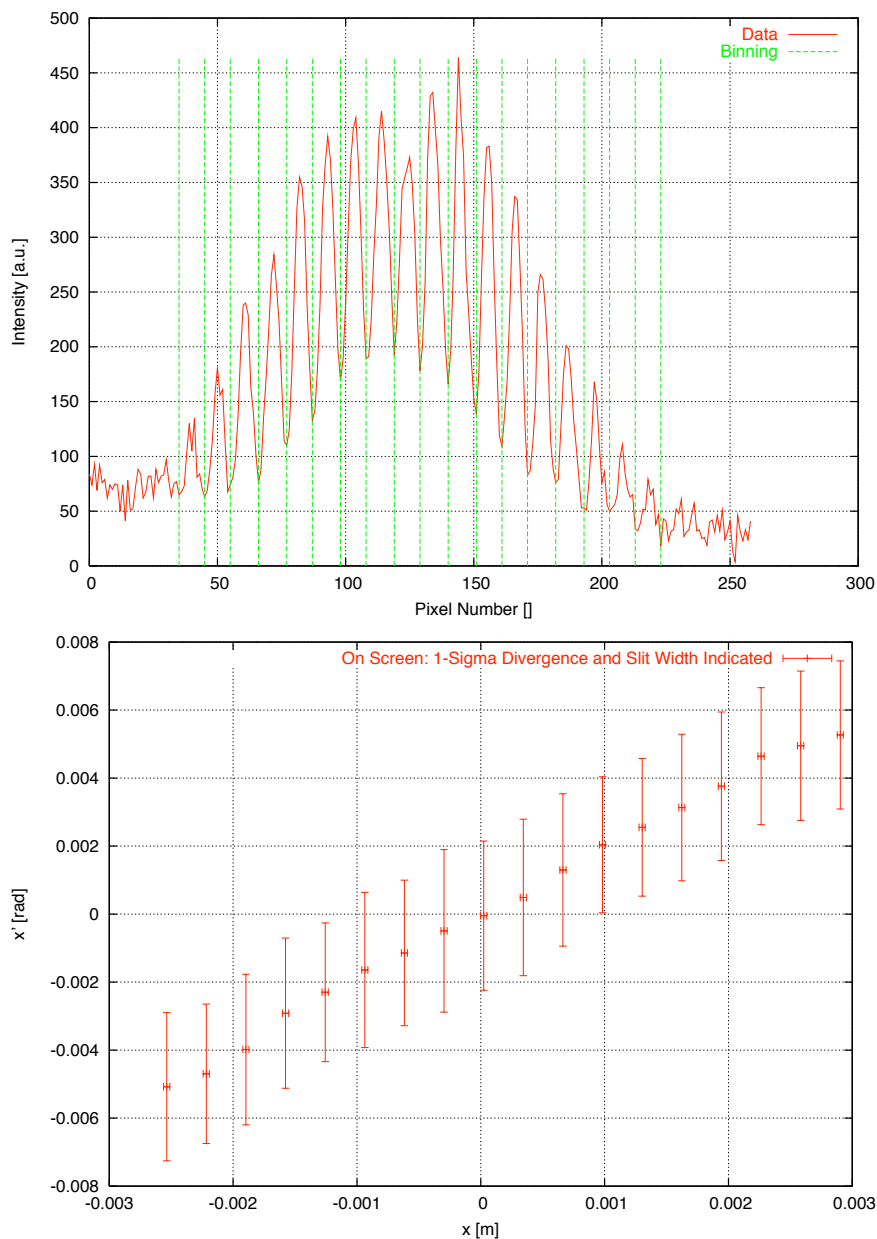


Figure 6.25: Analysis of the horizontal pinhole data shown in Fig. 6.24. The application *RECONSTRUCTION* bins the histogram data for each bunch slice and subtracts the background (top). For each beam slice the correlated divergence spread and centroid position is calculated. Both data sets are centered in phase space and plotted (bottom).

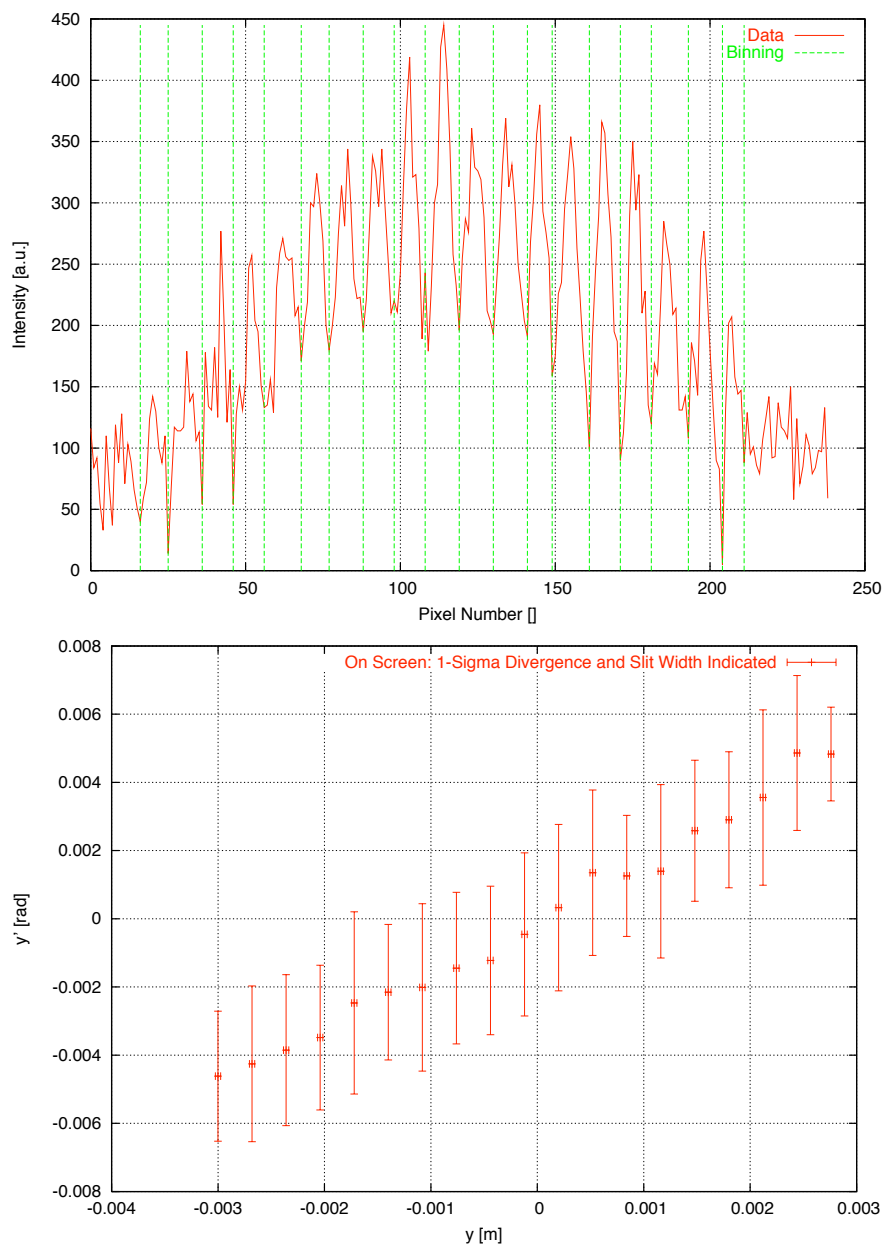


Figure 6.26: Analysis of the vertical pinhole data shown in Fig. 6.24. The application *RECONSTRUCTION* bins the histogram data for each bunch slice and subtracts the background (top). For each beam slice the correlated divergence spread and centroid position is calculated. Both data sets are centered in phase space and plotted (bottom).

Table 6.9: Error contributions for pinhole measurement analysis (for measurement shown in Fig. 6.24). The error contributions are independent and thus added quadratically to derive the total error. The emittance value depends strongly on the chosen background level. While the error of β remains low, α carries a large error. This is mainly due to the optics calibration uncertainty.

	$\Delta\varepsilon/\varepsilon$	$\Delta\beta/\beta$	$\Delta\alpha/\alpha$
Background level			
$\Delta I/I = \pm 2\%$	$\pm 8.0\%$	$\pm 1.0\%$	$\pm 3.0\%$
Pinhole pitch error			
$\Delta w = \pm 5 \mu\text{m}$	$\pm 1.6\%$	$\pm 1.6\%$	$\pm 23.9\%$
Positioning uncertainty			
$\Delta L = \pm 1 \text{ mm}$	$\pm 2.6\%$	$\pm 2.6\%$	$\pm 0.0\%$
Optics calibration uncertainty			
$\Delta p/p = \pm 3.3\%$	$\pm 3.3\%$	$\pm 3.3\%$	$\pm 46.6\%$
Total error	$\pm 9.2\%$	$\pm 4.6\%$	$\pm 52.5\%$

beamlet distribution and hence the divergence spread of the slice is shifted to higher values giving an increased emittance value.

Finally, every pixel on the CCD can be mapped to an area of phase space (see Section 4.7.5). Using the relative intensity of the pinhole beamlets, a full reconstruction of the transverse phase space density is performed. At the test stand this is done with the IDL application PHSPDENS. An example of this phase space reconstruction for the measurement data shown in Fig. 6.24 is given in Fig. 6.27. The reduced SNR for the vertical data is clearly noticed as a blurring of the phase space ellipse contours. Increasing the SNR and reducing beamlet image overlap will further improve the quality of the reconstructed phase space density plots.

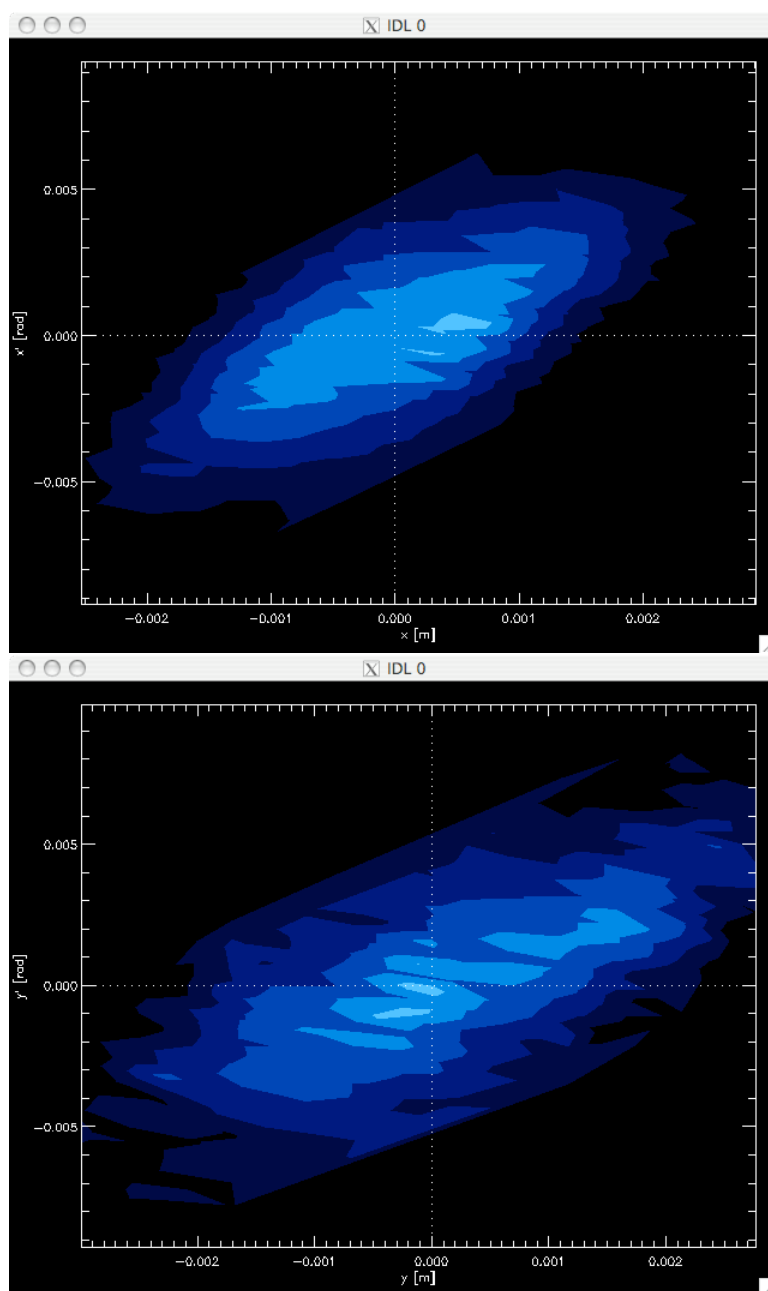


Figure 6.27: Reconstructed phase space densities from PHSPDENS. The top image (x plane) shows a better reconstruction than the bottom picture (y plane); this is due to the superior SNR of the horizontal data and the reduced amount of beamlet image overlap in the horizontal direction.

A comparison of the beam size measured directly with the phosphor screen and the beam size derived from the pinhole measurements is given in Table 6.10. The values are compatible within error margins.

Table 6.10: A comparison between beam size measured directly on the phosphor screen and beam size derived from the pinhole emittance measurement. The values are compatible within error margins.

	Direct P43 Measurement	From Pinhole Measurement
σ_x [mm]	1.46 ± 0.02	1.40 ± 0.09
σ_y [mm]	1.71 ± 0.01	1.61 ± 0.10

6.3.5 Emittance as a function of Bunch Charge

The emittance of bunches with different bunch charge and peak current was measured. An example is shown in Fig. 6.28. No strong increase of emittance is observed for large bunch charges as expected for a purely emittance dominated beam.

6.3.6 Emittance as a function of HV

Since the applied HV determines the space charge limitation of the cathode and the electrostatic focusing properties of the gun, it has a strong influence on the beam size evolution and the emittance. It is therefore of interest to investigate the emittance for different HV settings.

Unfortunately this is not possible for HV settings much below 40 keV because the screen monitors at the test stand are not sensitive enough to properly image a low intensity *and* low energy beam. It was observed that 40 keV was the lower energy limit to image beams with less than 2 mA peak current.

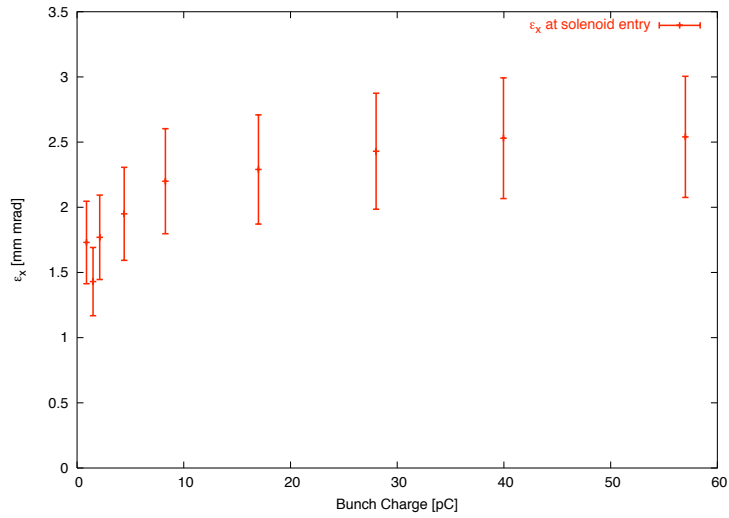


Figure 6.28: Emittance measured as a function of bunch charge. The emittance was measured with solenoid scans. 25 shots were integrated to improve the SNR on the phosphor screen monitor.

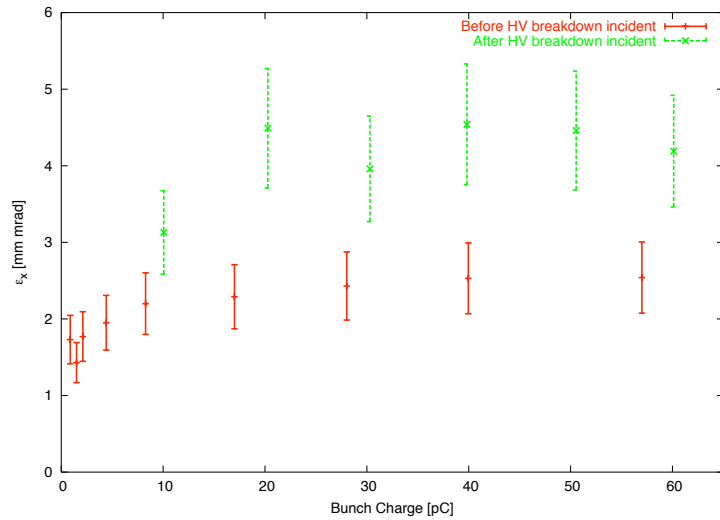


Figure 6.29: Emittance measured as a function of bunch charge before and after a HV breakdown incident. The HV arc partially destroyed the FEA leading to a highly non-homogenous emission and hence to an increased emittance. The emittance values measured after the incident have increased by as much as 100%.

It was therefore decided to perform emittance measurements at increased HV settings even though FEA operation at 50 keV and above had proven to be very delicate. During the first emittance measurements at 50 keV an arc triggered HV breakdown and the measurement had to be aborted. The FEA suffered damage: emission intensity was reduced by roughly a factor two. A second attempt to measure the emittance at 50 keV was made. In this run a severe HV arc hit the FEA and left a large crater (visible by eye!) which bridged the gate isolation and rendered the FEA useless. No successful emittance measurements have been performed at increased HV settings.

The damage suffered from the first HV arc is however a nice example to demonstrate how FEA surface damage influences the emittance of the FEA beam. Emittance measurements performed before and after the FEA damage show an increase of up to 100%. The emittance increase is caused by highly non-homogeneous emission from the partially destroyed FEA (see Section 2.6.3). A comparison of emittances measured for different bunch charges before and after the HV breakdown incident is shown in Fig. 6.29.

6.3.7 Emission Considerations

In addition to the characterization of the beam dynamics of a bunch emitted by an FEA source, the measurements performed at the gun test stand help to characterize the emission process. The normalized emittance measured for the SRI FEAs at 40 keV is on the order of 1 mm mrad. Since the bunches are emittance dominated this normalized emittance can be assumed constant. The FEA has an active emitting area with radius 0.5 mm which gives an RMS source size of $\sigma_x = 0.297$ mm (Gaussian fit for parabolic source distribution). This gives a simple estimate for the transverse momentum spread (in units of the rest mass) at the source

$$\sigma_{\gamma\beta_x} = \frac{\varepsilon^{(n)}}{\sigma_x} = 3.4 \cdot 10^{-3}. \quad (6.13)$$

The gate voltage gives the initial energy

$$e U_{\text{gate}} = \frac{m_e v^2}{2} \quad (6.14)$$

and therefore the total velocity at emission is given by

$$\beta = \sqrt{\frac{2 e U_{\text{gate}}}{m_e c^2}} = 2.6 \cdot 10^{-2} \quad (6.15)$$

for a gate voltage of 173 V. The emission angle is therefore

$$\sin \sigma_\theta = \frac{\sigma_{\beta_x}}{\beta} = 0.129 \quad \longrightarrow \quad \sigma_\theta \approx 7.4^\circ, \quad (6.16)$$

which is in the same range as the results of other measurements of this source type [39]. It is however important to note that these are crude approximations: At emission the energy spread in the bunch is large, particle motion is not necessarily paraxial and emission is not homogeneous across the entire FEA surface.

6.4 Comparison of Measurements with Simulation

Between the transverse beam measurement results presented here and the simulated beam size and emittance presented in Chapter 3 some discrepancies are noticed. The beam size in the diagnostic section was found to be on the order of 0.5 – 3 mm depending on the solenoid setting. The normalized transverse emittance was measured to be roughly 1 mm mrad. In the original simulations, beam sizes were found below 2 mm and normalized emittances were considerably lower at < 0.5 mm mrad.

However, there are several considerable differences between the parameters used for simulations and the actual experimental situation:

- Simulations were performed assuming a peak current of 100 mA in the bunch. In measurements it was discovered that the Spindt-type FEAs from SRI can only deliver peak currents on the order of a few mA. The reduced bunch current leads to reduced space charge forces and hence the gun design becomes over-focusing. Also, the character of the emitted bunches changes entirely: At 100 mA the emitted beam would have been space charge dominated; at a few mA the beam is neither clearly space charge nor emittance dominated according to Eq. (2.37).
- In the original simulations a gate voltage of roughly 50 V was assumed sufficient to trigger emission of the required peak current. Correspondingly the initial energy was chosen as $\gamma_0 = 1.0001$. In the measurements presented here, much higher gate voltages were applied. These higher gate voltages need to be taken into account in the γ_0 specified in simulations.
- The simulations carried out to design the test stand gun assumed that gated FEAs *with* a focusing layer would be used. It was therefore assumed that the source divergence would be nearly zero (see Section 3.1.1). The actually used Spindt-type FEAs from SRI lack a focusing layer and hence there is a finite source divergence which in turn can lead to a considerable source emittance contribution. Estimates shown in Section 6.3.7 indicate that this source divergence is not at all negligible.
- As mentioned in Section 5.3.1, the accelerating gap is larger than the design value of 11 mm. Before installation of the 3D mover motor system this cannot be corrected. The increased gap length leads to reduced accelerating gradient and hence to reduced electrostatic focusing of the emitted bunches.

There is currently no other FEA type available to generate a space charge dominated beam. An attempt to approximate the designed focusing properties with the current cathode type is to reduce the accelerating HV and thus

weaken the electrostatic focusing of the gun.⁷ Unfortunately a further HV reduction is not feasible due to the already low SNR of the screen monitors. At lower beam energies the signal of the beam on the screen becomes so weak that the beam size cannot be measured at all. Another approach is to redesign the electrodes for weaker bunches and replace the original electrodes with a new set. This is however not worthwhile since the LEG Project is interested in the characterization of a space charge dominated FEA beam and the investigation of emittance compensation. In the future, the test stand will be equipped with another type of FEA capable of delivering sufficient peak current and bunch charge. Efforts are underway to manufacture such FEA cathodes (see Section 7).

Therefore, in order to perform a direct comparison between simulation and experimental data the simulation parameters have therefore been adapted to reflect the actual measurement conditions as a closely as possible. The MAFIA simulation were run again with a new set of parameters:

- The peak current was reduced to match the peak current values of the SRI cathodes.
- The initial energy γ_0 was increased to take into account the higher gate voltages according to $\gamma_0 = 1 + \frac{eU_{\text{gate}}}{m_e c^2}$.
- The diode gap was increased to 12 mm to take into account the longitudinal misalignment (see Section 5.3.1).
- An initial source divergence was introduced by the parameter θ_0^{max} . Particle divergences are distributed randomly between 0° and $\pm\theta_0^{\text{max}}$.

An example of a comparison between measurement data and simulation is given in Fig. 6.30 where the beam size data presented in Fig. 6.17 is plotted together with simulation data. The 40 keV 0.642 mA bunch is focused with

⁷This has already happened since the applied HV is 40 kV rather than the design value of 100 kV.

a solenoid magnetic field of 53.6 mT. For the gate voltage of 173 V a γ_0 of 1.00034 has been used.

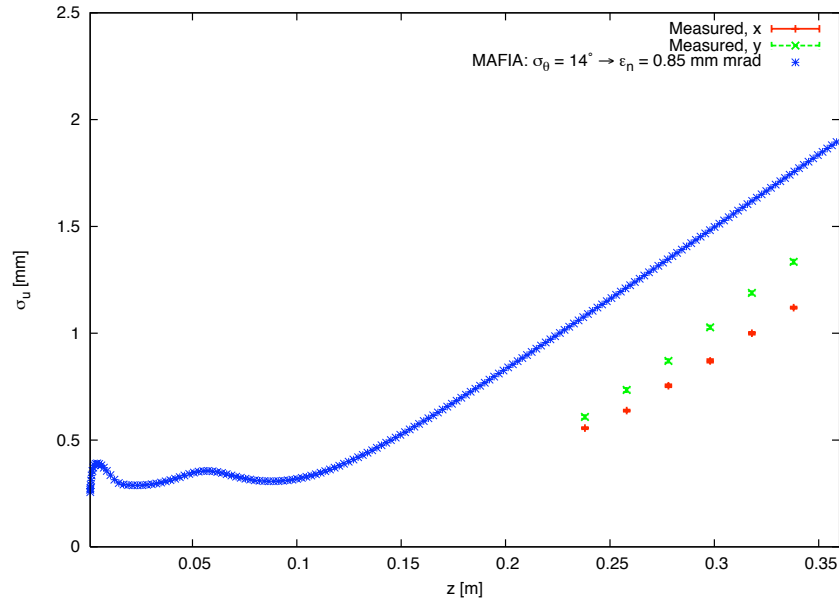


Figure 6.30: A comparison between measured data (see Fig. 6.17) and simulation. A bunch with 0.642 mA peak current and normalized transverse emittance of roughly 1 mm mrad is focused with 53.6 mT. The simulation used a source divergence of $\sigma_\theta = 14^\circ$.

The initial source divergence parameter was determined by observing the resulting emittance. For a source divergence of $\sigma_\theta = 14^\circ$ a normalized transverse emittance of 0.85 mm mrad is given by MAFIA. This is slightly less than what was measured, however a further increase of the source divergence was not feasible because particle loss at the anode iris began which in turn influences the emittance results. Although the emittance and slope of the beam size are roughly correct, the actual beam size is systematically too large in simulations. If the applied solenoid strength is varied, the slope can be changed, but the proper beam size is not reached.

Another attempt to match measurement data is to reduce the source divergence angle. This is shown in Fig. 6.31 where a source divergence of $\sigma_\theta = 6^\circ$

has been used in MAFIA. Although the beam sizes given by MAFIA are now roughly on the same order as in the measurement, the beam size slope and emittance (MAFIA gives a normalized transverse value of 0.41 mm mrad) are off.

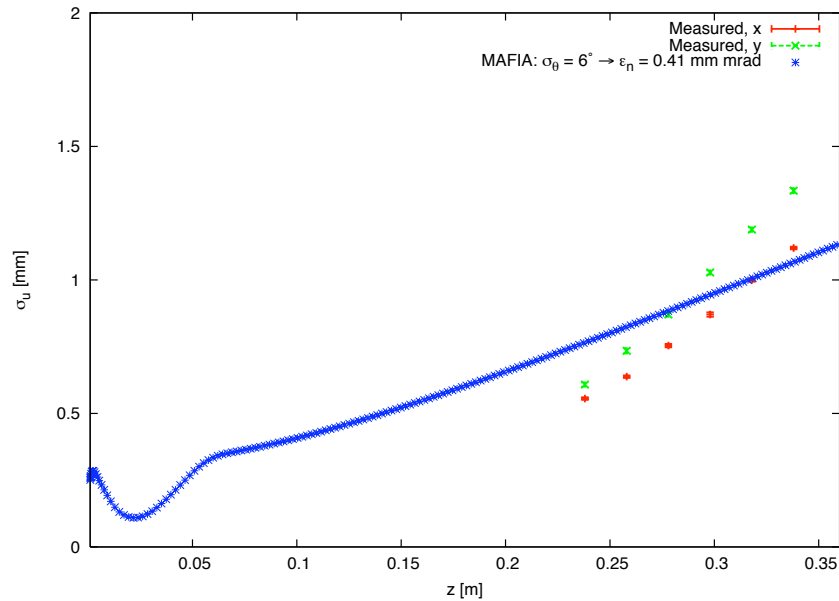


Figure 6.31: A comparison between measured data (see Fig. 6.17) and simulation. A bunch with 0.642 mA peak current and normalized transverse emittance of roughly 1 mm mrad is focused with 53.6 mT. The simulation used a source divergence of $\sigma_\theta = 6^\circ$.

The discrepancies observed here illustrate that at the test stand there is obviously an emittance contribution in addition to the source divergence. The emittance given by MAFIA is clearly too low although the applied source divergence has already been maximized. An additional emittance contribution which can not modeled by MAFIA has to be assumed present.

There are basically two possible explanations: The assumed transverse misalignment of the cathode (see Section 5.3.5) will lead to increased nonlinearities of the electrostatic focusing field at the anode iris which in turn can increase the emittance. Until the 3D mover motor system is installed and the

misalignment has been corrected, it will however not be possible to verify if such a misalignment can lead to an emittance growth on the order of 100%.

A second explanation is given by the fact that the actual emission process has not been modeled by the MAFIA simulation. Emission was assumed to be homogeneous over the entire emission surface of the FEA. It has been shown [23] that non-homogeneous emission with large correlation lengths can lead to a considerable amount of emittance deterioration at the source. If the measured emittance is considerably high (also after correction of the misalignment!) compared to the simulated emittance, non-homogeneous emission has to be assumed the likely cause. In such a scenario, a code capable of simulating the actual emission process would have to be used in combination with MAFIA to properly match measured data.

Chapter 7

Conclusions & Outlook

Summary

The 100 keV DC Gun Test Stand has been designed, assembled, commissioned and is now in full operation. It allows measurement of the complete transverse phase space of a particle bunch emitted by an FEA cathode. Measurements have been performed with alternative methods in order to compare results and validate measurement techniques. Different measurement techniques render compatible results. Online emittance optimization is possible with the established tools.

Measurements have been compared to simulations and show that the actual emission process has to be modeled in detail to reach full agreement between simulation and measurement. The simulation framework presented here could be used in combination with a code which models the emission process (for example CAPONE, presented in [23]) for the design of a scaled-up version of the actual LEG. The required beam diagnostics as well as the specifications for the assembly of the LEG can make use of the tools developed for the 100 keV DC Gun Test Stand.

FEA operation in the test stand is stable within boundaries that are now known and described. The test stand is available to measure transverse bunch properties of bunches emitted by cathode candidates for the LEG Project. Due to its modular design the gun can be adapted to house various types of cathodes.

Conclusions

Measurements of the performance of SRI FEAs revealed clearly that emission current was far too low for use as a cathode in a low emittance gun. Peak currents collected from the FEAs remained well below 10 mA while the proposed X-FEL gun requires 5.5 A peak current. Measurements at the test stand revealed emittances above 2 mm mrad which is a factor 40 higher than the proposed design requires at the gun exit. Finally, the sensitivity of the FEAs to HV breakdown needs to be addressed to ensure decent cathode lifetime.

An FEA candidate with a gate *and* focusing layer will reduce the source divergence and hence the emittance at the gun exit. PSI's LMN is currently developing the process to manufacture gated and focused FEAs optimized for use in a low emittance gun. As soon as working FEA samples are delivered, they will be installed in the test stand: Transverse properties of the emitted bunches as well as FEA performance will be characterized, giving feedback for the optimization and production process.

A lower emittance and higher peak current will render space charge dominated beams. The emittance will no longer remain constant throughout the test stand and the evolution of the emittance will be measured with the pepper-pot setup. This will allow investigation of the emittance compensation scheme with the tools made available in the scope of this thesis. In addition, the current SNR issues of the screen monitor systems should be mitigated by increased beam intensity. With a better SNR, transverse measurements should have lower errors due to the decreased background level

uncertainty. And finally, with an increased SNR, true single-shot measurements (no image averaging) — a big advantage of the pinhole array and pepper-pot techniques — should become possible.

Outlook

There is a long list of further planned activity at the test stand as well as ideas for future measurements.

In a first step the dimensions of the slit array masks have to be adapted for the large emittances of the current emitters in order to use them as an alternative emittance measurement method.

The steering of the beam due to earth magnetic field and residual dipole moment of the solenoid can be corrected with two sets of Helmholtz coils added above and below the beam path. The necessary power supply hardware and controls have been prepared. Once the coils are installed, proper tuning will allow cancellation of any beam steering observed with the screen monitors.

The 3D mover motor system is currently being commissioned and will soon be installed. It will allow for the first time to correct for misalignment of the cathode with respect to the anode, solenoid magnet and drift section. It is expected that once the diode is properly aligned, stepping up the DC HV to the design setting of 100 keV will become possible. Also, it is expected that an FEA properly aligned to the anode iris will trigger less parasitic emission and HV breakdown. Increased HV will lead to higher bunch energy, increased electrostatic focusing and therefore considerably change the dynamics of the bunches emitted by the FEA. In addition, the 3D mover motor system will allow correction of the gap length to the design value as well as a reduction of the accelerating gap to increase the accelerating gradient.

The pepper-pot system has not been used yet, but will be installed in the near future. The pepper-pot makes use of the same measurement principles as the pinhole array, but contrary to the fixed location of the pinhole array, the pepper-pot can be driven through the beam longitudinally which will allow

measurement of the emittance evolution along the beam path. Especially for space charge dominated beams and investigation of emittance compensation, this will be an indispensable diagnostic device. The measurement readout and analysis software is ready and has been used successfully for pinhole array measurements. Once the pepper-pot is installed, measurements of the transverse phase space distribution at arbitrary locations in the diagnostic section will become possible.

Since the SRI FEAs have proven to be insufficient for use as a low emittance gun source, there is also interest to measure other cathode candidates at the test stand. Recent experiments [37] have shown that laser-induced emission from single needle tips generates the peak current required for the proposed X-FEL gun. The emission process is however not yet understood and hence there is little knowledge of the phase space distribution of the emitted bunches. The gun test stand is suitable for such measurements. The challenge is to redesign parts of the test stand so that the pulsed 100 kV transformer can be connected to the needle tip and the laser can be coupled into the gun and properly focused on the tip. Due to the modular design of the test stand this task should be manageable.

Finally, the test stand cathode mounts and feedthroughs will be adapted to house FEA samples from LMN which will hopefully arrive soon. The LMN FEA samples will be gated, focused and deliver higher emission current than the present SRI FEAs. The test stand can be used to benchmark performance of the LMN samples as well as verify that the cathodes have been successfully optimized for use in a low emittance gun. If an FEA candidate is found that fulfills the design specifications of the X-FEL gun, first longitudinal phase space investigations will then be performed at the 500 kV pulser and RF cavity test stand.

Acknowledgments

It goes without saying that the design and commissioning of the test stand presented in this thesis would have never been possible without the help of countless people at PSI. Some gave advice or shared their experience while others offered a helping hand or technical support. And yet others encouraged me to continue my research and cheered me up even when at some times my work seemed unpromising. To all these people I owe my sincere gratitude.

I would first like to thank Prof. Dr. Albin Wrulich for giving me the opportunity to do these studies and work in his research group for the LEG Project. I greatly appreciated his friendly and encouraging nature. Many thanks go to my supervisor Dr. Andreas Streun for his advice and guidance. I learned very much in our long discussions thanks to his profound knowledge of beam dynamics. I am very grateful to Dr. Åke Andersson who spent many hours together with me at the test stand; not only his questions and advice helped me advance the experiment, but also his hands-on support during countless hours of disassembly and reassembly of the vacuum chamber.

I would like to express my thanks also to Dr. Volker Schlott, Albert Kammerer, and Andreas Jaggi for their help with the diagnostics involved at the test stand. Without their experience and knowledge of the technical details of the diagnostics, decent experimental data acquisition would not have been possible.

I also thank Dr. Micha Dehler for his help with MAFIA especially while I was

getting started with the design simulations. But also later on he answered many of my MAFIA related questions which I greatly appreciate.

Dr. Marco Pedrozzi set me up with the Parmela code and helped me with my very first simulation runs. He also offered a lot of advice for HV commissioning and signal transmission. I appreciate his effort and his encouragement.

I am grateful to Dr. Romain Ganter for his support with cathode and FEA issues. Not only did he give me a whole lot of information about FEAs, he was also the person who showed me how to properly assemble vacuum chambers and deal with UHV components. I would also like to say thank you to Dr. Frédéric Le Pimpec for his insight on surfaces in high electric fields and all the discussions on HV conditioning and breakdown.

I owe many thanks to Dr. Lothar Schulz, Martin Steinacher, Theo Bieri, Reno Gaiffi, and Peter Huber of the SLS vacuum group for all their support. Without their effort I would have not been able to reach the stable UHV conditions required for experiments like the ones reported here. Their friendly advice has been greatly appreciated.

I would like to acknowledge Dr. Detlef Vermeulen, Dr. Mirek Dach, Martin Heiniger, and Babak Kalantari for all their support with the control system and the controls applications used at the test stand. There was a great deal of work involved in connecting all experimental hardware to a fully digital control system and they made this possible.

I am grateful to Dr. Rafael Abela for unbureaucratically offering space in the SLS experimental hall at X03D to install the bunker for the test stand.

As always in an experimental effort, there are many contributors without whom the final results would have not been achievable. I would like to thank all who offered their support: Dr. Andreas Adelman, Ernst Baumann, Robin Betemps, Dr. Michael Böge, Sigi Bohr, Marlen Bugmann, Andreas Duffner, Dave George, Benjamin Gross, Peter Häberli, Max Heimgartner, Colin Higgs, Matt Horvat, Bruno Jakob, Dr. Eugenie Kirk, Christof Kraus, Dr. Juraj Krempasky, Markus Kropf, Dr. Andreas Lüdeke, Matthias

Moser, Dr. Marco Negrazus, Hansjörg Oehler, Dr. Benedikt Oswald, Martin Paraliiev, Dr. Thomas Schietinger, Christian Vollenweider, Elmar Zehnder, Charlie Zumbach.

Finally, I would like to express my profound gratitude to my parents and my girlfriend Dina. My parents encouraged my interest in science for as long as I can remember. Thanks Dad, your tours of the accelerators and all the machines at LBL (especially E. O. Lawrence's original 1931 4.5 inch cyclotron) must have sparked something in my young soul. My parents gave me the opportunity to study physics, ultimately making it possible for me to perform this work. My girlfriend Dina has supported me throughout my undergraduate and graduate studies and has been a great source of encouragement for my PhD work. I am sincerely thankful to her for helping me get through the tough times but also for celebrating with me the great times. And there were many.

Appendix A

Design Drawings of the Gun Test Stand

This section shows original design drawings of the main test stand components: an overview of the entire test stand, a sectional drawing through the cathode cone and ceramic break, detail drawings of the cathode/FEA and anode/solenoid assemblies, and an overview drawing of the diagnostics section.

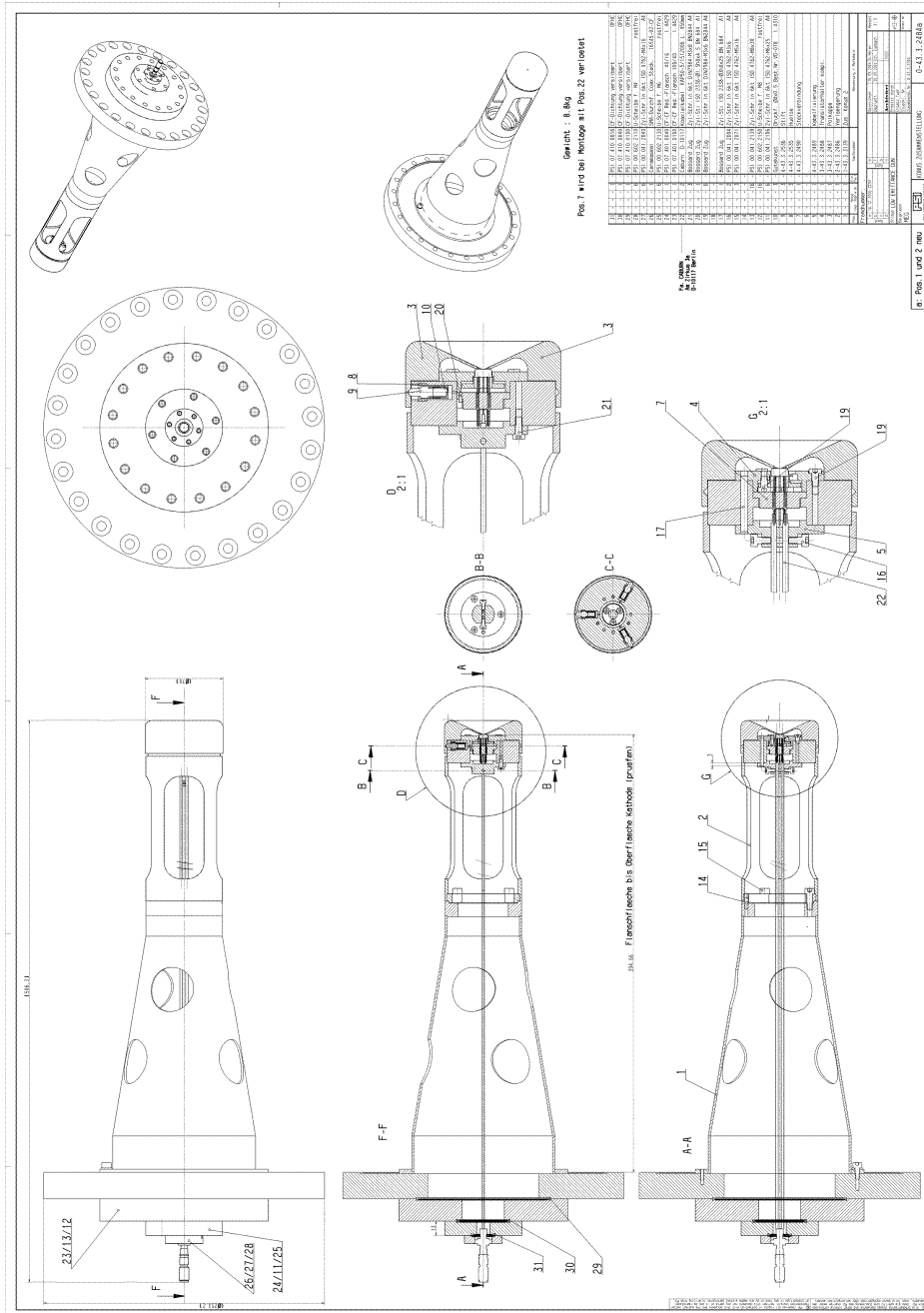


Figure A.3: Design drawing of the cathode assembly with FEA mounting.

Bibliography

- [1] *SLS: Swiss Light Source*, <http://sls.web.psi.ch/>
- [2] *LEG: The Low Emittance Gun Project at PSI*, <http://leg.web.psi.ch>
- [3] K. Wille: *Physik der Teilchenbeschleuniger und Synchrotronstrahlungsquellen*, 2nd Ed., Teubner Studienbücher, Stuttgart, 1996
- [4] *TTF: TESLA Test Facility*, <http://tesla.desy.de/>
- [5] J. Rossbach: *New Developments on Free Electron Lasers Based on Self-Amplified Spontaneous Emission*, Proceedings of PAC 2001, Chicago IL, USA, p. 11
- [6] H. Wiedemann: *Particle Accelerator Physics I, Basic Principles and Linear Beam Dynamics*, 2nd Ed., Springer, Berlin, 1999
- [7] A. W. Chao, M. Tigner: *Handbook of Accelerator Physics and Engineering*, World Scientific, Singapore, 1999
- [8] H. Wiedemann: *Particle Accelerator Physics II, Nonlinear and Higher-Order Beam Dynamics*, 2nd Ed., Springer, Berlin, 1999
- [9] *LCLS: Linac Coherent Light Source*, <http://www-ssrl.slac.stanford.edu/lcls>
- [10] *European X-Ray Laser Project XFEL*, <http://xfel.desy.de/xfelhomepage>

- [11] *SCSS: SPring-8 Compact SASE Source*, <http://www-xfel.spring8.or.jp/>
- [12] K. Togawa et al.: *Pulsed HV Electron Gun with Thermionic Cathode for the Soft X-Ray FEL Project at SPring-8*, Proceedings of PAC 2003, Portland OR, USA, p. 3332
- [13] T. Shintake: *Status of the SCSS Project*, Proceedings of APAC 2004, Gyeongju, Korea, p. 4
- [14] *An X-Ray Free Electron Laser at Paul Scherrer Institute*, PSI-FEL/LEG Project Team Internal Report, December 2005, <http://leg.web.psi.ch/public/publications/2005/>
- [15] *LEG/X-FEL Parameter List*, <http://leg.web.psi.ch/>
- [16] C. M. Tang, A. C. Ting, T. Swyden: *Field-emission arrays — a potentially bright source*, Nucl. Instr. and Meth. A318, p. 353, 1992
- [17] A. Hofmann: *Kinetic Theory*, CERN Yellow Report 95-06 Vol. 1, p. 259
- [18] E. R. Colby: *Design, Construction, and Testing of a Radiofrequency Electron Photoinjector for the Next Generation Linear Collider*, FERMILAB-THESIS-1997-03, <http://lss.fnal.gov/archive/thesis/fermilab-thesis-1997-03.pdf>
- [19] F. B. Kiewiet: *Generation of ultra-short, high-brightness relativistic electron bunches*, PhD Thesis, Technical University Eindhoven, 2003, <http://alexandria.tue.nl/extra2/200313092.pdf>
- [20] M. Ferrario: *Space Charge Effects*, CERN Accelerator School, Trieste, Italy, 2005, <http://cas.web.cern.ch/cas/Trieste-2005/Trieste-lectures.htm>
- [21] A. E. Candel, M. M. Dehler, S. C. Leemann: *Electron Beam Dynamics Simulations for the Low Emittance Gun*, Proceedings of EPAC 2004, Lucerne, Switzerland, p. 2505

- [22] W. Joho: *Fun with Formulas*, CERN Accelerator School, Brunnen, Switzerland, 2003, <http://cas.web.cern.ch/cas/BRUNNEN/lectures.html>
- [23] A. E. Candel: *Simulation of Electron Source for Next-Generation X-Ray Free Electron Laser*, PhD Thesis, Diss. ETH Nr. 16181, ETH Zurich, 2005, <http://www.itp.phys.ethz.ch/staff/candel/publications/PhDThesis.pdf>
- [24] P. Emma: *Issues and Challenges for Short Pulse Radiation Production*, Proceedings of EPAC 2004, Lucerne, Switzerland, p. 225
- [25] *TESLA Technical Design Report*, Part II - The Accelerator, 2001
- [26] B. E. Carlsten, T. O. Raubenheimer: *Emittance growth of bunched beams in bends*, Phys. Rev. E, Vol. 51, p. 1453, 1995
- [27] B. E. Carlsten: *New Photoelectric Injector Design for the Los Alamos National Laboratory XUV FEL Accelerator*, Nucl. Instr. and Meth. A285, p. 313, 1989
- [28] X. Qiu et al.: *Demonstration of Emittance Compensation through the Measurement of the Slice Emittance of a 10-ps Electron Bunch*, Phys. Rev. Lett, Vol. 76, No. 20, p. 3723, 1996
- [29] V. V. Miltchev et al.: *Transverse Emittance Measurements at the Photo Injector Test Facility at DESY Zeuthen*, Proceedings of FEL 2004, Trieste, Italy, p. 399
- [30] S. B. van der Geer et al.: *Nonlinear electrostatic emittance compensation in kA, fs electron bunches*, Phys. Rev. E, Vol. 65, 046501, 2002
- [31] T. Shintake: *Small Emittance Sources/Guns*, CERN Accelerator School, Brunnen, Switzerland, 2003, <http://cas.web.cern.ch/cas/BRUNNEN/lectures.html>

- [32] S. Humphries: *Charged Particle Beams*, John Wiley & Sons, Inc., New York, 1990
- [33] C. Travier: *An Introduction to Photo-Injector Design*, LAL/RT 93-08, 1993, http://www-lib.kek.jp/cgi-bin/img_index?9310273
- [34] *PITZ: Photo Injector Test Facility at DESY Zeuthen*, <http://adweb.desy.de/pitz/web/index.html>
- [35] F. Stephan: *Status and Perspectives of Photo Injector Developments for High Brightness Beams*, Talk given at the ICFA Workshop on “The Physics and Applications of High Brightness Electron Beams”, Erice, Italy, 2005
- [36] R. Ganter et al.: *Nanosecond field emitted current pulses from ZrC needles and field emitter arrays*, J. Vac. Sci. Technol. B, Vol. 24, No. 2, p. 974, 2006
- [37] R. Ganter: *High Current Electron Emission from Microscopic Tips*, Proceedings of FEL 2006, Berlin, Germany, to be published
- [38] *Laboratory for Micro- and Nanotechnology (LMN) at PSI*, <http://lmn.web.psi.ch/>
- [39] W. Zhu: *Vacuum Microelectronics*, John Wiley & Sons, Inc., New York, 2001
- [40] M. Dehler, A. Candel, E. Gjonaj: *Full scale simulation of a field-emitter array based electron source for free-electron lasers*, J. Vac. Sci. Technol. B, Vol. 24, No. 2, p. 892, 2006
- [41] L. Dvorson, A. I. Akinwande: *Double-gated Spindt emitters with stacked focusing electrode*, J. Vac. Sci. Technol. B, Vol. 20, No. 1, p. 53, 2002
- [42] *SRI International: MicroSystems Innovation Center*, Menlo Park CA, USA, <http://www.sri.com/psd/microsys/>

- [43] S. C. Leemann: *100 keV Gun Test Stand: Design and Parameter Study*, SLS Internal Note, SLS-TME-TA-2004-0244, 2004, <http://slsbd.psi.ch/pub/>
- [44] *MAFIA: Solution of Maxwell's Equations Using a Finite Integration Algorithm*, CST GmbH, Darmstadt, Germany, <http://www.cst.de/>
- [45] J. R. Pierce: *Rectilinear Electron Flow in Beams*, J. Appl. Phys., Vol. 11, No. 8, p. 548, 1940
- [46] M. von Ardenne: *Tabellen der Elektronenphysik, Ionenphysik und Übermikroskopie*, Band II, Deutscher Verlag der Wissenschaften, Berlin, 1956
- [47] A. Streun: *Entwurf eines Solenoids für den 100 keV Gun Teststand*, Version 3, unpublished internal note
- [48] K. Flöttmann: *Pepper Pot Design for Space Charge Dominated High Brightness Beams*, DESY Internal Note, TESLA-FEL 96-09, 1996
- [49] *GPT: General Particle Tracer*, Pulsar Physics, Soest, The Netherlands, <http://www.pulsar.nl/>
- [50] *Bewilligung für den Umgang mit ionisierender Strahlung vom 6. Juni 2006*, Bewilligungsnummer AG-0444.09.024, Bundesamt für Gesundheit
- [51] *TermoTek Laserkühlung AG*, Rastatt, Germany, <http://www.termotek-ag.com/>
- [52] L. Tanner, F. Jenni: *Digital Control for Highest Precision Accelerator Power Supplies*, Proceedings of PAC 2001, Chicago, USA, p. 3681
- [53] *F.u.G. Elektronik GmbH*, Rosenheim, Germany, <http://www.fug-elektronik.de/>
- [54] *PPT Puls-Plasmatechnik GmbH*, Dortmund, Germany, <http://www.puls-plasmatechnik.de/>

- [55] *Avtech Electrosystems Ltd.*, Ogdensburg NY, USA, <http://www.avtechpulse.com/>
- [56] *Varian, Inc.*, Palo Alto CA, USA, <http://www.varianinc.com/>
- [57] *Pfeiffer Vacuum GmbH*, Asslar, Germany, <http://www.pfeiffer-vacuum.de/>
- [58] *EPICS: Experimental Physics and Industrial Control System*, <http://www.aps.anl.gov/epics>
- [59] *W&T: Wiesemann und Theis GmbH*, Wuppertal, Germany, <http://www.wut.de/>
- [60] *VI Control Systems Ltd.*, Los Alamos NM, USA, <http://www.vicontrols.com/>
- [61] *LeCroy Corporation*, Chestnut Ridge NY, USA, <http://www.lecroy.com/>
- [62] *Sony Business Solutions & Systems*, Park Ridge NJ, USA, <http://bssc.sel.sony.com/>
- [63] *Thales Optem, EHD imaging GmbH*, Damme, Germany, <http://thales-optem.de/>
- [64] A. Streun: *CAM*, an IDL application to read out, display and post-process frame grabber data, <http://slsbd.psi.ch/~streun/apps/cam/>
- [65] K. Flöttmann: *Some basic features of the beam emittance*, Phys. Rev. ST Accel. Beams, Vol. 6, 034202, 2003
- [66] S. G. Anderson et al.: *Space-charge effects in high brightness electron beam emittance measurements*, Phys. Rev. ST Accel. Beams, Vol. 5, 014201, 2002

- [67] *GNU Octave*, a free Matlab-like high-level language, <http://www.octave.org/>
- [68] S. C. Leemann, Å. Andersson: *Gun Test Stand Solenoid Measurements*, SLS Internal Note, SLS-TME-TA-2005-0264, 2005, <http://slsbd.psi.ch/pub/>
- [69] *F. W. Bell / Sypris Test & Measurement*, Orlando FL, USA, <http://www.fwbell.com/>
- [70] Å. Andersson, S. C. Leemann: *Experimental Determination of the Point-Spread Function for the Optical Diagnostics Setup at the 100 keV Gun Test Stand*, SLS Internal Note, SLS-TME-TA-2005-0278, 2005, <http://slsbd.psi.ch/pub/>
- [71] K. L. Jensen et al.: *Space charge effects on the current-voltage characteristics of gated field emitter arrays*, J. Appl. Phys., Vol. 82, No. 2, p. 845, 1997
- [72] J. D. Lawson: *The Physics of Charged-Particle Beams*, 2nd Ed., Oxford University Press, Oxford, 1988
- [73] J. Schmerge: *LCLS Gun Solenoid Design Considerations*, LCLS Technical Note, LCLS-TN-05-14, 2005, <http://www-ssrl.slac.stanford.edu/lcls/technotes/lcls-tn-05-14.pdf>
- [74] W. H. Press, B. P. Flannery, S. A. Teukolsky, W. T. Vetterling: *Numerical Recipes in Pascal — The Art of Scientific Computing*, Cambridge University Press, Cambridge, 1989
- [75] A. Streun: *EMM*, an IDL application to calculate emittance by applying Levenberg-Marquardt fits to quadrupole scan data, <http://slsbd.psi.ch/~streun/apps/emm/>

Curriculum Vitae

September 7, 1976	Born in Oakland CA, USA
1982 – 1987	Elementary school in Walnut Creek CA, USA
1988	Elementary school in Geneva, Switzerland
1989	Junior high school in Walnut Creek CA, USA
1990 – 1992	Junior high school in Berikon-Widen AG, Switzerland
1992 – 1996	High school in Lucerne, Switzerland
1996 – 2001	Undergraduate studies in physics at ETH Zurich, Switzerland
1999 – 2001	Teaching assistant for mathematics at ETH Zurich, Switzerland
2001 – 2002	Master’s Thesis at PSI, Villigen, Switzerland: “Precise Beam Energy Calibration at the SLS Storage Ring by Means of Resonant Spin Depolarization”
2002	Guest of the Accelerator Theory Group, Japanese National High Energy Accelerator Research Organization KEK Tsukuba, Japan: “Second Order Fringe in MAD-X for the Module PTC”
2002 – 2007	Graduate research assistant at PSI, Villigen, Switzerland
2004 – 2007	Graduate studies at the Laboratory for Particle Accelerators, EPF Lausanne, Switzerland
2004 – 2006	Teaching assistant for particle accelerator physics at EPF Lausanne, Switzerland

A list of publications can be found at <http://www.simonleemann.ch/work.html>